Bond-length fluctuations in the copper oxide superconductors

2003 J. Phys.: Condens. Matter 15 R257

(http://iopscience.iop.org/0953-8984/15/7/201)

INSTITUTE OF PHYSICS PUBLISHING JOURNAL OF PHYSICS: CONDENSED MATTER

J. Phys.: Condens. Matter **15** (2003) R257–R326 PII: S0953-8984(03)31434-1

TOPICAL REVIEW

Bond-length fluctuations in the copper oxide superconductors

John B Goodenough

Texas Materials Institute, ETC 9.102, University of Texas at Austin, Austin, TX 78712, USA

Received 1 November 2002
Published 10 February 2003
Online at stacks.iop.org/JPhysCM/15/R257

Abstract

Superconductivity in the copper oxides occurs at a crossover from localized to itinerant electronic behaviour, a transition that is first order. A spinodal phase segregation is normally accomplished by atomic diffusion; but where it occurs at too low a temperature for atomic diffusion, it may be realized by cooperative atomic displacements. Locally cooperative, fluctuating atomic displacements may stabilize a distinguishable phase lying between a localized-electron phase and a Fermi-liquid phase; this intermediate phase exhibits quantum-critical-point behaviour with strong electron–lattice interactions making charge transport vibronic. Ordering of the bond-length fluctuations at lower temperatures would normally stabilize a charge-density wave (CDW), which suppresses superconductivity. It is argued that in the copper oxide superconductors, crossover occurs at an optimal doping concentration for the formation of ordered two-electron/two-hole bosonic bags of spin $S = 0$ in a matrix of localized spins; the correlation bags contain two holes in a linear cluster of four copper centres ordered within alternate Cu–O–Cu rows of a CuO_2 sheet. This ordering is optimal at a hole concentration per Cu atom of $p \approx 1/6$, but it is not static. Hybridization of the vibronic electrons with the phonons that define long-range order of the fluctuating (Cu–O) bond lengths creates barely itinerant, vibronic quasiparticles of heavy mass. The heavy itinerant vibrons form Cooper pairs having a coherence length of the dimension of the bosonic bags. It is the hybridization of electrons and phonons that, it is suggested, stabilizes the superconductive state relative to a CDW state.

Contents

1. Introduction

The discovery in 1986 of high-temperature superconductivity in the copper oxides [1] stimulated a renaissance of interest in transition-metal oxides with perovskite-related structures. Of particular interest were transition-metal oxide systems that undergo a change of their d electrons from localized to itinerant behaviour as a function of the d-electron bandwidth and/or the valence state of the transition-metal atom since the high superconductive critical temperature T_c in the copper oxides is found at such a crossover.

The parent compound of all the copper oxide superconductors is an antiferromagnetic insulator with a single d electron per Cu atom in an $x^2 - y^2$ antibonding σ^* band of a CuO_2 sheet with $(180° - \phi)$ Cu–O–Cu bond angles. Therefore, initial experiments were concentrated not only on the copper oxide superconductors, but also on systems having a single d electron per transition-metal atom in a parent antiferromagnetic compound. However, failure to find the high-T_c superconductive phenomenon in other perovskite-related systems with both a single d electron per transition-metal atom in the parent compound and a crossover from localized to itinerant electronic behaviour has introduced the question 'What is unique about the copper oxide superconductors?'.

On the other hand, the subsequent discovery of a colossal negative magnetoresistance (CMR) just above a Curie temperature T_C in the manganese oxide perovskites at the crossover from localized to itinerant electronic behaviour has broadened interest in the more general question of how this crossover proceeds in perovskite-related structures. There is now mounting experimental evidence that the crossover occurs in a first-order transition and that where the resulting phase separation would occur at too low a temperature for atomic diffusion, it is accommodated by cooperative oxygen-atom displacements that create a spinodal phase segregation at a small length scale. These cooperative displacements fluctuate, which leads to bond-length fluctuations and therefore to fluctuations of the two phases. Two-phase fluctuations are not detected by a conventional diffraction experiment; fast experimental probes are required to reveal them directly. However, once phase fluctuations have been detected directly, other experimental probes can be developed that allow their existence to be inferred from indirect physical phenomena.

Stabilization of a phase intermediate between localized and itinerant electron behaviour may also occur; it is characterized by locally cooperative bond-length fluctuations at higher temperatures. These fluctuations have been identified as a quantum-critical-point (QCP) phenomenon. At lower temperatures, long-range-cooperative bond-length ordering may result

in stabilization of a charge-density wave (CDW) or a superconductive phase. In most materials, a CDW is stabilized; the CDW opens a gap at the Fermi surface, which suppresses Cooper-pair formation. Therefore, the challenging question is the character of the superconductive phase that can compete with a CDW. In this review, it is argued that the superconductive phase in the copper oxides is associated with two phenomena:

(i) an ordering of bosonic two-electron/two-hole correlation bags into alternate Cu–O–Cu rows of a CuO_2 sheet and
(ii) hybridization of electrons with phonons associated with long-range-cooperative Cu–O bond-length fluctuations that define the moving, ordered bags.

The electron–phonon hybridization results in itinerant vibronic quasiparticles of heavy mass, and Cooper pairs of these quasiparticles are bound by a non-retarded elastic energy rather than by the retarded electron–phonon coupling of a conventional superconductor.

The copper oxides are type-II superconductors; quenching of the superconductivity by an external magnetic field does not occur globally at a critical field strength H_c as in a type-I superconductor, but progresses in steps by the introduction of bundles of magnetic flux in normal-state vortices. The phenomenology of vortex behaviour in the optimally doped copper oxide superconductors is well described with a single-phase model; in the superconductive state below T_c any two-phase fluctuations must be ordered into a traveling CDW in which a phonon interacts strongly with the electrons, whereas above T_c the disordered fluctuations may be described as QCP behaviour or as a polaron liquid.

Early experiments demonstrated that the superconductive condensate consists of two-electron particles having paired spins like the Cooper pairs of a conventional superconductor, but the superconductive-pair coherence length ξ is anisotropic and small ($\xi_\perp \approx 3$ Å and $\xi_\parallel \approx 10$ Å) relative to its value in conventional superconductors, e.g. $\xi_{\rm conv} \approx 1000$ Å [2]. Since polaronic conduction is diffusive, which introduces an activation energy into a polaron mobility, most theorists have looked to the spin–spin superexchange interactions as the driving force for pair formation in the copper oxides. The parent compound contains Cu(II) having a localized spin $S = 1/2$. Oxidation creates a low-spin Cu(III) with spin $S = 0$ and reduction Cu(I) with $S = 0$. Since there is no spin–spin exchange stabilization for an ion with $S = 0$, the spin–spin interactions would segregate spin-rich 'spinon' clusters from spinless clusters, i.e. 'holon' clusters, on oxidation. This approach ignores bond-length fluctuations associated with the first-order character of a transition from localized to itinerant electronic behaviour. Too little appreciated is the fact that, at the crossover from localized to itinerant electronic behaviour, the time for an electron to tunnel from one Cu atom to another is roughly the period of an optical-mode oxygen vibration, $\tau_h \approx \omega_o^{-1}$, which reduces any activation energy in the diffusive mobility to $\Delta H_m < kT$. The associated strong electron–lattice coupling results in *vibronic* conductivity, which gives 'bad-metal' behaviour. The normal state of the copper oxide superconductors is metallic, but they are bad metals and the metallic conduction is not described by conventional itinerant-electron theory [3]. In this review, emphasis is placed on the role of electron–lattice coupling and of the bond-length fluctuations appearing at the crossover from localized-to itinerant-electronic behaviour, but a proper theory needs to introduce the contributions of both the spin–spin and the electron–lattice interactions and how they organize the two-phase fluctuations into a distinguishable thermodynamic state that supports high-T_c superconductivity.

First, the structural architecture of the copper oxide superconductors is compared to that of the perovskite structure. The architecture of the copper oxide superconductors removes the orbital degeneracy of the parent antiferromagnetic compound and creates 2D ($180° - \phi$) Cu–O–Cu bonding in (001) basal planes of corner-shared Cu sites; these sites may be

octahedral, square pyramidal or square coplanar. As a result, the electronic properties are strongly anisotropic.

Next, the electronic properties of the transition-metal oxides with perovskite structure are first formulated in the limit of localized 3d electrons; the transition from localized to itinerant electronic behaviour is introduced as a breakdown of the spin–spin superexchange perturbation theory. The virial theorem is employed to argue for a first-order transition from localized to itinerant electronic behaviour and to stress some predictions that follow from it.

The evolution of physical properties with the strength of the M–O–M bonding in a few single-valent AMO_3 perovskites (M = transition metal) are then reviewed to emphasize the generality of the concept of two-phase fluctuations at the crossover from localized to itinerant electrons in perovskite-related oxides.

Finally, the concept of a spinodal segregation into two-phase fluctuations at the crossover from antiferromagnetic insulator to itinerant-electron metal is applied to the copper oxide superconductors. An intermediate QCP phase is identified; ordering of the bond-length fluctuations in this phase selects a critical fraction of charge carriers per Cu atom, i.e. the composition of optimal doping, at which the phase becomes superconductive. The concept of a 'correlation bag' containing electrons in molecular orbitals of a cluster is contrasted with that of a 'holon' cluster. Evidence that the two-phase fluctuations order into 'travelling stripes' containing bosonic correlation bags is presented. Evidence for the formation of heavy quasiparticles propagating along the Cu–O–Cu bond axes is also discussed. The resulting scenario is shown to account for the compositional dependence of the phenomenon as well as why this high-T_c superconductivity mechanism has thus far been restricted to the layered copper oxides with $(180^\circ - \phi)$ Cu–O–Cu bonding.

2. Structural architecture of the copper oxide superconductors

2.1. The p-type superconductors

The ideal cubic-perovskite structure is illustrated in figure 1. An important feature of this AMO_3 structure is the matching of the equilibrium (A–O) and (M–O) bond lengths. Ideal matching occurs where the geometric tolerance factor

$$t \equiv (\text{A–O})/\sqrt{2}(\text{M–O}) \tag{1}$$

is unity. It is customary to express the equilibrium bond lengths in these oxides as the sum of tabulated ionic radii determined empirically from ambient x-ray data [4]. However, this procedure masks the fact that the (A–O) and (M–O) equilibrium bond lengths have quite different thermal-expansion coefficients and compressibilities. The (A–O) bond generally has the larger thermal-expansion coefficient, which makes $\mathrm{d}t/\mathrm{d}T > 0$. The (A–O) bond is normally more compressible, which makes $\mathrm{d}t/\mathrm{d}P < 0$ [5]; however, the equilibrium (M–O) bond has a double-well potential at the crossover from localized to itinerant electronic behaviour, which makes the (M–O) bond more compressible and $\mathrm{d}t/\mathrm{d}P > 0$ where there are bond-length fluctuations at crossover.

Accommodation of a $t < 1$ is made by a cooperative rotation of the corner-shared $MO_{6/2}$ octahedra so as to reduce the M–O–M bond angle from 180° to $(180^\circ - \phi)$. As t is reduced from $t = 1$, rotations about the [001] axis give tetragonal $I4/mcm$ symmetry; these rotations are followed at smaller t by rotations about [111] to give rhombohedral $R\bar{3}c$ symmetry and then about [110] to give orthorhombic $Pbnm$ (or $Pnma$) symmetry. The bending angle ϕ increases with decreasing t, changing discontinuously on going from one cooperative rotation to another.

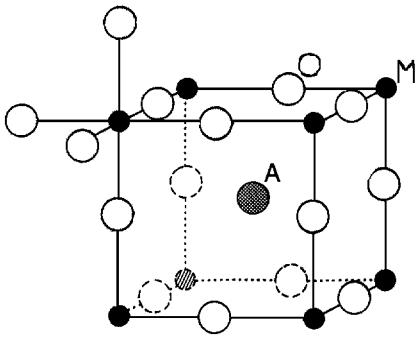

Figure 1. The structure of ideal cubic perovskite AMO_3.

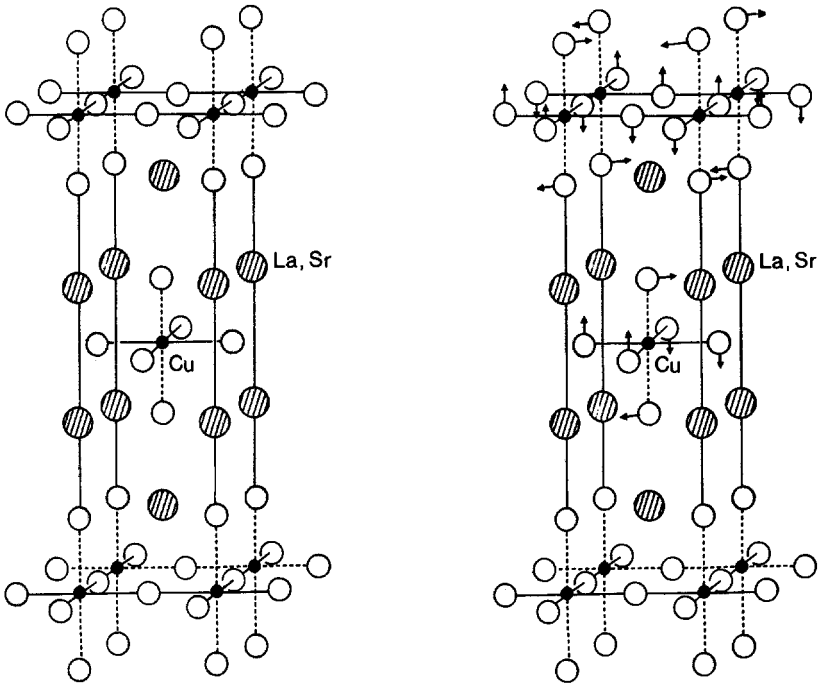

Figure 2. Structures of (a) tetragonal (T) and (b) orthorhombic (O) La_2CuO_4. The arrows represent the direction of tilting of the CuO_6 octahedra.

Examination of figure 1 shows that MO_2 layers alternate with AO rock-salt layers in the perovskite structure. Therefore, it is possible to insert a second rock-salt layer between two successive MO_2 layers, and these insertions tend to enter periodically to give the Ruddlesden–Popper [6] family of phases $AO{\cdot}(AMO_3)_n$. The tetragonal structure of figure 2(a) is the simplest of these intergrowth structures. The high-temperature structure of the parent compound La_2CuO_4, for example, has this structure. However, a room-temperature two-dimensional tolerance factor $t_{2D} < 1$ introduces a cooperative rotation about a [110] axis, arrows of figure 2(b), to produce an orthorhombic distortion. In this structure, the Cu occupy octahedral sites.

Both Cu(II) and low-spin Cu(III) are also stable in square-pyramidal or square-coplanar sites, which allows the layered copper oxides to accommodate to a large family of structures. A

smaller A-site cation stable in eightfold oxygen coordination may form an A′ layer rather than an AO layer when placed between two CuO_2 layers. Loss of oxygen from the A′ layer leaves the A′ ion in eightfold oxygen coordination. The coppers of the CuO_2 layers are in square-pyramidal coordination where they are adjacent to an AO layer on one side and an A′ layer on the other; they are in square-coplanar coordination where they have two adjacent A′ layers. Moreover, other layers may be inserted between two AO layers; these layers may have variable oxygen content that allows oxidation of the CuO_2 layers without changing either the oxygen coordination of any of the Cu atoms of a CuO_2 sheet or the A atoms of adjacent AO or A′ layers. If we represent the layers between two AO sheets by Φ, then the p-type superconductors may be represented by designation of the successive layers that are encountered on traversing the *c*-axis:

$$\mathrm{AO \cdot CuO_2 \cdot AO} \tag{2a}$$

$$\mathrm{\Phi \cdot AO \cdot CuO_2 \cdot AO \cdot \Phi} \tag{2b}$$

$$\mathrm{\Phi \cdot AO \cdot CuO_2 \cdot A' \cdot CuO_2 \cdot AO \cdot \Phi} \tag{2c}$$

$$\mathrm{\Phi \cdot AO \cdot CuO_2 \cdot A' \cdot CuO_2 \cdot A' \cdot CuO_2 \cdot AO \cdot \Phi} \tag{2d}$$

$$\mathrm{\Phi \cdot AO \cdot CuO_2 \cdot A' \cdot CuO_2 \cdot A' \cdot CuO_2 \cdot A' \cdot CuO_2 \cdot AO \cdot \Phi} \tag{2e}$$

in which A′ is a smaller rare earth or Y or Ca, and A is a larger A-site atom such as Ba, Sr, Pb or La. In this representation, $La_{2-x}Sr_xCuO_4$ is given by (2*a*) and oxidation of the CuO_2 layer is accomplished by substitution of Sr^{2+} for La^{3+}.

The $YBa_2Cu_3O_{6+x}$ (YBCO) structure of figure 3 is given by representation (2*c*). The Y^{3+} ions occupy the A′ layer and the Cu(III)/Cu(II) of the CuO_2 sheets are in square-pyramidal oxygen coordination. The two BaO layers are bridged by linearly coordinated Cu(I) in the parent compound $YBa_2Cu_3O_6$; oxidation occurs by introducing oxygen into the layer of bridging copper to form chains of corner-shared square-coplanar Cu(III)/Cu(II). The Cu(III)/Cu(II) redox band of the $\Phi = CuO_x$ chains overlaps that of the CuO_2 sheets, and the chain segments are, therefore, commonly referred to as a charge-reservoir layer [7].

The $Tl_{2-y}Ba_2CuO_{6-x}$, $Tl_{2-y}Ba_2CaCu_2O_{8-x}$ and $Tl_{2-y}Ba_2Ca_2Cu_3O_{10-x}$ structures of figure 4 are described by the representations (2*b*)–(2*d*). In this family, Ca^{2+} ions occupy the A′ layers while the larger Ba^{2+} ions occupy the AO layers; the $\Phi = Tl_{2-y}O_{3-x}$ layer between the BaO sheets accepts electrons from the CuO_2 sheets, particularly from the copper in fivefold oxygen coordination, to produce p-type conduction in the CuO_2 sheets [8, 9].

The bismuth compounds $Bi_2Sr_2CuO_{6+x}$ and $Bi_2Sr_2CaCu_2O_{8+x}$ represented by (2*b*) and (2*c*) are members of an analogous family containing Sr in place of Ba. In this case, $\Phi = Bi_2O_{2+x}$ layers [10, 11] accommodate extra oxygen to oxidize the CuO_2 sheets. The Bi and O atoms are displaced considerably from their ideal positions to form ladder-like structures in the Bi_2O_{2+x} layers [12, 13]. This family has been extensively studied by surface-sensitive techniques such as photoemission spectroscopy (PES) because of the ease with which the Bi_2O_{2+x} layer can be cleaved and the passivity of a BiO_{1+y} surface.

Figure 5 shows the $YBa_2Cu_4O_8$ structure [14]; it can be derived from that of $YBa_2Cu_3O_{6+x}$ (figure 3) by replacing the $\Phi = CuO_x$ chains with a double Cu–O chain. As prepared, this superconductive compound has its CuO_2 sheets underoxidized (underdoped). However, a large pressure dependence of T_c, $dT_c/dP = 0.55$ K kbar^{-1} [15], has been shown to result from transfer of electrons from the CuO_2 sheets to the double Cu–O chains of the Φ layer [16]. A compound $YBa_2Cu_{3.5}O_{7.5}$ consists of combining figures 3 and 5 into alternating layers of $YBa_2Cu_3O_7$ and $YBa_2Cu_4O_8$ [17, 18].

The $Pb_2Sr_2R_{1-z}Ca_zCu_3O_{8+x}$ (R = lanthanide or Y) is another example of a structure closely related to that of $YBa_2Cu_3O_{6+x}$. As shown in figure 6, the $\Phi = CuO_x$ layers of

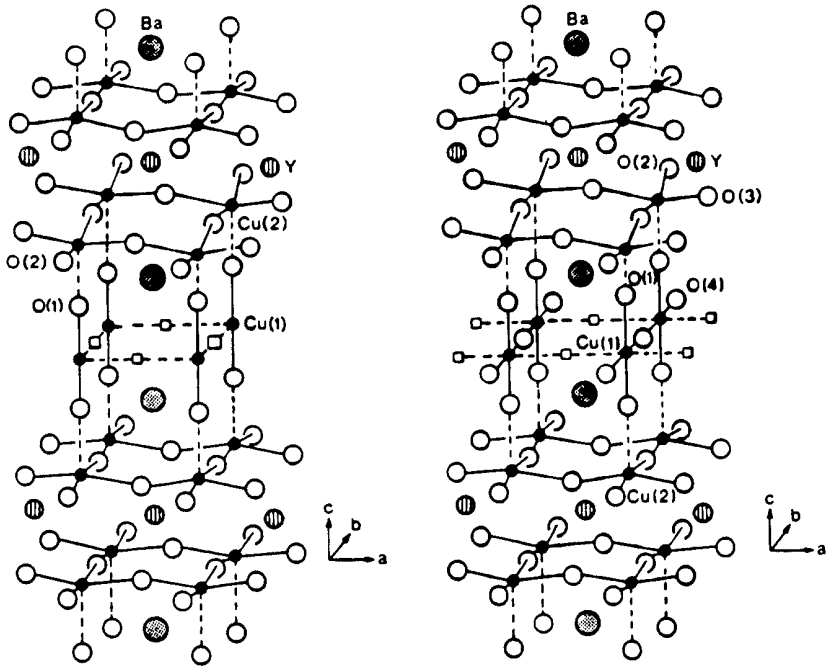

Figure 3. Structures of (a) tetragonal $YBa_2Cu_3O_6$ and (b) ideal orthorhombic $YBa_2Cu_3O_7$.

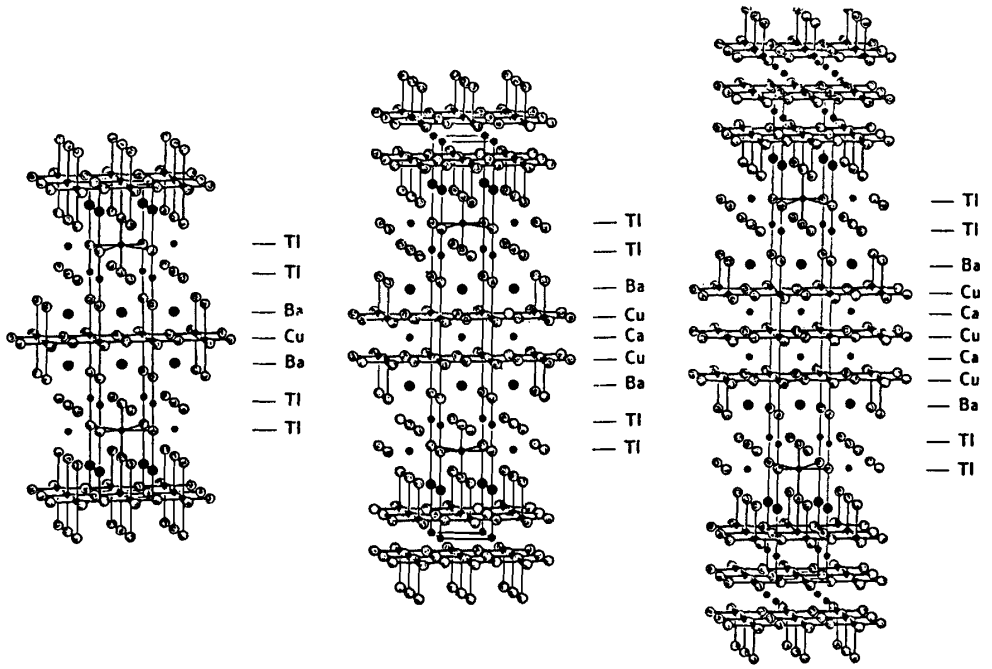

Figure 4. Structures of ideal (a) $Tl_2Ba_2CuO_6$, (b) $Tl_2Ba_2CaCu_2O_8$ and (c) $Tl_2Ba_2Ca_2Cu_3O_{10}$.

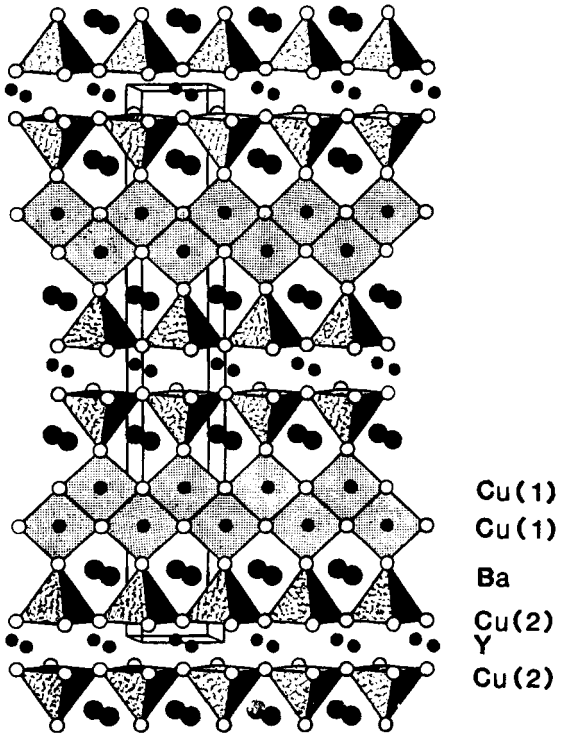

Figure 5. $YBa_2Cu_4O_8$.

$YBa_2Cu_3O_{6+x}$ are replaced by PbO–Cu–PbO layers. Partial substitution of Ca^{2+} for R^{3+} in the A′ plane is necessary in this case to introduce p-type charge carriers into the CuO_2 sheets so as to make them superconductive [19, 20].

The highest values of the superconductive critical temperature ($T_c \approx 131$ K) have been found in the trilayer mercury compounds $Hg_{1-y}M_yBa_2Ca_2Cu_3O_{8+x}$ of figure 7 [21]; in representation (2*d*), A′ = Ca and $\Phi = Hg_{1-y}M_yO_x$. The mercury compounds have 180° Cu–O–Cu bonds in the CuO_2 sheets, which limits the oxidation of these sheets by the interstitial oxygen in the Hg layers of the original $HgBa_2Ca_2Cu_3O_{8+x}$ compound [22] since oxidation reduces the equilibrium Cu–O bond length. By choosing the size of the M cation and its valence, substitution for Hg of M cations of higher oxidation state (e.g. M = Bi, Tl, Mo and/or Re) that bring extra oxygen into the Hg planes not only stabilizes the phase; it also allows optimization of both the oxidation state and the Cu–O bond length of the superconductive CuO_2 sheets.

Like $YBa_2Cu_3O_{6+x}$ of figure 3, the structure of $RuSr_2GdCu_2O_8$ corresponds to representation (2*c*) in which A′ = Gd and A = Sr; the $\Phi = RuO_2$ plane between the SrO rock-salt layers is reported to have a ferromagnetic component below a magnetic-ordering temperature $T_M = 133$ K [23–27]. Since superconductivity and ferromagnetism are mutually exclusive, the implication of this finding is that the superconductive electronic state of the high-T_c cuprates is two dimensional. This conclusion is supported by the observation that the RuO_2 planes are conductive in the normal state, but they do not become superconductive below T_c; the RuO_2 planes and CuO_2 layers are apparently decoupled [28]. The RuO_2 planes contain nearly as many Ru^{4+} as Ru^{5+} ions [29, 30] and thus act as a charge reservoir that oxidizes the CuO_2 sheets. A rotation of the Ru octahedral sites about the *c*-axis bends the Ru–O–Ru in-

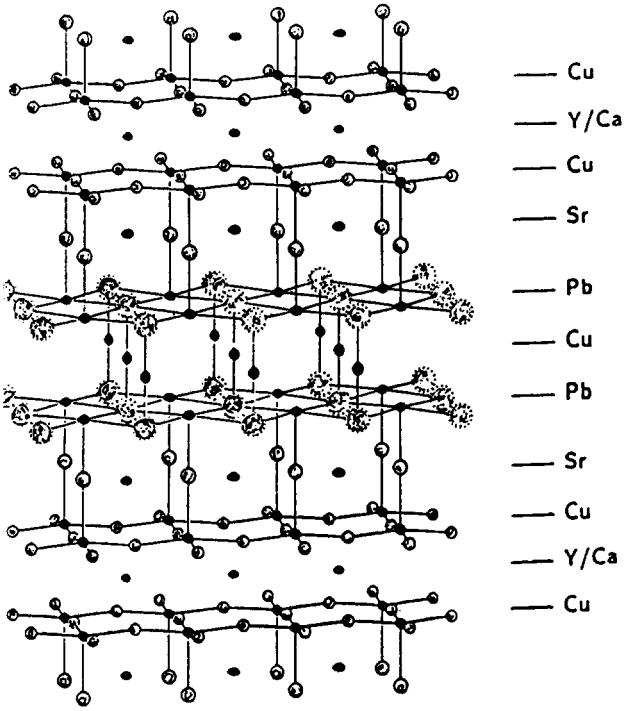

Figure 6. Structure of $Pb_2Sr_2Y_{1-z}Ca_zCu_3O_8$.

plane bonds to $(180° - \phi)$, which narrows the π^* RuO_2 band and creates an antiferromagnetic coupling between Ru atoms with a canted-spin ferromagnetism [31–33] that increases with an applied magnetic field [34].

In summary, the layered copper oxides have been found to exhibit a remarkable ability to oxidize layers containing CuO_2 sheets in a variety of ways without changing the oxygen coordination of the Cu atoms of a sheet even though the Cu atoms of a given sheet may occupy octahedral, square-pyramidal or square-coplanar sites. Where the oxygen coordination or its orientation varies from Cu to Cu in a CuO_2 sheet, superconductivity is suppressed by the resulting perturbation of the two-dimensional (2D) periodic potential. The presence of two different A or A′ cations in adjacent layers perturbs the periodic potential to a lesser extent; it lowers the critical temperature T_c without completely suppressing superconductivity. The superconductivity of the copper oxides occurs in the CuO_2 sheets and appears to be a 2D phenomenon although coupling along the c-axis also occurs. This anisotropic character of the copper oxide superconductors has made processing of these oxides for technical applications difficult. The formal number of Cu(III)/Cu atom (i.e. number of positive charge carriers per Cu atom) in a CuO_2 sheet that gives the highest value of T_c for a given p-type system is always in the range 0.15–0.18; at this state of oxidation, the superconductors all appear to be single phase below T_c. Although a given system may have a large range of oxidation states at higher temperatures, the superconductive phases are all confined to a narrow range of oxidation states of the CuO_2 sheets. The superconductive phase is thus seen to be a thermodynamically distinguishable phase that is stabilized at low temperatures at a crossover from localized to itinerant electronic behaviour [35]. Compositions lying between the parent antiferromagnetic-insulator phase and the superconductive phase are said to be ‘underdoped’, those between the

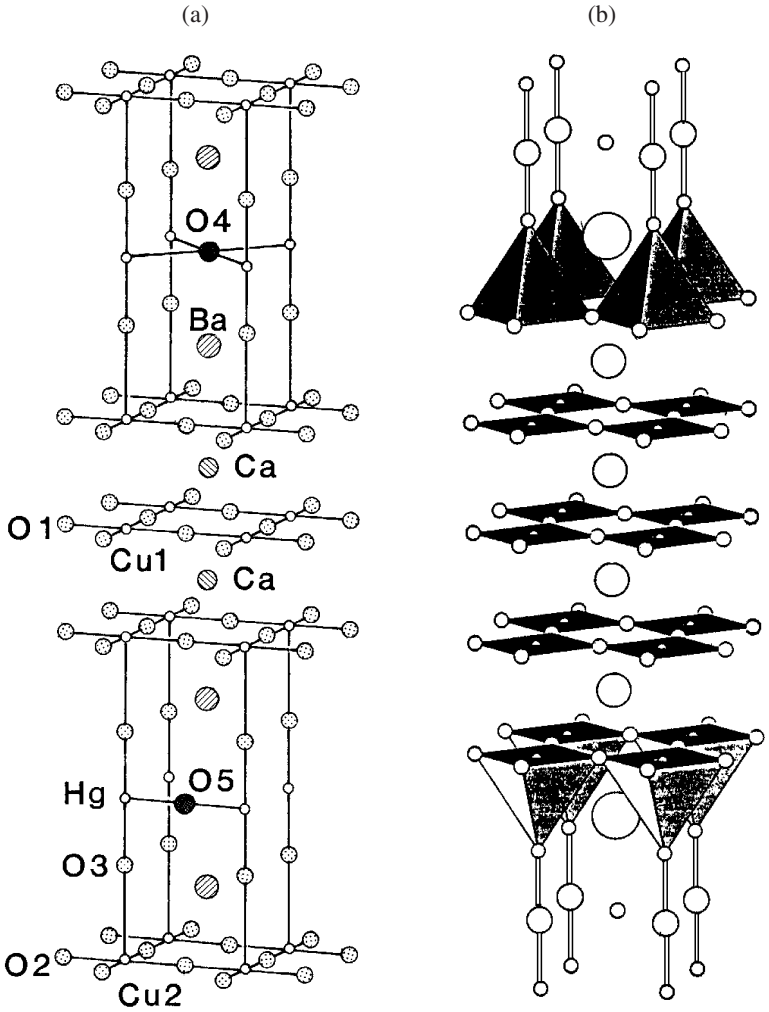

Figure 7. Structures of $HgBa_2Ca_{n-1}Cu_nO_{2n+2+\delta}$ for (a) $n = 3$ and (b) $n = 5$.

highest-T_c superconductive phase and the Fermi-liquid (FL), non-superconductive phase to be overdoped.

2.2. The n-type superconductors

Where the CuO_2 sheets are under a compressive stress as occurs with a tolerance factor $t < 1$, oxidation of the sheets relieves this stress by shortening the equilibrium Cu–O bond length; reduction of the sheets would increase a compressive stress. Where the CuO_2 sheets are under tensile stress as occurs with a $t > 1$, reduction of the CuO_2 sheets relieves the stress; oxidation would increase the stress. Where the Cu–O bond length in the sheets has the equilibrium value for a Cu(II) ion, it proves difficult to dope the sheets either p-type or n-type. Therefore, a given layered copper oxide system may be doped p-type or n-type, but not both [36]. Two structures in which the parent compounds have stretched 180° Cu–O–Cu bonds and have been made n-type superconductors are the T′-tetragonal structure of figure 8(a) and the infinite-layer structure of figure 9(b).

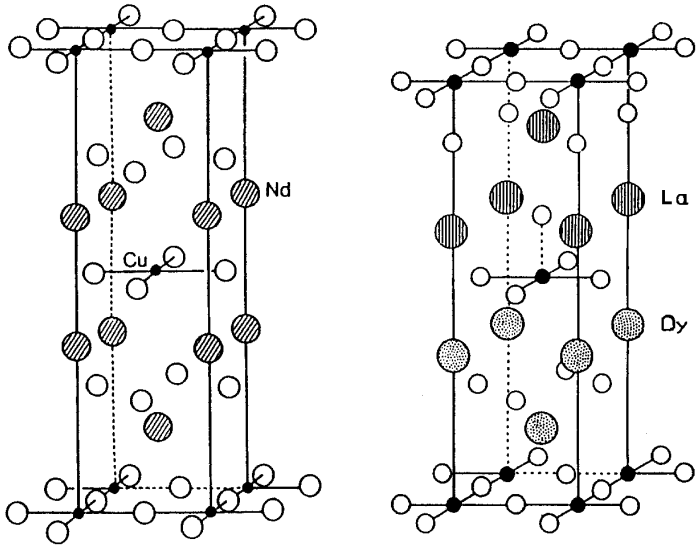

Figure 8. Structure of (a) T′-tetragonal Nd_2CuO_4 and (b) T*-tetragonal $LaDyCuO_4$.

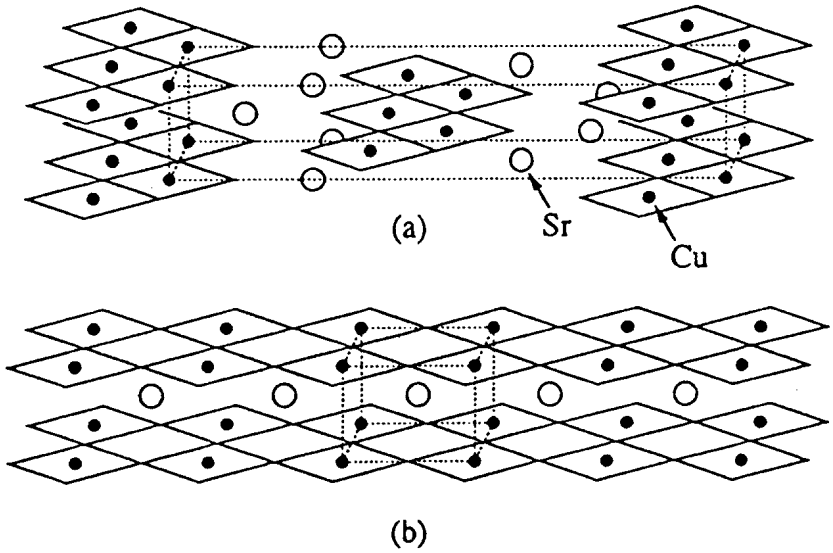

Figure 9. Comparison of the (a) atmospheric-pressure and (b) high-pressure forms of $SrCuO_2$.

The T′-tetragonal structure is derived from the tetragonal/orthorhombic (T/O) La_2CuO_4 structure of figure 3 by the displacement of the oxygen atoms of two adjacent AO rock-salt sheets into the intersheet A-cation tetrahedral sites to form an A–O_2–A fluorite layer in place of the two AO·AO rock-salt sheets [37]. Removal of the apical oxygen at the square-pyramidal Cu sites of the La_2CuO_4 structure leaves CuO_2 planes of corner-shared square-coplanar sites. The equilibrium basal-plane lattice parameter of a fluorite layer is larger than that of the rock-salt layer and transforms the compressive stress on the octahedral-site CuO_2 sheets of the T/O La_2CuO_4 structure to a tensile stress on the square-coplanar CuO_2 planes of the T′ structure. The relative magnitudes of the elastic energies due to these two types of strain

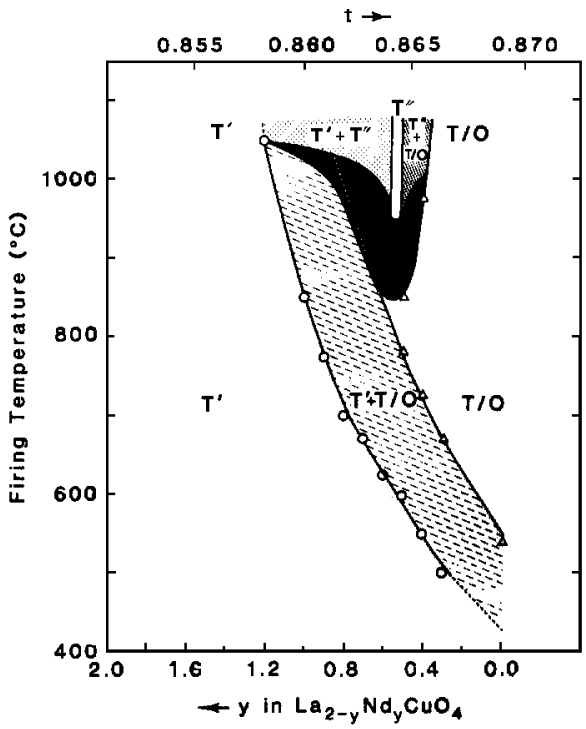

Figure 10. The stability ranges of the T′ versus T/O structure in the system $La_{2-y}Nd_yCuO_4$ prepared at different firing temperatures. The room-temperature tolerance factors for different values of y are also shown, after [38].

determine which structure is stabilized. A smaller A-site cation, i.e. a smaller tolerance factor t, favours the T′ structure as is illustrated in figure 10 for the system $La_{2-y}Nd_yCuO_4$ obtained at different firing temperatures starting from oxalate precursors [38]. By increasing the firing temperature, it was possible to increase the critical value of y at which the transition from the T/O to the T′ phase occurred. The calculated value of the room-temperature tolerance factor decreases with increasing y, but t increases with temperature. Therefore, if the transition occurs at a critical value of $t = t_c$, then the plot of figure 10 shows how t increases with temperature. La_2CuO_4 compounds with the T′ structure have been prepared at atmospheric pressure for Ln = Pr $\cdots$ Gd [37], and partial substitution with Dy has been able to reduce the room-temperature Cu–O bond length in this structure to 1.94 Å. With the exception of Gd_2CuO_4, these compounds have been made n-type superconductors by substitution of smaller Ce^{4+} [39] or Th^{4+} [40] ions for La^{3+} or F^- for O^{2-} in the fluorite layer [41]. These substitutions do not change the oxygen coordination at a Cu site. However, any O^{2-} ions remaining on the apical-site positions introduce fivefold oxygen coordination at some Cu sites, which perturbs the periodic potential of the CuO_2 planes sufficiently to suppress superconductivity.

At small n-type doping of the $Ln_{2-x}Ce_xCuO_4$ systems with the T′ structure, the electronic charge carriers remain small polarons in an antiferromagnetic phase up to a critical doping concentration x_c where there is a first-order transition to a superconductive phase. However, the appearance of superconductivity requires synthesis or subsequent annealing in an inert atmosphere or under pressure to ensure removal of apical oxygen from all the Cu atoms. The smaller the lanthanide ion Ln^{3+}, the higher is x_c. The superconductive phase occurs at an electron concentration $0.14 < x < 0.17$ similar to the hole concentration in the p-type

superconductors; and x_c increases with decreasing size of the Ln^{3+} ion, which diminishes the compositional range in which superconductivity is found, see section 5.1.

Figure 10 suggests that a preparation below 400 °C might stabilize La_2CuO_4 in the T′ structure. However, the oxygen ions are not mobile at these temperatures, and the large compressive stress on the CuO_2 sheets of La_2CuO_4 is partially relieved by the distortion from T-tetragonal to O-orthorhombic symmetry on lowering the temperature. In air or O_2 atmosphere, the compressive stress is also partially relieved by the introduction of interstitial oxygen. The interstitial oxygen is, surprisingly, mobile to well below room temperature, and phase segregation into oxygen-rich and oxygen-poor regions below room temperature creates filamentary superconductivity in the oxygen-rich regions of $La_2CuO_{4+\delta}$ [42–48]. The interstitial oxygens occupy the tetrahedral A-site positions between the two LaO sheets of the rock-salt layers [49]. Substitution of the larger Sr^{2+} ion for La^{3+} in $La_{2-x}Sr_xCuO_4$ relieves the compressive stress on the CuO_2 sheets sufficiently that interstitial oxygen is not introduced in air for $x > 0.1$. However, these observations emphasize the importance of monitoring the oxygen content of all the copper oxide superconductors.

The tetragonal T* structure of figure 8(b) is found where two A cations of quite different size are present in the A_2CuO_4 compounds [50–52]; it is a hybrid of figures 3 and 8(a) containing fluorite layers alternating with rock-salt layers. In $LaDyCuO_4$, for example, the fluorite layers are Dy rich and the rock-salt layers are La rich; this ordering minimizes the bond-length mismatch between successive layers. With this arrangement, the Cu of single CuO_2 sheets become fivefold coordinated. In this structure, it has only been possible to oxidize the CuO_2 sheets.

In the infinite-layer structure of $A'CuO_2$, figure 9(b), planes of corner-shared square-coplanar Cu sites alternate with A′ planes. This structure was first obtained by Siegrist *et al* [53] with the compound $Ca_{0.86}Sr_{0.14}CuO_2$. However, synthesis at atmospheric pressure allows little variation of the Ca/Sr ratio. In $SrCuO_2$, for example, the large Sr^{2+} ion breaks apart the CuO_2 planes and the CuO_2 double chains of figure 9(a) are formed instead. Attempts to dope $Ca_{0.86}Sr_{0.14}CuO_2$ sufficiently to make either an n-type or a p-type superconductor were unsuccessful; the Cu–O bond length of 1.93 Å is near the equilibrium value for the Cu(II) ion; and in the infinite-layer structure of figure 9(b), bond-length mismatch is not accommodated by either cooperative bending of the 180° Cu–O–Cu bonds or stretching of the Cu–O bonds. However, pressure decreases the Cu–O equilibrium bond length, and Takano *et al* [54] synthesized $SrCuO_2$ with the infinite-layer structure of figure 9(b) under a pressure of 25 kbar; this phase was stable at atmospheric pressure and room temperature even though the Cu–O bond length was stretched at ambient to 1.965 Å. This result led Smith *et al* [55] to prepare under pressure n-type superconductors in two infinite-layer systems, $Sr_{1-y}Nd_yCuO_2$ and $Sr_{1-y}Pr_yCuO_2$. The equilibrium Cu–O bond length increases with n-type doping, and superconductivity appeared for $y \geqslant 0.14$, showing that the superconductive phase is also stabilized here in the range $0.14 \leqslant n \leqslant 0.18$ electrons/Cu atom. This finding was quickly confirmed by Er *et al* [56] who demonstrated n-type superconductivity in the $Sr_{1-y}La_yCuO_2$ system prepared under pressure.

Arima *et al* [57] have plotted the relationship between the Cu–O bond length for the La_2CuO_4 oxides and the structure, the possible doping type, and the bandgap of the parent compound, figure 11. The clear break at 1.93 Å shows the influence of the bond length on the type of doping and the structure; whether the oxygen coordination of the Cu atoms also influences the type of doping has not been articulated or demonstrated. The influence of the variance $\sigma* \equiv \langle r_A^2\rangle - \langle r_A\rangle^2$ of the atomic radii r_A of the A cations has also been investigated [58, 59]; the variance plays a smaller role and does not change the qualitative conclusions from figure 11.

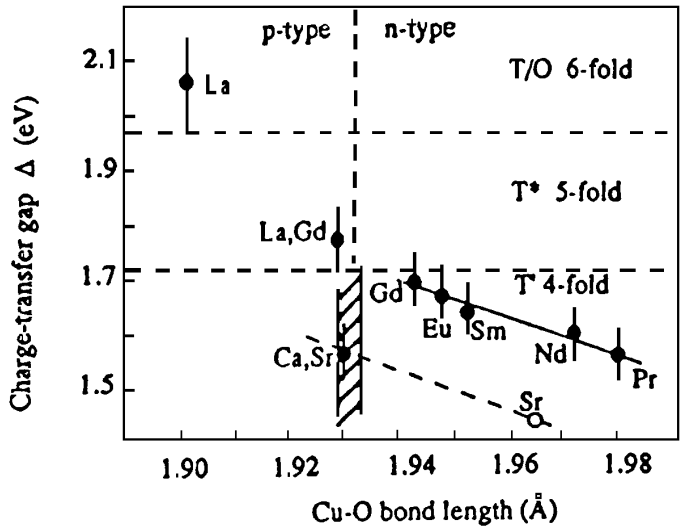

Figure 11. Charge-transfer gap versus Cu–O bond length for Ln_2CuO_4 oxides, after [57].

3. Electronic considerations

3.1. Overview

It is useful to consider three quite different classes of metal oxides: the main group oxides, the rare-earth oxides and the d-block transition-metal oxides.

The main-group elements have only s and p electrons in partially filled shells, and only these valence electrons are active in bonding. With the exception of $5s^2$ and $6s^2$ lone-pair core electrons, the s and p electrons are itinerant and occupy primarily O^{2-}:$2p^6$ bonding bands that are separated from empty antibonding, primarily cation s and p bands by a large energy gap in the case of ns and np cation bands with $n \leqslant 4$. Cations such as Sn and Sb with outer 5s and 5p orbitals active in bonding have an intermediate-size energy gap between bonding and antibonding s and p bands, and their oxides may be reduced by introducing electrons into their 5s bands; but in this case, disproportionation reactions generally isolate these electrons as $5s^2$ lone pairs at a single reduced-cation site. A similar situation generally applies to the 6s electrons of Tl, Pb and Bi; but as counter-cations in a transition-metal oxide, an overlap of the 6s-electron energies and a transition-metal redox couple may play an important role in broadening the d-electron band or, as in the Tl copper oxides, providing a charge reservoir for the transition-metal redox couple.

The $4f^n$ configurations at the lanthanide atoms Ln are localized, and the intra-atomic electron–electron Coulomb energies between 4f electrons are large, $U_{fn} > 6$ eV. Consequently the Ln atoms can only have a single valence state unless a $4f^n$ configuration happens to fall in the energy gap between the filled O 2p bands and empty cationic antibonding bands. In the copper oxide superconductors, the lanthanide 5d orbitals are empty and are at energies well above the Fermi energy, which is near the top of the O 2p bands. In these oxides, cerium is Ce^{4+} and all the other Ln ions are Ln^{3+} with the possible exception of praesodymium, which has a Pr^{4+}/Pr^{3+} couple near, but generally below the Fermi energy. Hybridization of the Cu 3d and Pr $4f^2$ orbitals may remove the spin degeneracy at the Fermi energy, thereby suppressing formation of singlet Cooper pairs and superconductivity.

In perovskite-related oxides containing a 3d-block transition-metal atom M, the antibonding electrons of M 3d parentage may be either localized or itinerant [60]. It is imperative to understand the nature of the transition from localized-to itinerant-electronic behaviour if one wishes to describe the high-T_c phenomenon in the copper oxides since this phenomenon is found at the crossover from localized-electron antiferromagnetism in a parent single-valent Cu(II) compound to itinerant-electron behaviour in the overdoped compositions. For this purpose, it is convenient to begin with the construction of ligand-field 3d orbitals; this construction introduces the oxygen component into the antibonding orbitals that arises from M–O bonding.

The on-site Coulomb energy U that separates successive redox couples is responsible for localizing electrons in single-valent compounds; the interatomic M–O–M interactions in a perovskite-related structure are responsible for suppressing U and converting the localized-electron configurations into itinerant electrons occupying an energy band of width W. In a single-valent compound, the crossover from localized to itinerant electronic behaviour occurs where $W \approx U$.

In a mixed-valent compound, charge carriers tunnel from site to site in a time $\tau_h \approx \hbar/W$, and the bandwidth W narrows sharply as W changes from $W > U$ to $W < U$. Holes or electrons introduced into a redox couple of a localized-electron configuration hop from site to site in a time $\tau_h > \omega_o^{-1}$, where ω_o^{-1} is the period of an optical-mode oxygen vibration, and the charge carriers are polaronic. Small dielectric polarons are mobile electrons or holes that are dressed in oxygen displacements that trap them at a single site before they have time to hop to a neighbouring like atom. Therefore, small polarons move diffusively. Itinerant electrons, on the other hand, have a $\tau_h < \omega_o^{-1}$, which means they tunnel from site to site too rapidly to be trapped. Consequently they have dispersive energies $\varepsilon_k = \hbar^2 k^2/2m^*$ that span a bandwidth W and a mobility $\mu = e\tau_s/m^*$, where τ_s is the mean free time between scattering events. The crossover from polaronic to itinerant electronic behaviour occurs where $\tau_h \approx \omega_o^{-1}$; strong electron–lattice coupling means the attempt frequency for an electron hop is $\nu_o > \tau_h^{-1}$. In this case, the charge carriers move with little or no motional enthalpy; the charge-carrier motion is *vibronic*. The result is bad-metal behaviour in which the charge carriers are coupled strongly to fluctuating, cooperative oxygen-atom displacements, but they are not trapped by local oxygen displacements; the vibronic charge carriers have a Fermi surface.

In a single-valent compound with $W < U$, the spin–spin M–O–M interactions between localized-electron configurations are described by superexchange perturbation theory; in the itinerant-electron limit $W > U$, the bandwidth W_b can be described by the tight-binding theory, which neglects U. In the crossover region $W_b \approx U$, it is not possible to neglect the influence of U; it increases the effective mass of the quasiparticles and narrows the bandwidth W. Hubbard introduced a theory providing a smooth crossover with a progressive opening of an energy gap between successive redox energies in a single-valent system as W decreased to $W < U$. However, recent experiments indicate that the crossover is not smooth, and the virial theorem will be used to argue for a first-order transition at crossover. A first-order transition leads to phase segregation where segregation occurs at a high enough temperature for atomic diffusion, which proves to be the case in $La_2CuO_{4+\delta}$ where the interstitial oxygens are mobile below room temperature. However, if the phase segregation would occur at too low a temperature for atomic diffusion, it is manifest in cooperative bond-length fluctuations. The lattice instabilities associated with these fluctuations and the resulting vibronic conductivity are found in the normal state of the copper oxide superconductors. Moreover, in these mixed-valent systems, the two-phase fluctuations also manifest themselves in the formation of mobile 'correlation bags' that act as multicentre polarons having a diffusive, vibronic mobility with $\Delta H_m < kT$ at temperatures $T > T_c$.

3.2. Ligand-field considerations

The five 3d orbitals of a free atom are degenerate; but with more than one electron or hole in a 3d manifold, the spin degeneracy is removed by the ferromagnetic direct-exchange interaction between electron spins in orthogonal atomic orbitals. These exchange interactions produce the Hund intra-atomic exchange field H_{ex}. The energy splitting between a high and a lower localized spin state will be designated Δ_{ex}.

The atomic orbitals f_m with azimuthal orbital angular momentum operator L_z, where $L_z f_m = -\mathrm{i}\hbar(\partial f/\partial\phi) = \pm m\hbar f_m$, have the angular dependences

$$\begin{aligned} f_0 &\sim (\cos^2\theta - 1) \sim [(z^2 - x^2) + (z^2 - y^2)]/r^2 \\ f_{\pm1} &\sim \sin 2\theta \exp(\pm\mathrm{i}\phi) \sim (yz \pm \mathrm{i}zx)/r^2 \\ f_{\pm2} &\sim \sin^2\theta \exp(\pm\mathrm{i}2\phi) \sim [(x^2 - y^2) \pm \mathrm{i}xy]/r^2. \end{aligned} \tag{3}$$

In an isolated octahedral site, the xy and $(yz \pm \mathrm{i}zx)$ orbitals only overlap the neighbouring O $2p_\pi$ orbitals while the $[(z^2 - x^2) + (z^2 - y^2)]$ and $(x^2 - y^2)$ orbitals only overlap the O $2p_\sigma$ and 2s orbitals. The resonance integrals $b^{ca} \equiv (f_m, H'\phi_o) \approx \varepsilon_{mo}(f_m, \phi_o)$ describing the energy of a virtual charge transfer to an empty M = 3d orbital from the same-symmetry sum of near-neighbour oxygen orbitals ϕ_o contain both an overlap integral (f_m, ϕ_o) and a one-electron energy ε_{mo}; these integrals are larger for σ-bonding than for π-bonding, which makes $b^{ca}_\sigma > b^{ca}_\pi$.

If the Madelung energy of a point-charge ionic model of a crystal places the lowest empty 3d orbital of a degenerate manifold an energy ΔE_p above the O 2p orbitals and ΔE_s above the O 2s orbitals, the antibonding d-like states may be described in second-order perturbation theory to give the ligand-field wavefunctions

$$\begin{aligned} \psi_t &= N_\pi(f_t - \lambda_\pi\phi_\pi) \\ \psi_e &= N_\sigma(f_e - \lambda_\sigma\phi_\sigma - \lambda_s\phi_s) \end{aligned} \tag{4}$$

where the symmetry designations t and e distinguish the threefold-degenerate manifold of π-bonding orbitals. Equation (4) is valid provided the covalent-mixing parameters $\lambda_\sigma \equiv b^{ca}_\sigma/\Delta E_p$ or $\lambda_\pi \equiv b^{ca}_\pi/\Delta E_p$ are much smaller than unity. A larger ΔE_s keeps $\lambda_s \ll \lambda_\sigma$ where equation (4) is applicable. According to second-order perturbation theory, the M–O interaction raises the antibonding states by an energy

$$\Delta\varepsilon = |b^{ca}|^2/\Delta E. \tag{5}$$

A $b^{ca}_\sigma > b^{ca}_\pi$ raises the antibonding e-orbital manifold above the π-orbital manifold by an energy Δ_c, and this cubic-field splitting is

$$\Delta_c = \Delta\varepsilon_\sigma - \Delta\varepsilon_\pi = \Delta_M + (\lambda^2_\sigma - \lambda^2_\pi)\Delta E_p + \lambda^2_s\Delta E_s \tag{6}$$

where Δ_M is a purely electrostatic term of uncertain sign due to the penetration of the O^{2-}-ion electron cloud by the cation 3d wavefunctions. If ΔE_p for a particular manifold becomes too small or b^{ca} too large, the perturbation expansion breaks down, and an isolated MO_6 complex must be treated in molecular-orbital theory, an array of corner-shared octahedra by band theory.

The cubic-field splitting Δ_c is the same order of magnitude as the intra-atomic exchange energy Δ_{ex}, and the $d^4 - d^7$ configurations may be either high-spin t^3e^1, t^3e^2, t^4e^2, t^5e^2 where $\Delta_{ex} > \Delta_c$ or low-spin t^4e^0, t^5e^0, t^6e^0, t^6e^1 where $\Delta_c > \Delta_{ex}$. The covalent mixing of O 2p wavefunctions into ψ_t and ψ_e lowers the intra-atomic exchange splitting Δ_{ex} and increases Δ_c. Therefore, stronger covalent mixing stabilizes low-spin relative to high-spin configurations.

For localized-electron manifolds where ligand-field theory is applicable, successive redox energies are split by an on-site electrostatic energy U to add an electron to a d^n manifold to make it d^{n+1}. In an octahedral site, the effective energy U_{eff} must take into account Δ_c and Δ_{ex}.

For example, $U_{\rm eff}$ for $n = 3$ and 8 is increased by Δ_c if $\Delta_c < \Delta_{ex}$ and by Δ_{ex} if $\Delta_c > \Delta_{ex}$; for $n = 5$ it is increased by Δ_{ex} if $\Delta_c < \Delta_{ex}$, and for $n = 6$ by Δ_c if $\Delta_c > \Delta_{ex}$. Moreover, if the top of the O 2p bands lies in the gap U between successive redox energies in a point-charge model, the lower redox couple becomes pinned at the top of the O 2p bands and the effective gap between the pinned redox couple and the upper couple is referred to as a charge-transfer gap $\Delta E_p < U$.

If the cubic crystalline field leaves an orbital degeneracy as occurs with e^1 configurations, for example, the degeneracy may be removed by a Jahn–Teller distortion of the site to lower symmetry. These distortions order the occupied orbital. In a solid, cooperative orbital ordering lowers the symmetry of the crystal, but disordered orbital fluctuations introduce a local crystal-field splitting of the degeneracy and an important electron coupling to bond-length fluctuations.

3.3. M–O–M interactions

In perovskite-related structures with 3d-block transition-metal atoms M, the dominant interactions between d-like orbitals centred at neighbouring M atoms are the $(180° - \phi)$ M–O–M interactions. The spin-independent resonance integrals describing charge transfer between M atoms at R_i and R_j are

$$\begin{aligned} b_\pi^{cac} &\equiv (\psi_{ti}, H'\psi_{tj}) \approx \varepsilon_\pi \lambda_\pi^2 \\ b_\sigma^{cac} &\equiv (\psi_{ei}, H'\psi_{ej}) \approx \varepsilon_\sigma \lambda_\sigma^2 \cos\phi \end{aligned} \tag{7}$$

where λ_π varies with the acidity of the A cations as well as with the bending angle ϕ and H' is the perturbation of the potential at R_j caused by the presence of an M atom at R_i. The smaller term $\varepsilon_s \lambda_s^2$ is omitted from b_σ^{cac} for simplicity.

In the itinerant-electron limit, the on-site energy U is reduced by screening from the other electrons to a value $U \ll W$, and tight-binding band theory for itinerant electrons ignores U to give a bandwidth

$$W = W_b \approx 2zb^{cac} \tag{8}$$

where z is the number of like nearest neighbours. Moreover, the time for an electron to tunnel from one atom to another in this limit is $\tau_h < \omega_o^{-1}$, where ω_o^{-1} is the period of the optical-mode vibration that would trap an electronic charge carrier in a mixed-valent system at a single M atom; therefore, the charge-carrier mobility is

$$\mu = e\tau_s / m* \tag{9}$$

where τ_s is the mean time between scattering events and m^* is the effective mass of the charge carrier. Introduction of a finite U into the theory enhances m^* and narrows W.

In the localized-electron limit, a single-valent compound is an insulator with an electron bandwidth $W < U$; a mixed-valent compound has a $\tau_h > \omega_o^{-1}$, which allows the lattice to trap a charge carrier at a single site as a small dielectric polaron. Small polarons move diffusively with a mobility

$$\mu = (eD_o/kT)\exp(-\Delta G_m/kT) \tag{10}$$

where $\Delta G_m = \Delta H_m - T\Delta S_m$ is the motional free energy and the motional enthalpy ΔH_m is the activation energy required for a charge carrier to overcome the trapping energy so as to jump to a neighbouring site.

Where there are localized spins on neighbouring sites, it is necessary to introduce spin-dependent resonance integrals; with an angle θ_{ij} between spins at R_i and R_j, these integrals are

$$t_{ij}^{\uparrow\uparrow} = b^{cac}\cos(\theta_{ij}/2) \qquad \text{and} \qquad t_{ij}^{\uparrow\downarrow} = b^{cac}\sin(\theta_{ij}/2) \tag{11}$$

for parallel and antiparallel coupling of near-neighbour spins [61]. Since the spin angular momentum is conserved in an electron transfer, a real charge transfer in a mixed-valent system gives a *ferromagnetic double-exchange* interaction where $\Delta H_m < kT$ allows fast electron transfer between near neighbours:

$$\Delta\varepsilon_{ex}^{\uparrow\uparrow} \approx -czt_{ij}^{\uparrow\uparrow} = -czb^{cac}\cos(\theta_{ij}/2). \tag{12}$$

Small-polaron conductors have too slow an electron transfer for the double-exchange reaction to be applicable; however, where fast electron transfer occurs within a multicentre polaron, ferromagnetic double exchange couples the spins within the multicentre polaron. Multicentre polarons may be stabilized at the crossover from localized to itinerant electronic behaviour of the σ-bonding e electrons, and double exchange is operative in the presence of localized t^3 configurations with spin $S = 3/2$ as is illustrated by the manganese oxide perovskites $Ln_{1-x}A_xMnO_3$ (A = alkaline earth) exhibiting a colossal negative magnetoresistance [61], see the discussion of figure 27 in section 4.

In a single-valent compound, virtual charge transfers from one M atom to a near neighbour give *superexchange* spin–spin interactions. Interactions between half-filled orbitals are constrained by the Pauli exclusion principle to be *antiferromagnetic*; and the virtual charge transfers are described in second-order perturbation theory as [60, 61]

$$\Delta_{ex}^{s} = -|t_{ij}^{\uparrow\downarrow}|^2/U_{\text{eff}} = \text{constant} + J_{ij}S_i \cdot S_j \tag{13}$$

where $J_{ij} \sim (2b_{ij}^2/4S^2U_{\text{eff}})$ and $b_{ij} = b^{cac}$. There is, in addition, a *semicovalent exchange* arising from the transfer of two electrons from the same O 2p orbital, one to the M atom on one side and the other to the M atom on the other side. Since the two electrons in the O 2p orbital are spin paired, this interaction is *antiferromagnetic* where the receptor orbitals on the two neighbouring atoms having localized spins are both half filled or both empty. Thus the sign of the superexchange and semicovalent-exchange interactions are the same [63]. Since the O 2p electrons are itinerant, the cost to transfer two electrons is $2\Delta E_p$ [64] and addition of the semicovalent component changes the J_{ij} of equation (13) to

$$J_{ij} \sim (2b_{ij}^2/4S^2)[U_{\text{eff}}^{-1} + (2\Delta E_p)^{-1}] \tag{14}$$

where only the semicovalent exchange is operative if the receptor orbitals are both empty. Moreover, where a localized-electron redox couple becomes pinned at the top of the O 2p band, which corresponds to the charge-transfer-gap situation of the Zaanen–Sawatzky–Allen [65] treatment, the charge-transfer gap is $\Delta = \Delta E_p < U_{\text{eff}}$ and the semicovalent exchange component may be dominant. In this case a $W > \Delta E_p$ is sufficient to introduce itinerant electrons that screen the on-site energy U, making $W > U$, and the 3d electrons occupy a narrow itinerant-electron antibonding band pinned at the top of the O 2p bands. This situation is encountered in the p-type copper oxide superconductors. Figure 12 illustrates the change in $\Delta_\sigma = \Delta E_p$ for $YCrO_3$, $LaMnO_3$ and $CaMnO_3$, the change in the measured energy gap [66], and a schematic representation of the superexchange versus semicovalent virtual charge transfers [67].

Superexchange and semicovalent spin–spin exchange interactions between a half-filled and an empty orbital on a cation with a localized spin are ferromagnetic and are treated in third-order perturbation theory since electron transfer to an empty orbital is not constrained by the Pauli exclusion principle; transfer to the empty orbital of a spin parallel to a localized spin on the receptor cation is stabilized by the intra-atomic exchange energy Δ_{ex} [60]. In the case of e^1–O–e^1 interactions between high-spin Mn^{3+}:t^3e^1 ions, for example, the t^3 configurations give a localized spin $S = 3/2$ and orbital order of the e electrons introduces 2D ferromagnetic e^1–O–e^0 interactions in the (001) planes of $LaMnO_3$ and antiferromagnetic t^3e^0–O – t^3e^0

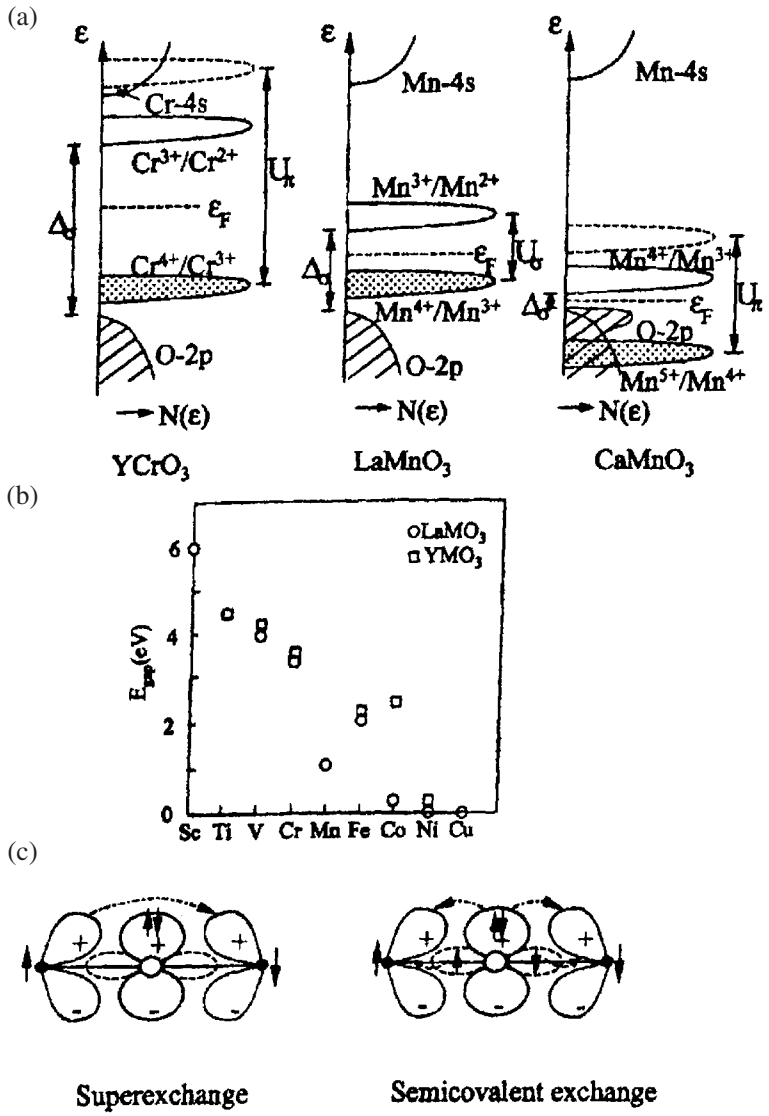

Figure 12. (a) Schematic energy diagrams for $YCrO_3$, $LaMnO_3$ and $CaMnO_3$. (b) The charge-transfer gap $\Delta = \Delta E_p$ measured by optical spectra, from [66]. (c) Virtual electron transfers for 180° t^3e^0–O–t^3e^0 interactions in Anderson superexchange and semicovalent exchange.

interactions between planes [68], but orbital fluctuations give rise to a vibronic (quasistatic) 3D ferromagnetic superexchange interaction [69, 70].

Conventional theory for single-valent compounds is based on the assumption that the transition from localized to itinerant electronic behaviour is smooth with the progressive opening of an energy gap U between successive redox energies as the bandwidth W narrows from $W > U$ to $W < U$; the insulator–metal transition at $W \approx U$, illustrated in figure 13 for a half-filled band, is known as the Mott–Hubbard transition. However, this theory neglects electron–lattice interactions. Brinkman and Rice [71], for example, have predicted that as the Mott–Hubbard transition is approached from the itinerant-electron side, the electron effective

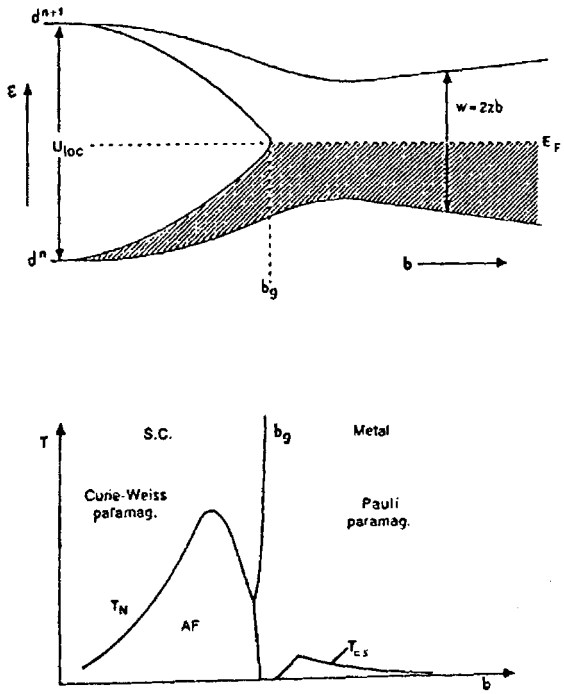

Figure 13. Schematic evolution with resonance integral b^{cac} of the one-electron energies in the Mott–Hubbard single-phase description for a half-filled band and the associated phase diagram for a smooth transition at $b = b_g$. Note: SC = semiconductor, T_{CS} = superconductive critical temperature.

mass $m_{e-e}{}^*$ due to on-site electron–electron interactions increases from the bare-electron mass $m_b{}^*$ as

$$m_{e-e}{}^*/m_b{}^* = [1 - (U/U_c)^2]^{-1} \tag{15}$$

where U_c is the value of U at the Mott–Hubbard transition. However, this mass-enhancement expression becomes infinite at $U = U_c$, and nature avoids infinities. It does so by undergoing a first-order transition from the itinerant-electron regime to the localized-electron (or strongly correlated itinerant-electron) regime with localized spins [72–74]. The basis for a first-order transition between the two regimes is most easily argued from the virial theorem of mechanics.

According to the virial theorem for a system of particles of mean kinetic energy $\langle T \rangle$ and potential energy $\langle V \rangle$ in central-force fields,

$$2\langle T \rangle + \langle V \rangle = 0. \tag{16}$$

Electrons in a solid are bound, which makes $\langle V \rangle < 0$. Since the volume occupied by an electron increases discontinuously on going from the localized to the itinerant electronic regime, $\langle T \rangle$ decreases discontinuously and therefore, from equation (16), $|\langle V \rangle|$ must also decrease discontinuously. A discontinuous decrease in $|\langle V \rangle|$ for antibonding electrons in an oxide is accomplished by a discontinuous decrease in the equilibrium M–O bond length, which results in a first-order transition with

$$(\text{M–O})_{\text{localized}} > (\text{M–O})_{\text{itinerant}}. \tag{17}$$

This deduction has several experimentally testable consequences.

(1) Conventional phase segregation into a structure containing itinerant electrons and a structure with localized electrons may prevent investigation of the evolution of physical properties with changing bandwidth at the crossover.
(2) Where phase segregation would occur at too low a temperature for atomic diffusion, locally cooperative bond-length fluctuations may segregate mobile, itinerant-electron clusters within a localized-electron matrix or mobile localized-electron clusters in an itinerant-electron matrix. The former have been called *correlation bags* [75], the latter *strong-correlation fluctuations* [74]. Alternatively, the two phases may coexist in nearly equal proportions to give rise to locally cooperative bond-length fluctuations; this situation corresponds to QCP behaviour. The bond-length fluctuation may order at lower temperatures into a static CDW, e.g. a disproportionation of 2 Fe(IV) into $Fe(V)O_6$ σ-bonding molecular-orbital clusters and localized Fe(III) configurations in $CaFeO_3$ [76], or they may stay disordered to lowest temperature, e.g. at crossover in the system $Ln_{0.5}A_{0.5}MnO_3$ (Ln = lanthanide, A = alkaline earth) [77]. In the copper oxide superconductors, the bond-length fluctuations may order into stripes of itinerant electrons alternating with stripes of localized spins, which corresponds to a CDW, or they may transform stripes containing bosonic clusters into heavy quasiparticles that open a superconductive gap at the Fermi surface.
(3) The coexistence of two fluctuating phases changes the bandwidth from the tight-binding W_b narrowed by mass enhancement to a narrower vibronic band [78]

$$W = W_b \exp(-\lambda\varepsilon_{sc}/\hbar\omega_o) \tag{18}$$

where ε_{sc} is the stabilization of a strong-correlation fluctuation or, in a mixed-valent compound, an electron-rich localized-electron phase relative to a hole-rich itinerant-electron phase; $\lambda \sim \varepsilon_{sc}/W_b$ is a measure of the strength of the electron–lattice coupling. Since $\omega_o = \omega_o(\phi)$ changes with the bending of the $(180° - \phi)$ M–O–M bond angle, W varies more sensitively with ϕ than $W_b \approx 2z\varepsilon_\sigma\lambda_\sigma^2 \cos\phi$ from equations (7) and (8), for example.
(4) A double-well potential at crossover makes the (M–O) bond exceptionally compressible, and the pressure dependence of the tolerance factor becomes $dt/dP > 0$ rather than the normal $dt/dP < 0$ associated with a more compressible (A–O) bond.
(5) Bond-length fluctuations suppress the phonon contribution to the thermal conductivity.
(6) In the case of two-phase fluctuations, but not of a QCP phase, PES spectra would reveal the coexistence of two types of electron from the same atomic 3d manifold, one occupying a lower Hubbard band ($W < U$ in figure 13) and the other a coherent itinerant-electron band with a normal dispersion of the one-electron energies ε_k. Moreover, spectral weight would be transferred from the coherent band to the lower Hubbard band on narrowing the bandwidth W. The transfer of spectral weight would open a pseudogap in the density of states that changes progressively to a real energy gap as the band narrows to where only the localized-electron phase remains.
(7) Strong electron–lattice interactions would introduce a vibronic charge-carrier mobility

$$\mu \approx eD_o/kT \tag{19}$$

at higher temperatures resulting in bad-metal behaviour with a linear increase with temperature of the resistivity to high temperatures.
(8) Pressure would stabilize the itinerant-electron phase relative to the localized-electron phase.
(9) In the absence of localized spins in another manifold, the magnetic susceptibility for two-phase fluctuations would evolve from Curie–Weiss paramagnetism to Pauli paramagnetism

with increasing W by a progressive increase of the volume fraction of the Pauli paramagnetic phase.

4. Crossover from localized to itinerant electronic behaviour in some perovskites

4.1. The system $Ca_{1-x}Sr_xVO_3$

The single-valent d^1 system $Ca_{1-x}Sr_xVO_3$ illustrates the introduction of strong-correlation fluctuations on the approach to the crossover from localized to itinerant electronic behaviour from the itinerant-electron side. In this system, the bandwidth is increasing with increasing x. The system is metallic without long-range magnetic order for all x, but $CaVO_3$ becomes antiferromagnetic if the oxygen stoichiometry is not maintained. Figure 14 shows PES data from Inoue *et al* [73] for the 3d electrons of this system. Whereas a band calculation for the V^{4+}:$3d^1$ electrons of the VO_3 array (top of the figure) shows an antibonding π^* band of t-orbital parentage ($W_\pi \approx \varepsilon_\pi \lambda_\pi^2$) that is one-sixth filled, the PES spectra show the coexistence of two types of 3d electron and a progressive transfer of spectral weight with increasing x from a lower Hubbard band to a partially filled band of coherent electron states having a well defined Fermi energy. These data provide direct evidence for the coexistence of two electronic phases in a system that appears to be single phase to a diffraction experiment. The electrons in the lower Hubbard band can be identified as belonging to strong correlation fluctuations in a percolating itinerant-electron matrix, the volume fraction of strongly correlated electrons increasing progressively as the bandwidth decreases on the approach to long-range magnetic order in $CaVO_3$ [74]. Consistent with this interpretation was the observation that pressure, by stabilizing the itinerant-electron phase at the expense of the volume fraction of strong-correlation fluctuations, anomalously increases both the room-temperature thermoelectric power α(296 K) and the low-temperature phonon-drag component, whereas the $\alpha(T)$ data for Pt showed the expected decrease in α(296 K) and no change in the low-temperature phonon-drag component [74]. This observation provides, therefore, an indirect signature of the existence of strong-correlation fluctuations in an itinerant electron matrix of a metallic phase exhibiting no long-range magnetic order.

4.2. The system $La_{1-x}Nd_xCuO_3$

$LaCuO_3$ is a metallic perovskite that is prepared under high oxygen pressure. In a point-charge ionic model, the Madelung energy is not large enough to lift the Cu(III):t^6e^2 level above the O^{2-}:$2p^6$ level, so the antibonding σ^* band states of e-orbital parentage are pinned at the top of the O 2p bands with a dominant O 2p character. This σ^* band is half filled. Attempts to narrow the bandwidth sufficiently to induce stabilization of an antiferromagnetic phase in $La_{1-x}Nd_xCuO_3$ were unsuccessful; it was not possible to obtain the perovskite phase for $x > 0.6$. However, the pressure dependence of the thermoelectric power $\alpha(T)$ showed the signature of strong-correlation fluctuations even in the parent $LaCuO_3$ compound, and the paramagnetic susceptibility of the CuO_3 array (after subtraction of the Na^{3+}-ion contribution) showed an increase with x, figure 15, in the volume fraction of a phase with Curie–Weiss behaviour coexisting with a Pauli paramagnetic phase [79].

4.3. $LaMnO_3$

The compound $LaMnO_3$ contains high-spin Mn(III):t^3e^1 electrons; the localized-electron e^1 configuration has a twofold orbital degeneracy that is removed by a local Jahn–Teller distortion of the octahedral site from cubic to tetragonal or orthorhombic symmetry. The t^3

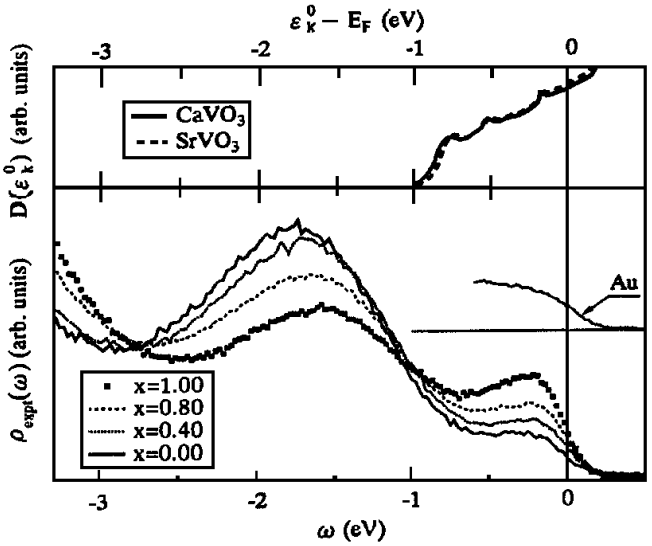

Figure 14. Top: density of one-electron states of $CaVO_3$ and $SrVO_3$ calculated by the APW method. Bottom: measured photoemission spectra $\rho_{expt}(\omega)$ of $Ca_{1-x}Sr_xVO_3$ taken with $h\upsilon = 50$ eV, after [73].

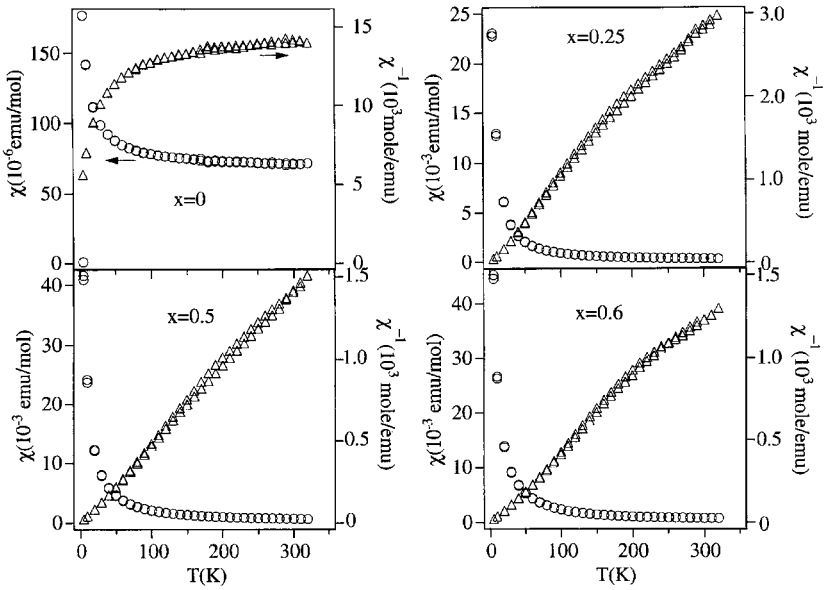

Figure 15. Temperature dependence of molar magnetic susceptibility $\chi(T)$ and its inverse, $\chi^{-1}(T)$, for the CuO_3 array of $La_{1-x}Nd_xCuO_3$, after [79].

configuration remains localized with a spin $S = 3/2$ whereas there is a transition from localized to itinerant behaviour of the e electrons in $La_{1-x}Sr_xMnO_3$ in the range $0.08 \leqslant x \leqslant 0.20$ below the magnetic-ordering temperature [80]. In the parent compound $LaMnO_3$, the localized e^1 configuration approaches the transition to itinerant-electron behaviour from the localized-electron side.

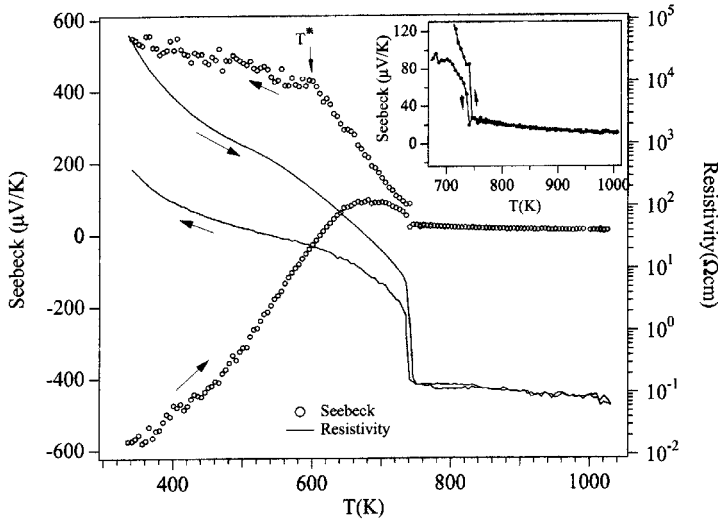

Figure 16. Resistivity $\rho(T)$ and thermoelectric power $\alpha(T)$ taken on cycling a virgin single crystal of $LaMnO_3$ from room temperature to 1020 K measured in a vacuum of 10^{-3} Torr, after [82].

Figure 16 shows the resistivity $\rho(T)$ and thermoelectric power $\alpha(T)$ of a single crystal of $LaMnO_3$ as measured in a vacuum of 10^{-3} Torr [81]. An irreversible change in the room-temperature $\alpha(300\ \mathrm{K})$ from -600 to about $+550\ \mu\mathrm{V\ K^{-1}}$ on thermal cycling to 1020 K reflects a small-polaron conduction. Initially, the crystal contains a small fraction $c = 0.0009$ of Mn(II) ions; but on heating above 500 K, it becomes oxidized to a similarly small fraction of Mn(IV) ions on the MnO_3 array. The $\rho(T)$ and $\alpha(T)$ curves were reversible after the first cycle. The second significant feature of figure 16 is a sharp drop in both $\alpha(T)$ and $\rho(T)$ on heating to above an orbital order–disorder transition at T_{JT}. Below T_{JT}, the twofold-degenerate e^1 configurations order into the (001) planes as a result of a cooperative Jahn–Teller distortion of the local octahedral sites that give dominant ferromagnetic $e^1 \cdots$ O–e^0 interactions within (001) planes and antiferromagnetic t^3e^0–O–t^3e^0 interactions between (001) planes. However, above T_{JT} where the occupied e orbitals fluctuate, breathing-mode oxygen displacements also occur at individual $MnO_{6/2}$ sites; these breathing-mode displacements induce a disproportionation 2 Mn(III) = Mn(II) + Mn(IV) that generates mobile negative and positive electronic charge carriers in equal proportion, which is why both $\rho(T)$ and $\alpha(T)$ decrease. The data further suggest that short-range bond-length fluctuations with some disproportionation set in within an orbitally ordered matrix in the range $T^* \approx 600\ \mathrm{K} < T < T_{JT}$.

Tobe *et al* [83] have reported the optical conductivity for a detwinned $LaMnO_3$ crystal at several temperatures, figure 17. The data show a reduction of the energy gap with increasing temperature and its disappearance above the orbital-ordering temperature $T_{oo} = T_{JT}$. Significantly, above T_{JT} where $LaMnO_3$ is conductive, there is no Drude component in the optical conductivity; $LaMnO_3$ becomes a *vibronic* conductor with $\tau_h \approx \omega_o^{-1}$, not an itinerant-electron metal with $\tau_h < \omega_o^{-1}$, at temperatures $T > T_{JT}$ where closing of the energy gap at the Fermi energy allows partial, fluctuating disproportionation of 2 Mn(III) into Mn(II) and Mn(IV). Opening of the energy gap between the Mn(IV)/Mn(III) and Mn(III)/Mn(II) redox couples is, in this case, accomplished by ordering of occupied, localized e^1 orbitals below T_{JT}; at $T > T_{JT}$, the electronic charge carriers remain sufficiently localized that they couple strongly to locally cooperative oxygen vibrations that deform the $MnO_{6/2}$ octahedra. This situation is to

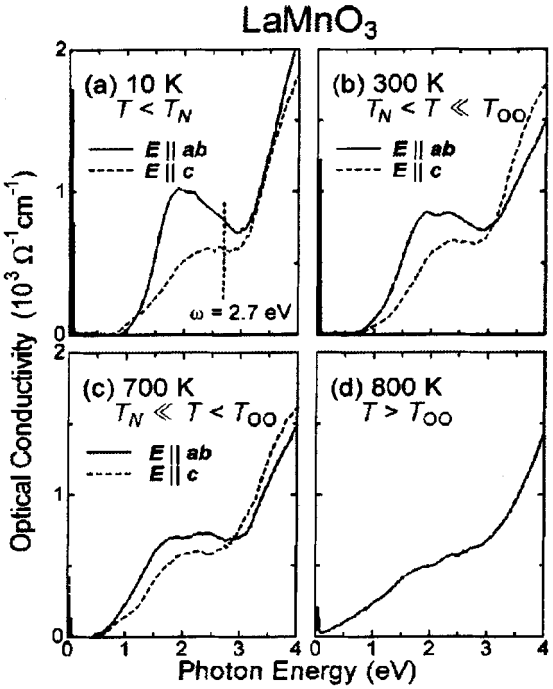

Figure 17. Optical conductivity spectra for $E \parallel ab$ (solid curves) and $E \parallel c$ (dashed curves) of a detwinned $LaMnO_3$ crystal at representative temperatures: (a) 10 K $< T_N$, (b) $T_N <$ 300 K $< T^*$, (c) $T^* <$ 700 K $< T_{TJ}$ and (d) 800 K $> T_{JT}$. Note: $T_{oo} = T_{JT}$, after [83].

be contrasted with that of isoelectronic $CaFeO_3$ where a gap in the σ^* conduction band is opened up by stabilization of an ordered disproportionation reaction [76] 2 Fe(IV) = Fe(V) + Fe(III) in which the empty e orbitals of an $Fe(V)O_6$ cluster form molecular orbitals and the e^2 electrons of the Fe(III) ions are localized; the ordered arrangement of alternating $Fe(V)O_6$ clusters and Fe(III) ions creates a 'negative-U' CDW. Fluctuations between the right-and left-hand sides of the disproportionation reaction provide an order parameter that reflects an increase in stabilization of the ordered disproportionation as the temperature is lowered.

Given this evidence that $LaMnO_3$ approaches a transition from localized to itinerant electronic behaviour, it became of interest to probe how the Néel temperature varies with pressure. Chemical pressure can be exerted by substituting a smaller lanthanide for La in $LnMnO_3$, but this approach changes primarily the $(180° - \phi)$ Mn–O–Mn bond angle. Hydrostatic pressure, on the other hand, changes the equilibrium (Mn–O) bond length. Bloch [84] had studied the variation of the Néel temperature T_N with volume V for numerous antiferromagnetic insulators and had found the general relationship

$$\alpha_B \equiv \mathrm{d}\log T_N/\mathrm{d}\log V = -3.3 \pm 0.4. \tag{20}$$

This relationship, known as Bloch's rule, applies in the localized-electron limit where the interatomic spin–spin interaction is described by superexchange plus semicovalent-exchange perturbation theory with $T_N \sim \sum'_{ij} J_{ij}$ from equation (14), for example. Theoretical justification of this rule came from calculation of $b^{ca} \sim r^{-n}$, which gave $n = 2.5$–3.0 for an (M–O) bond length r [85, 86]. If U_{eff} and ΔE_p of equation (14) are pressure-independent, it follows that $T_N \sim r^{-10} \sim V^{-3.3}$. Furthermore, if the compressibility $K \equiv -V^{-1}\partial V/\partial P$ remains constant, the pressure dependence of T_N should conform to Bloch's rule. Therefore,

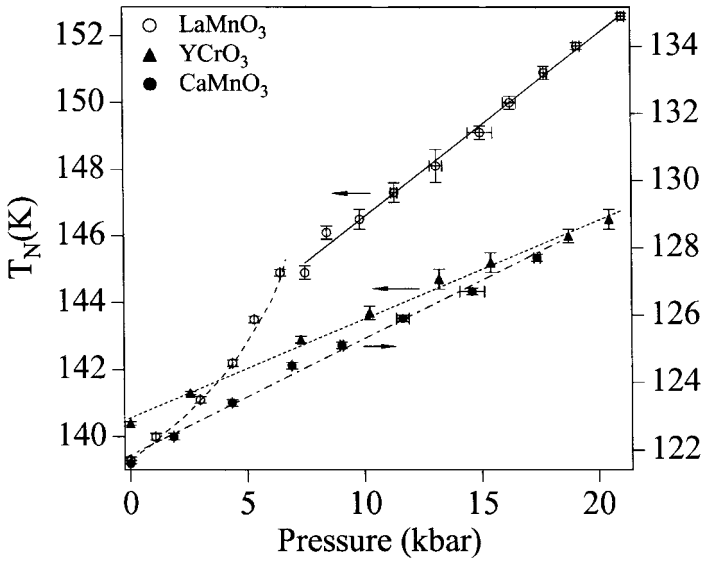

Figure 18. Pressure dependence of the Néel temperature of $LaMnO_3$, $YCrO_3$ and $CaMnO_3$, after [87].

any deviation from Bloch's rule would be an indication that U_{eff} and/or ΔE_p are decreasing with increasing pressure. Since we may write

$$\alpha_B = K^{-1} T_N^{-1} (\mathrm{d}T_N/\mathrm{d}P) \tag{21}$$

α_B is obtained experimentally by measuring T_N versus P and the compressibility K. Figure 18 compares $T_N(P)$ for $LaMnO_3$, $CaMnO_3$ and $YCrO_3$, all of which have comparable compressibilities [87]. An $\alpha_B = -5.3$ for $LaMnO_3$ above 7 kbar is to be compared with an $\alpha_B = -3.8$ and -3.0, respectively, for $CaMnO_3$ and $YCrO_3$. Moreover, a non-linear increase of T_N with P below 7 kbar is terminated by a two-phase region; not only is the variation of T_N with P anomalously high, it is also not monotonic. Thus the approach to the localized to itinerant electronic transition from the localized-electron side also provides evidence for a first-order phase transition in a single-valent perovskite with $[U_{\text{eff}}^{-1} + \Delta E_p^{-1}]$ increasing discontinuously as the gap between successive redox couples narrows.

4.4. The $RNiO_3$ family (R = Y or lanthanide)

An early neutron-diffraction study of $LaNiO_3$ failed to find any magnetic order in $LaNiO_3$ [88]. This observation was clarified in 1965 [89] when it was demonstrated that $LaNiO_3$ is metallic with Ni(III) in the low-spin state $t^6\sigma*^1$ as a result of strong Ni:e–O:2p covalent bonding. The Madelung energy is not large enough to raise the Ni(III)/Ni(II) couple above the top of the O^{2-}:$2p^6$ level in a point-charge model, which pins the antibonding states of the redox couple at the top of the O 2p bands with a dominant O 2p character. In the Zaanen–Sawatzky–Allen scheme [65], $LaNiO_3$ is classified as a charge-transfer-gap material with $\Delta E_p \approx 1$ eV $< U_{\text{eff}}$ and a σ^* band of e-orbital parentage having a bandwidth $W_\sigma > \Delta E_p$. A systematic study of other members of the $RNiO_3$ family was prevented at that time by an inability to prepare samples at atmospheric pressure. In 1991, Lacorre *et al* [90] succeeded in preparing under modest oxygen pressures (150–200 bar) sintered pellets of the $RNiO_3$ family from $LaNiO_3$ to $EuNiO_3$ that were convenient for transport measurements, and the phase diagram of figure 19

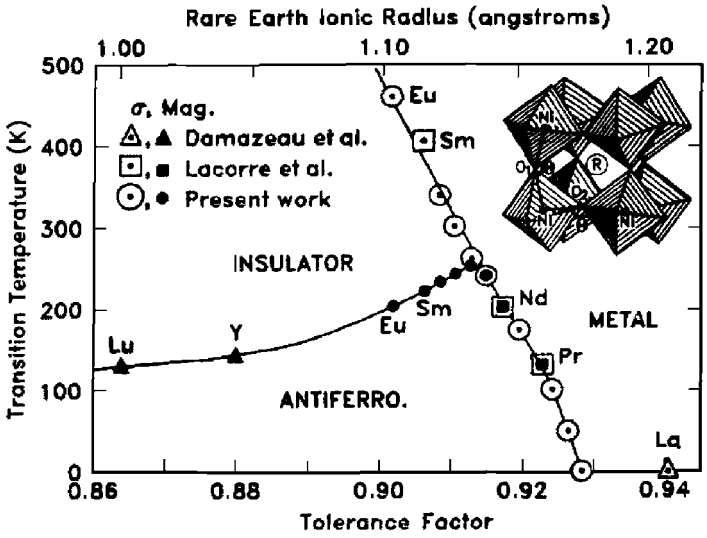

Figure 19. Insulator–metal-antiferromagnetic phase diagram for $RNiO_3$ as a function of the tolerance factor and (equivalently) of the ionic radius of the rare-earth ion R, after [91].

was reported soon after [91]. With decreasing ionic radius of the rare-earth ion R^{3+}, the equilibrium Ni–O bond length remains essentially constant, but the $(180^\circ - \phi)$ Ni–O–Ni bond angle decreases with decreasing tolerance factor t, which narrows the σ^* band. The Ni–O bond length increases discontinuously by about 0.2% on cooling through the insulator–metal transition [92], which is consistent with more localized electrons in the insulator phase in accordance with equation (17). Not shown in figure 19 is a transition from orthorhombic $Pbnm$ to rhombohedral $R\bar{3}c$ symmetry at a temperature T_{OR} between $PrNiO_3$ and $LaNiO_3$ [93].

The reported magnetic order below T_N is unusual [94, 95]; ferromagnetic (111) Ni layers are alternately coupled ferromagnetically and antiferromagnetically on traversing a pseudocubic [111] axis. However, this solution of the neutron data is not unique. Like the Mn(III):t^3e^1 and Fe(IV):t^3e^1 configurations, low-spin Ni(III):t^6e^1 also has a twofold e-orbital degeneracy that may be removed either by a local Jahn–Teller distortion of the octahedral site from cubic to tetragonal or orthorhombic symmetry as in $LaMnO_3$ or by a disproportionation reaction as in $CaFeO_3$. Alonso *et al* [96–98] have reported a distortion from orthorhombic to monoclinic $P2_1/n$ symmetry in $YNiO_3$ and the $RNiO_3$ compounds containing the heavier rare-earth ions. The monoclinic $P2_1/n$ structure contains two interpenetrating face-centred-cubic arrays of Ni sites distinguishable by different mean ⟨Ni–O⟩ bond lengths. A disproportionation of two low-spin Ni(III):t^6e^1 ions into diamagnetic Ni(IV)O_6 clusters and localized Ni(II):t^6e^2 configurations would give antiferromagnetic coupling between the Ni(II) spins across the clusters, a magnetic-order solution that is also compatible with the neutron data. Moreover, TEM, Raman scattering and x-ray absorption spectroscopy have shown that the $P2_1/n$ symmetry in the antiferromagnetic temperature range extends to $NdNiO_3$, but with a reduced discrimination between the two types of Ni site [99, 100]. Nevertheless, Rodriguez-Carvajal *et al* [95] have proposed two different Jahn–Teller distortions at the two distinguishable Ni sites that is claimed to account for the unusual magnetic order originally deduced from the neutron data. In either case, the interacting spins would be localized, and Medarde [93] has noted that samples with $T_N < T_t$ exhibit $T_N \sim \cos^2\phi$, a relation signalling localized-electron superexchange interactions according to equations (7), (11) and (13) since $T_N \sim \sum'_{ij} J_{ij}$.

This observation places localized spins on $SmNiO_3$ whereas metallic $LaNiO_3$ has itinerant electrons occupying a σ^* band of e-orbital parentage. Only a small change in tolerance factor, from $t \approx 0.968$ to 0.980, separates $SmNiO_3$ and the composition where the metal–insulator transition temperature T_t falls to zero. Therefore, this $RNiO_3$ family offers a rare opportunity to study the evolution of physical properties across the localized-to itinerant-electronic transition in a single-valent NiO_3 matrix containing one active 3d electron per Ni atom.

Although single crystals were not available, a technique to cold-press the polycrystalline sample yielded conductivities comparable to those obtained with single crystals [101]. Measurement of T_N versus P and compressibility gave a Bloch coefficient $\alpha_B \approx -5.5$, similar to that found for $LaMnO_3$ in the region $P > 7$ kbar. In addition, a two-phase region was found in the pressure range 15 kbar $< P <$ 20 kbar, showing that, in this case also, the approach to crossover from the localized-electron side is not monotonic; a first-order phase change introduces a two-phase region.

Figure 20 shows the pressure dependence of the resistivity $\rho(T)$ and thermoelectric power $\alpha(T)$ for four samples having tolerance factors in the crossover region [102]. The following features are noteworthy.

(1) Both the magnitude of α (296 K) and the low-temperature phonon-drag component of $\alpha(T)$ of $LaNiO_3$ increase with pressure. This feature proved to be a signature of the presence of strong-correlation fluctuations in $CaVO_3$, and its presence in the system $La_{1-x}Nd_xCuO_3$ allows a description of the evolution from Pauli to Curie–Weiss paramagnetism as the growth with x of the volume fraction of strong-correlation fluctuations. It is, therefore, to be anticipated that $LaNiO_3$, which approaches crossover from the itinerant-electron side, may also contain strong-correlation fluctuations.

(2) A $dT_t/dP < 0$ demonstrates an anomalous $dt/dP > 0$, which is characteristic of a double-well potential for the equilibrium (Ni–O) bond length; this feature is also consistent with the coexistence of two fluctuating electronic phases in samples that are single phase to a diffraction experiment.

(3) The resistivity at 15 K of $PrNiO_3$ drops progressively with increasing pressure by nearly six orders of magnitude over the range $0 < P <$ 14 kbar while T_t drops linearly from 145 to only 75 K. The return to metallic conductivity in the presence of a finite insulator–metal transition temperature T_t can be understood as an increase with pressure of the volume fraction of the metallic phase to beyond percolation in the presence of a percolating antiferromagnetic-insulator phase of larger volume. The $NdNiO_3$ and $Sm_{0.5}Nd_{0.5}NiO_3$ samples show the same trend, but with a volume fraction of the metallic phase that remains too small to reach percolation in pressures $P <$ 16 kbar.

(4) The decrease with pressure in the magnitude of the jump in $|\alpha(T)|$ on cooling through T_t also reflects a decrease in the volume fraction of the antiferromagnetic-insulator phase.

Figure 21 shows the evolution at ambient pressure of the magnetic susceptibility of the NiO_3 array, obtained by subtraction of the rare-earth contribution, for the four samples of figure 20 [103]; the data are compared with the $\rho(T)$ curves in order to locate T_t. Three features are noteworthy.

(1) The $\chi^{-1}(T)$ curve for $Nd_{0.5}Sm_{0.5}NiO_3$, figure 21(d), shows no anomaly at T_t as defined by $\rho(T)$. This observation demonstrates that the insulator–metal transition is not stabilized by either Fermi-surface nesting or the onset of a homogeneous Mott–Hubbard transition. However, it can be understood as an order–disorder transition of preexisting strong-correlation fluctuations in the metallic phase.

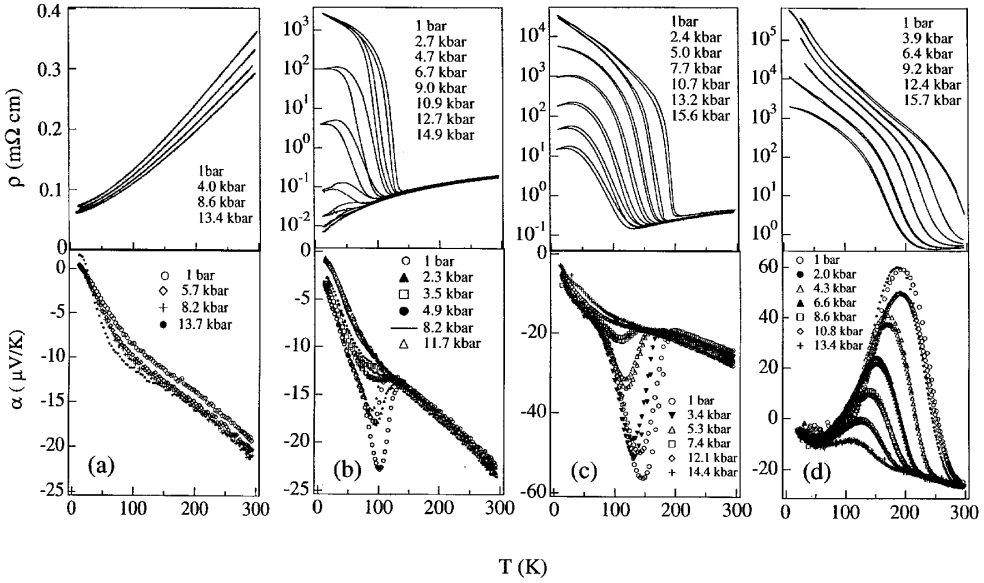

Figure 20. Resistivity $\rho(T)$ and thermoelectric power $\alpha(T)$ under different hydrostatic pressures for (a) $LaNiO_3$, (b) $PrNiO_3$, (c) $NdNiO_3$ and (d) $Sm_{0.5}Nd_{0.5}NiO_3$, after [102].

(2) Mott [104] predicted that flattening out of the one-electron ε_k versus k dispersion at the Fermi energy of a mass-enhanced metallic system would give a Pauli paramagnetism having a temperature dependence below a temperature T_d, but he was unable to find a suitable experimental example to test his prediction. Qualitatively, the $\chi(T)$ data for $LaNiO_3$ in figure 21(a) appears to fit the Mott prediction for a homogeneous electronic system. However, a weak temperature dependence persisting above the apparent $T_d \approx$ 200 K does not conform to the Mott picture. On the other hand, this $\chi(T)$ curve can be described by a model containing two electronic phases in which

$$\chi = \chi_p + \chi_{cw} \tag{22}$$

where χ_p is the susceptibility of a mass-enhanced, conductive FL phase with a $T_d \approx 200$ K and χ_{cw} is a Curie–Weiss component from strong-correlation fluctuations.

(3) The $\chi^{-1}(T)$ curves of figures 21(b) and (c) for $PrNiO_3$ and $NdNiO_3$ show only a small anomaly at $T_N = T_t$ in a field of 10 Oe. The Curie–Weiss component χ_{cw} above T_N increases with decreasing size of the R^{3+} ion and therefore with decreasing bandwidth W. The behaviour of $\chi(T)$ below T_N is not characteristic of a localized-electron antiferromagnet. The continuous increase of $\chi(T)$ with decreasing temperature below T_N is not attributable to spin canting since there is no difference between the $\chi(T)$ for field-cooled and zero-field-cooled samples. However, a metallic, non-percolating minority phase persisting below $T_t = T_N$ would give a Mott temperature-dependent χ_p below $T_d \approx 200$ K.

Figure 22 shows the thermal conductivity $\kappa(T)$ for cold-pressed $RNiO_3$ samples with R = La, Pr, Nd, Sm, Eu and Gd [100]. The electronic contribution $\kappa_e(T)$ of the metallic phases was calculated from the measured resistivities $\rho(T)$ and the Wiedemann–Franz law. Whereas a significant phonon contribution is apparent in $GdNiO_3$, $EuNiO_3$ and $SmNiO_3$ below T_N on the localized-electron side and in $LaNiO_3$ on the itinerant-electron side of the crossover

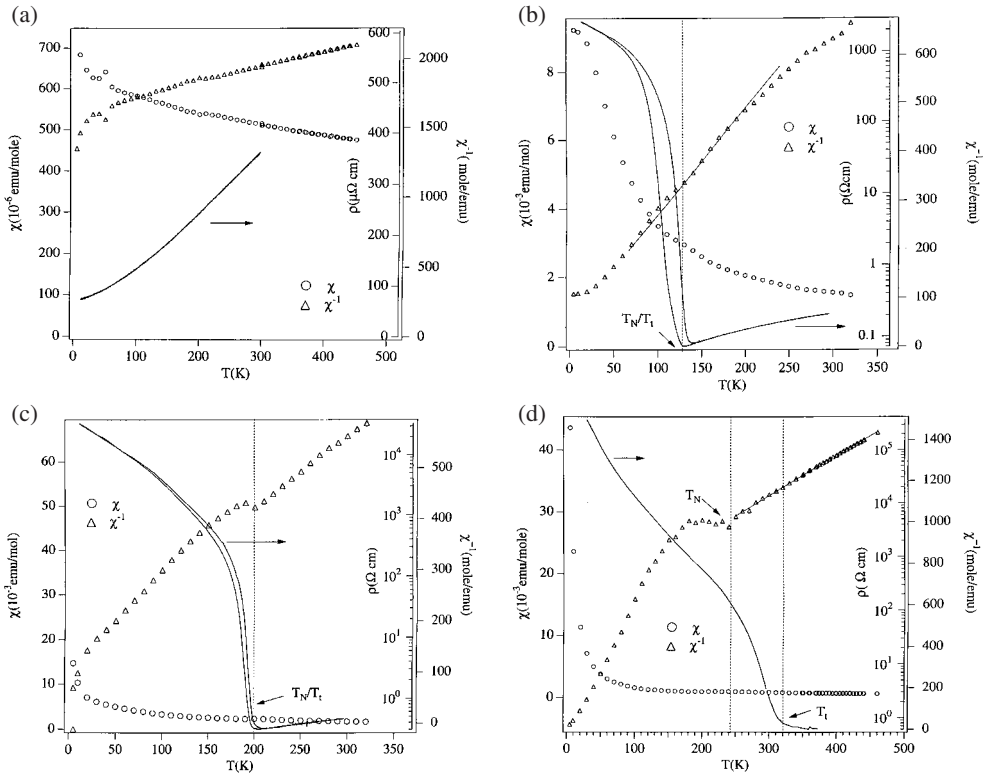

Figure 21. Temperature dependence of resistivity $\rho(T)$, magnetic susceptibility $\chi(T)$ and its inverse $\chi^{-1}(T)$ for the NiO_3 array of (a) $LaNiO_3$, (b) $PrNiO_3$, (c) $NdNiO_3$ and (d) $Sm_{0.5}Nd_{0.5}NiO_3$. The straight line in (d) is a linear fit to $\chi^{-1}(T)$ above T_N, after [103].

from localized to itinerant electronic behaviour, the phonons are dramatically suppressed in the crossover region. Figure 23 compares $\kappa(T)$ for $PrNiO_3$ with that for Fe_3O_4 where, below the Verwey transition T_v, a phonon contribution is introduced rather than further suppressed as in $PrNiO_3$ below T_t. Suppression of the phonon component of $\kappa(T)$ in the crossover region reflects bond-length fluctuations associated with the coexistence of two fluctuating phases. Figure 23 also shows a suppression of $\kappa(T)$ above T_N in the insulators $SmNiO_3$ and $EuNiO_3$. The suppression of $\kappa(T)$ in the paramagnetic temperature range is due to spin–lattice interactions resulting primarily from the semicovalent-exchange component of the magnetic interactions [67].

Massa *et al* [105] and Mroginski *et al* [106] have reported evidence from reflectivity, transmission and photo-induced infrared spectra of strong electron coupling to Ni–O vibrational modes in the crossover $RNiO_3$ samples. A direct indication that T_t depends sensitively on the oxygen vibrational modes comes from the observation by Medarde *et al* [107] of a 10 °C increase in T_t on substitution of ^{18}O for ^{16}O, figure 24.

The phase diagram of the $RNiO_3$ family shown in figure 25 updates that of figure 19. The shaded area is the crossover region where the localized-electron and itinerant-electron phases coexist and compete on a nearly equal basis. The oxygen isotope coefficient $\alpha_o \equiv \mathrm{d}\log T_t/\mathrm{d}\log M_o$ (M_o is the oxygen mass) increases and the lattice contribution to $\kappa(T)$ decreases as the tolerance factor t increases across a narrow transitional range $\Delta t \approx 0.02$. Such a dramatic change in electronic properties with only a small change in the $(180° - \phi)$ bending

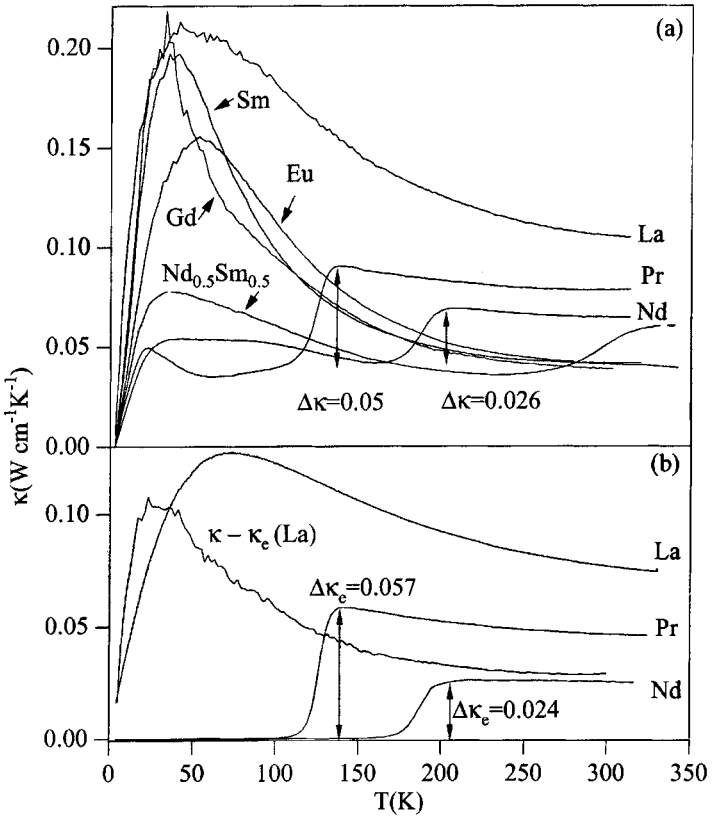

Figure 22. (a) Temperature dependence of the thermal conductivity in several cold-pressed $LnNiO_3$ samples (the Ln is labelled on each curve). (b) The upper-bound electronic contribution to the thermal conductivity in cold-pressed $LnNiO_3$ (Ln = La, Pr and Nd) calculated from $\rho(T)$ via the Wiedemann–Franz law, after [101].

angle forces consideration of the proper description of the dependence of the bandwidth W on ϕ.

Given the evidence for two-phase fluctuations associated with a strong electron coupling to oxygen vibrations, equation (18) provides a plausible expression for the bandwidth provided W_b includes narrowing due to a mass enhancement arising from the on-site Coulomb energy U. A $W = W_b \exp(-\lambda\varepsilon_{sc}/\hbar\omega_o)$ includes an oxygen-vibration frequency ω_o that decreases with the bending angle ϕ. Since it appears in an exponential term, the bandwidth W becomes sensitive to ϕ and therefore to the tolerance factor.

In order to distinguish between a $W = W_b$ and a $W = W_b \exp(-\lambda\varepsilon_{sc}/\hbar\omega_o)$, comparison was made between two samples of different composition each having the same value of T_t, one under pressure and the other at ambient [108]. Under pressure, the locally cooperative oxygen vibrations of frequency ω_o would increase with the reduction of the (Ni–O) bond length as well as with the reduction of the bending angle ϕ; W_b would also increase with an increase in the covalent-mixing parameter λ_σ, equations (7) and (8), as the mean (Ni–O) bond length and ϕ decrease. If the bandwidth were $W = W_b$, pressure would increase only t and samples with the same T_t would have similar properties. However, if $W = W_b \exp(-\lambda\varepsilon_{sc}/\hbar\omega_o)$, then stiffening of ω_o in the exponential would not only increase W more dramatically than the broadening of W_b, it would also influence other properties to give the two different compounds with the same T_t quite different properties even though T_t occurs at the same critical bandwidth W_c in each.

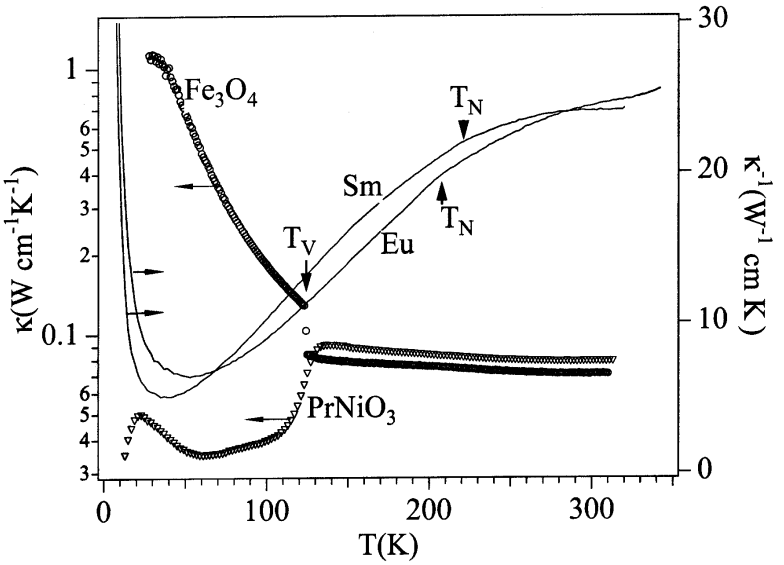

Figure 23. Temperature dependence of the thermal conductivity of single-crystal Fe_3O_4 together with that of cold-pressed $PrNiO_3$ and the inverse thermal conductivity of cold-pressed $SmNiO_3$ and $EuNiO_3$. The Verwey transition temperature T_V is shown on the Fe_3O_4 curve, after [101].

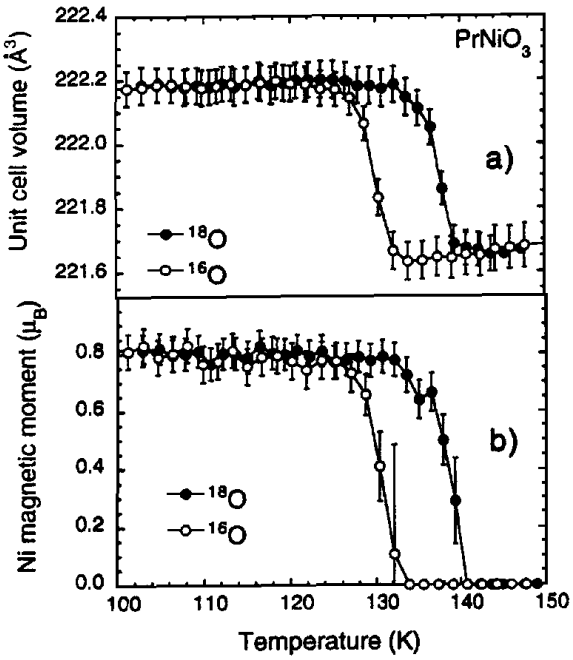

Figure 24. Unit-cell volume and Ni magnetic moment versus temperature for $PrNiO_3$ samples containing ^{18}O and ^{16}O, after [107].

Figure 26 compares the resistivity $\rho(T)$ and the thermoelectric power $\alpha(T)$ for three pairs of compounds, each pair with the same value of T_t [101]. Like $LaNiO_3$, $PrNiO_3$ at 14.9 kbar

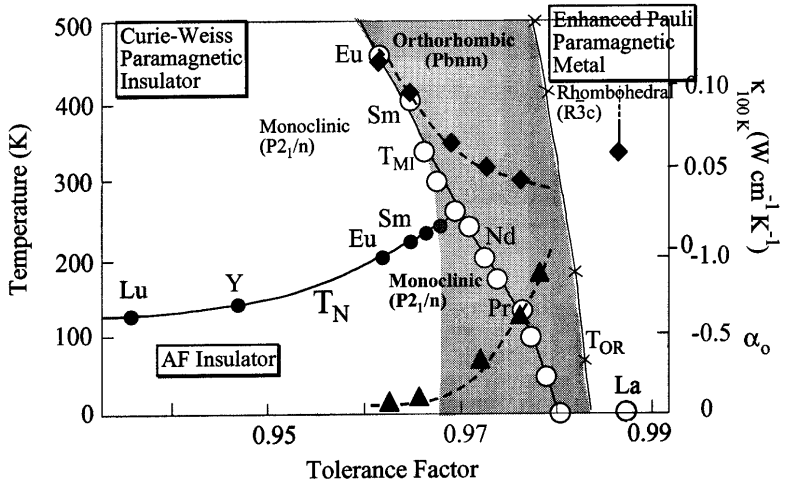

Figure 25. Phase diagram of the $RNiO_3$ family. The triangles symbolize the oxygen isotope coefficient α_o, the diamonds represent the lattice contribution to the thermal conductivity at 100 K, the circles are from figure 19 and T_{OR} is from [93], after [101].

remains metallic to lowest temperatures; however, there was no indication of an orthorhombic–rhombohedral transition below 15 kbar in $PrNiO_3$ and its $\rho(T)$ was significantly lower than that of $LaNiO_3$, figure 26(a), despite evidence from $\alpha(T)$ of a smaller density of charge carriers. Moreover, the transport properties of $PrNiO_3$ at ambient are quite different from those of $NdNiO_3$ under 13.2 kbar, figure 26(b). More striking is the difference between $NdNiO_3$ at ambient and $Sm_{0.5}Nd_{0.5}NiO_3$ under 15.7 kbar with the same value of T_t, figure 26(c). According to the phase diagram of figure 19, or as amended in figure 25, the interval $T_N < T < T_t$ in $Sm_{0.5}Nd_{0.5}NiO_3$ should vanish under a pressure that lowers T_t to that of $NdNiO_3$ if pressure only changes the tolerance factor t. Comparison of the $\alpha(T)$ curve at ambient in figure 20(d) with $\chi^{-1}(T)$ in figure 21(d) shows an increase in $\alpha(T)$ on cooling through $T_t > T_N$ that reaches a maximum value at T_N whereas cooling through a $T_t = T_N$ in $NdNiO_3$ gives a decrease in $\alpha(T)$. The sign of the change in $\alpha(T)$ on cooling through T_t of $Sm_{0.5}Nd_{0.5}NiO_3$ under 15.7 kbar remains opposite to that of $NdNiO_3$, and the interval $T_N < T < T_t$ as deduced from the maximum in $\alpha(T)$ does not change. This observation signals a $dT_N/dP < 0$ in contrast to the greater than normal $dT_N/dP > 0$ found for $SmNiO_3$. A change from $dT_N/dP > 0$ for localized spins coupled by superexchange interactions to a $dT_N/dP < 0$ for itinerant-electron antiferromagnets was predicted some years ago [108], and an early pressure experiment [109] on $CaCrO_3$ appeared to confirm that prediction.

In conclusion, the data of figure 26 show that pressure not only changes the tolerance factor t with $dt/dP > 0$ characteristic of a double-well potential for the equilibrium (Ni–O) bond length; it also changes the physical properties in a manner that favours a bandwidth $W = W_b(-\lambda\varepsilon_{sc}/\hbar\omega_o)$ over a $W = W_b$.

4.5. The mixed-valent manganese oxide perovskites

Thus far, the evidence cited for two-phase fluctuations at the crossover from localized- to itinerant-electronic behaviour has been restricted to single-valent compounds. In a p-type mixed-valent compound, the itinerant-electron phase would be electron poor and the localized-electron phase electron rich. This conclusion follows from the smaller magnitude

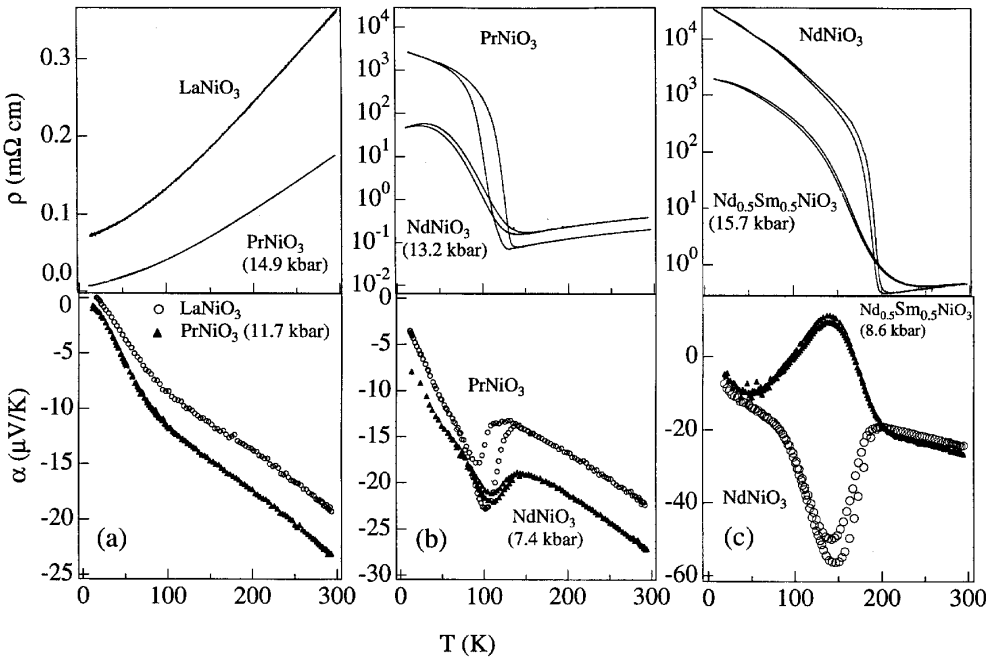

Figure 26. Comparisons of $\rho(T)$ and $\alpha(T)$ for two compounds with the same value of T_t, one at atmospheric pressure and the other under hydrostatic pressure, after [102].

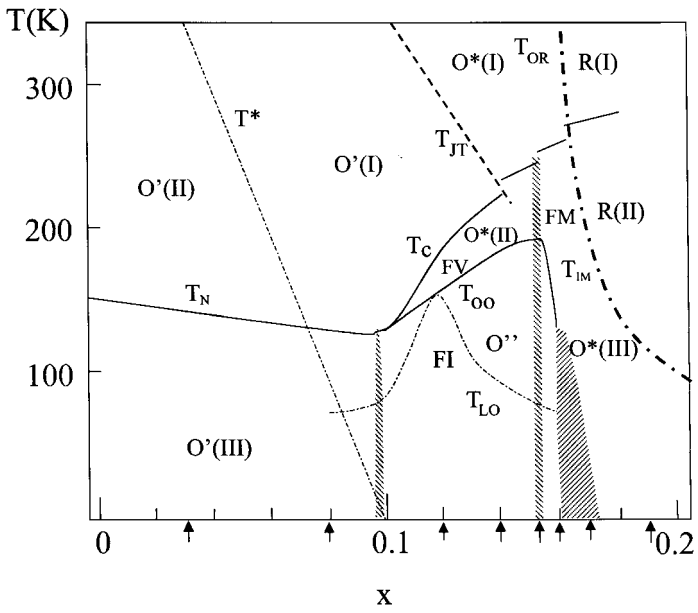

Figure 27. Phase diagram for $La_{1-x}Sr_xMnO_3$ in the crossover range $0 < x < 0.2$, after [80, 112].

$|\langle V\rangle|$ of the mean potential energy of the itinerant electrons as deduced from the virial theorem. In the $Ln_{1-x}A_xMnO_3$ (Ln = lanthanide, A = alkaline earth) manganese oxides with perovskite structure, for example, the itinerant-electron (or vibronic) clusters in a localized-

electron matrix are Mn(IV) rich and ferromagnetic; the Mn(III)-rich matrix is orbitally ordered O′-orthorhombic and therefore antiferromagnetic like the parent $LaMnO_3$ compound. Where the T_c of the orbitally disordered ferromagnetic phases is higher than the T_N of the matrix, an external magnetic field stabilizes the conductive ferromagnetic phase relative to the orbitally ordered, paramagnetic insulator matrix to give the colossal magnetoresistance (CMR) phenomenon where the ferromagnetic phase grows to beyond percolation within the paramagnetic matrix [110]. On cooling through the magnetic-ordering temperature, the internal Weiss molecular field grows the ferromagnetic phase to beyond percolation to give a ferromagnetic Curie temperature for a percolating, orbitally disordered vibronic phase containing an antiferromagnetic, orbitally ordered minority phase that may also become ferromagnetic and orbitally disordered, particularly in higher applied magnetic fields.

The phase diagram of figure 27 shows the crossover from a canted-spin antiferromagnetic insulator (CAFI) matrix to a ferromagnetic, metallic (FM) phase in the interval $0.08 < x < 0.2$ of $La_{1-x}Sr_xMnO_3$. A narrow, ferromagnetic vibronic (FV) phase in the temperature range $T_{oo} < T < T_c$ separates a paramagnetic (PM) matrix exhibiting the CMR phenomenon from a ferromagnetic-insulator (FI) phase. The PM matrix contains both ferromagnetic clusters and two-manganese polarons in an orbitally ordered O′-orthorhombic matrix; the two-manganese polarons condense progressively into the ferromagnetic clusters with decreasing temperature. The FI phase appears to have an orbital ordering that confines the itinerant electrons to c-axis 1D columns supporting a CDW [111]. At $x = 0.15$, there is a first-order transition from the FV compositions containing ferromagnetic vibronic superexchange and double-exchange interactions to a global FM phase [112].

4.6. Conclusion

In conclusion, the first-order character of the transition from localized to itinerant electronic behaviour has been demonstrated to be a general phenomenon that applies to mixed-valent as well as single-valent systems. In mixed-valent systems such as the copper oxides exhibiting high-temperature superconductivity, a first-order transition that gives rise to phase segregation at too low a temperature for atomic diffusion can, in perovskite-related structures, be accommodated by locally cooperative oxygen-atom displacements; these displacements can give either a spinodal phase segregation that supports two-phase fluctuations or QCP behaviour. A minority itinerant-electron phase in a localized-electron matrix exists, in a mixed-valent system, as a hole-rich itinerant-electron bag (cluster), i.e. as a multicentre polaron; where the volume fractions of the two phases compete equally with one another, the bond-length fluctuations are characteristic of those above a critical point and they give vibronic conduction. The QCP phase may represent a distinguishable thermodynamic state intermediate between a localized-electron phase and a FL phase. Ordering of the bond-length fluctuations may result in a static CDW; orbital ordering may confine itinerant electrons to a plane or an axis as in the manganese oxide perovskites. Given this picture of the character of the transition from localized-to itinerant-electronic behaviour in perovskite-related structures, we now apply it to an interpretation of the physical properties of the copper oxide superconductors.

5. Bond-length fluctuations in the copper oxide superconductors

5.1. Antibonding x^2–y^2 electrons

The structural architecture of the copper oxides removes the $(3z^2-r^2)$ and (x^2-y^2) degeneracy of the antibonding d-like states at the Cu atoms. In the parent compounds, the Cu(III) ions have filled $(3z^2 - r^2)$ orbitals and half-filled $(x^2 - y^2)$ orbitals strongly hybridized with O $2p_\sigma$

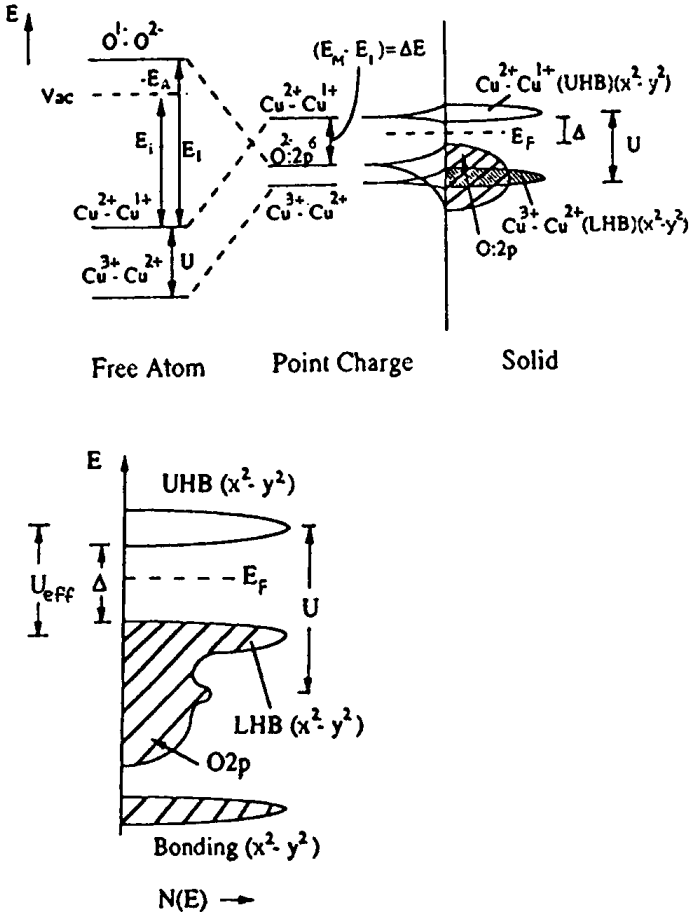

Figure 28. Schematic density of one-electron states for the CuO_2 sheets in Ln_2CuO_4 oxides where the lower $(x^2 - y^2)$ Hubbard band (LHB) is pinned at the top of the O 2p bands; the empty upper $(x^2 - y^2)$ Hubbard band (UHB) corresponds to the Cu(II)/Cu(I) couple, the filled LHB $(x^2 - y^2)$ to the Cu(III)/Cu(II) couple.

orbitals of a CuO_2 sheet. In a point-charge model, the Madelung energy is not strong enough to raise the Cu(III)/Cu(II) redox level above the O^{2-}:$2p^6$ level, so the Cu(III)/Cu(II) redox couple is pinned at the top of the O 2p bands and the $x^2 - y^2$ electrons have a strong O 2p admixture. Nevertheless, the parent compounds such as La_2CuO_4, which contain $(CuO_2)^{2-}$ sheets, are all antiferromagnetic insulators; a bandwidth $W < \Delta E_p < U$ means the on-site electron–electron Coulomb energy U is large enough to give localized spins and an energy gap $\Delta E_p = 1.5$–2.0 eV, figures 28 and 11.

Oxidation of the CuO_2 sheets of a parent compound does not create a localized Cu^{3+}:t^6e^2 configuration as found for isoelectronic octahedral-site Ni^{2+}:t^6e^2; the localized $(3z^2 - r^2)$ orbitals remain fully occupied on a Cu(III) atom, and oxidation introduces holes into the $(x^2 - y^2)$ band of antibonding states pinned at the top of the O 2p bands. The strong O 2p admixture in these $(x^2 - y^2)$ states would make these holes itinerant unless local oxygen displacements confined them to a molecular cluster. The smallest molecular cluster would be a single in-plane CuO_4 cluster having an empty $(x^2 - y^2)$ antibonding orbital. Such a cluster,

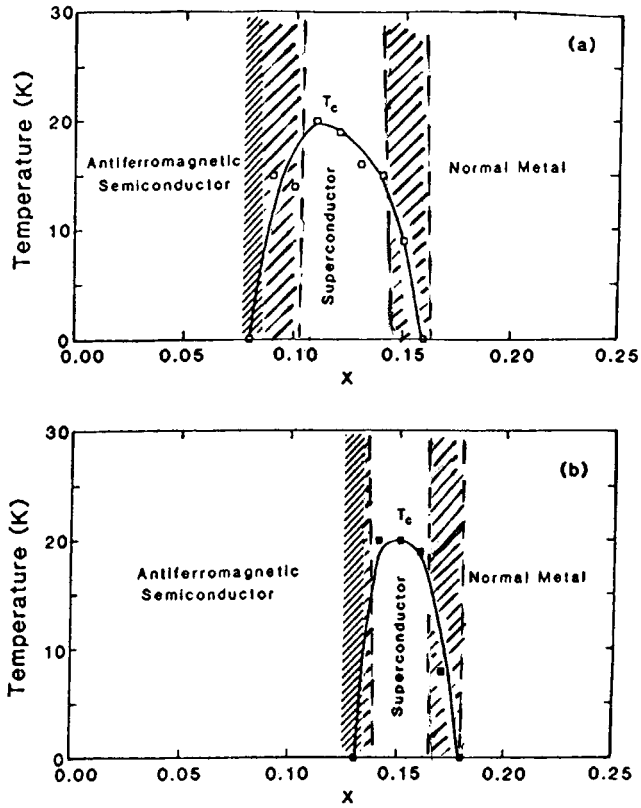

Figure 29. Variations of T_c with x for (a) $LaNd_{1-x}Ce_xCuO_4$ and (b) $Nd_{2-x}Ce_xCuO_4$. Shaded areas refer to two-phase regions, data from [115].

known as a Zhang–Rice singlet [113], has proved elusive. Alternatively, the hole may occupy a cluster containing several Cu centres; such a cluster would contain conductive $(x^2 - y^2)$ electrons and has, therefore, been referred to as a *correlation bag* since the $(x^2 - y^2)$ electrons within a bag are not localized, but occupy molecular orbitals [75]. The correlation bags are mobile with a motional enthalpy $\Delta H_m < kT_c$ [114].

The Cu atoms of the n-type superconductors have no apical oxygen atoms, which lowers the Madelung potential at a Cu site and raises the top of the O 2p band at which the occupied (x^2-y^2) states are pinned relative to the empty (x^2-y^2) states. The energy gap $\Delta E_p \approx 2.0$ eV in La_2CuO_4 is lowered to 1.5 eV in Pr_2CuO_4, and it decreases with increasing in-plane (Cu–O) bond length; see figure 11. Reduction introduces electrons into the upper antibonding $(x^2 - y^2)\sigma^*$ band, the Cu(II)/Cu(I) couple. The added electrons initially introduced form conventional small polarons ($\tau_h > \omega_o^{-1}$); but as the (Cu–O) bond length increases with deeper reduction, a critical lattice parameter is reached at which there is a first-order transition to a superconductive phase. Therefore, the smaller the mean ionic radius of the A cations, the larger is the critical concentration x_c at which the transition to superconductive behaviour occurs, see figure 29 [115]. The O 2p in the $(x^2 - y^2)\sigma^*$ band increases with the Cu–O bond length.

Both the p-type and the n-type overdoped samples are FL metals; in these mixed-valent compounds, the time for a charge carrier to hop from one site to another is $\tau_h < \omega_o^{-1}$ over the entire crystal. A $\tau_h < \omega_o^{-1}$ means the charge carriers are not confined by cooperative oxygen

displacements to a molecular cluster; they are itinerant. At the crossover from a $\tau_h < \omega_o^{-1}$ to a $\tau_h > \omega_o^{-1}$, a $\tau_h \approx \omega_o^{-1}$ gives bad-metal behaviour in which the charge carriers interact strongly with the lattice and with one another.

At higher temperatures, holes initially doped into the lower $(x^2 - y^2)$ band are self-trapped by cooperative atomic displacements in single-hole correlation bags containing several Cu centres; the positively charged bags move in a negatively charge electron-rich matrix, and Coulomb repulsions keep apart the individual bags. On lowering the temperature below a critical temperature T_s, a spinodal separation of the parent phase and a hole-rich phase occurs. Where there are mobile ions below T_s, the phase separation is accomplished by atomic diffusion; where there are no mobile ions, phase segregation can only occur by cooperative atomic displacements. In the hole-rich phase, the one-hole bags would overlap, so mobile multihole bags are formed and the mobile holes interact strongly with the cooperative (Cu–O) bond-length fluctuations that define the bags. The electronic behaviour of this phase is like that of a system above a critical point; therefore, it has been referred to as QCP behaviour [116–120] and the superconductive phase will be referred to as the QCP phase. Significantly, the phase separation in the underdoped compositions is not between the parent phase and a metallic phase, but between the parent phase and the unusual QCP phase.

Within the QCP phase, the instability associated with a double-well potential for the equilibrium (Cu–O) bond length is reflected in the coexistence of fluctuating, positively charged regions where a shorter average ⟨Cu–O⟩ bond length stabilizes weakly correlated electrons and negatively charged regions where a longer ⟨Cu–O⟩ bond length stabilizes localized spins. The volume fraction of the localized spins decreases as the hole concentration increases. The QCP phase is a bad metal and remains p-type, which shows retention of the splitting ΔE_p between lower and upper $(x^2 - y^2)$ bands. Where the crystallographic structure is retained to high enough hole concentrations, an n-type metallic, FL phase is reached; the transition from the QCP vibronic phase to the FL phase is first order, so another fluctuating two-phase region is encountered on the overdoped side as has also been noted by Phillips [120a, b].

On cooling the QCP phase, ordering of the bond-length fluctuations selects, at lowest temperatures, a specific concentration of the charge carriers. In the underdoped samples, this selection increases the volume fraction of the parent phase. However, different orderings of the bond-length fluctuations may compete with one another where the hole fraction p corresponds to a critical concentration for a commensurate CDW as occurs at $p = 1/8$, for example. The superconductive state and any competing commensurate-CDW state represent distinguishable low-temperature thermodynamic phases.

In the n-type materials, the electrons initially introduced are trapped at single sites as small polarons, and the intermediate QCP phase is confined to a narrow compositional range.

It is instructive to distinguish the lattice instabilities that occur in a single-valent compound at the crossover from localized to itinerant electronic behaviour from those that occur in a mixed-valent compound. In the single-valent compounds $CaFeO_3$ and $YNiO_3$, for example, the segregation into molecular-orbital clusters and localized-electron configurations requires a disproportionation reaction resulting in a 'negative-U' CDW. In the mixed-valent CuO_2 sheets of the copper oxides, segregation into electron-rich and electron-poor regions does not require a disproportionation stabilized only by the CDW ordering; it already occurs as a result of cooperative bond-length fluctuations at higher temperatures. Formation of a CDW at lower temperatures would be the result of an ordering of the mobile, short-length-scale regions of different charge resulting from the cooperative oxygen-atom displacements. However, a conventional CDW changes the translational symmetry of a crystal so as to open up a gap in the density of one-electron states at the Fermi surface, thus competing with the opening of a gap at the Fermi energy by the formation of superconductive Cooper pairs. The key to

understanding the high-T_c phenomenon in the copper oxides is to determine how the ordering of the bond-length fluctuations stabilizes a superconductive energy gap over a gap imposed by a change in the translational symmetry of the periodic potential.

5.2. $La_2CuO_{4+\delta}(0 \leqslant \delta \leqslant 0.1)$

The system $La_2CuO_{4+\delta}$ is instructive because it undergoes a conventional phase segregation by atomic diffusion between the parent antiferromagnetic phase of figure 2 and a composition that exhibits QCP behaviour.

As early as 1987, filamentary superconductivity was observed in ceramic samples of nominal La_2CuO_4 that had been slow cooled in air from the sintering temperature [43, 45]. This procedure loads the structure with excess oxygen to yield $La_2CuO_{4+\delta}$ with a maximum $\delta \approx 0.02$. Slow cooling in O_2 atmosphere raises the oxygen loading to $\delta \approx 0.03$.

In order to explore this phenomenon further, samples were loaded to higher values of δ with high oxygen pressures [44–46], and a phase segregation into an oxygen-rich superconductive phase and an oxygen-poor antiferromagnetic phase was shown to occur below a temperature T_s [47]. Neutron-diffraction studies [47, 49, 121] performed on $\delta \approx 0.03$ samples gave a range 290 K $\leqslant T_s \leqslant$ 320 K for the onset temperature of phase segregation and a $T_t \approx 430$ K for the orthorhombic–tetragonal transition in the single-phase region above T_s, figure 30. The oxygen-poor phase was the parent La_2CuO_4 compound; with decreasing temperature, its volume fraction increased as did the oxygen concentration δ_s of the phase exhibiting QCP behaviour that, at lower temperatures, became superconductive. The phase separation occurs via a diffusion of the interstitial oxygen located between two rock-salt LaO sheets (see section 2.2), and suprisingly these interstitial oxygens remain mobile down to about 200 K [49, 122]. Ahrens *et al* [123] have used magnetic susceptibility and La nuclear quadrupole resonance (NQR) to probe the phase segregation in a $\delta \approx 0.032$ sample. They found that T_c increases with the size of the segregated superconductive filaments where the filament diameter is comparable to a magnetic penetration depth. In a spinodal phase segregation, the cross-section of a percolating phase may be small; and the ordered, superconductive volume would be reduced by further phase segregation as the bond-length fluctuations order to select a superconductive carrier concentration corresponding to optimal doping. As the volume fraction of the percolating superconductive phase increases, suppression of T_c by the magnetic penetration depth decreases.

Oxygen loadings to $\delta = 0.10$ were obtained electrochemically by Wattiaux *et al* [124], and transport properties were measured over the entire compositional range $0 \leqslant \delta \leqslant 0.10$ [48, 125]. Zhou *et al* [48] determined the temperature and compositional range of the phase separation by monitoring the temperature dependences of the resistivity $\rho(T)$ and thermoelectric power $\alpha(T)$ under different pressures and thermal histories. They found that phase separation occurs between the antiferromagnetic parent phase with $\delta \approx 0$ and a superconductive phase with $\delta_s(\max) \approx 0.05$. The Néel temperature of the limiting composition of the parent phase was reduced from 320 to about 250 K. The temperature T_s for onset of the phase segregation decreased with increasing δ with a curvature concave to the δ axis to just below 200 K where the interstitial oxygen becomes immobile. An ordering of the interstitial oxygen occurs above room temperature in the compositional range $0.066 < \delta_o < 0.70$. A $\delta_o > \delta_s(\max)$ shows that the driving force for the phase segregation in the range $0 < \delta \leqslant 0.05$ is not stabilization of a phase with ordered interstitial oxygen; the driving force is not structural, but of electronic or vibronic origin. The normal electronic state of the superconductive phase is thus seen to be thermodynamically distinguishable from that of the antiferromagnetic parent phase. A $T_s \leqslant T_N$ $(x = 0)$ signals that the spin–spin interactions play a dominating role in driving

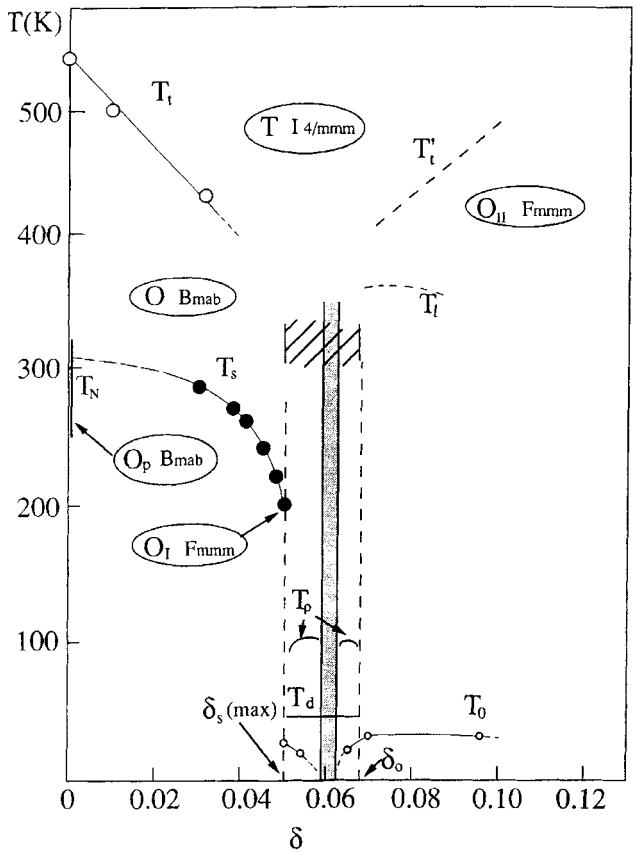

Figure 30. Phase diagram for $La_2CuO_{4+\delta}$, after [48].

segregation of the antiferromagnetic phase from the hole-rich superconductive phase having a hole concentration per Cu atom $p > 2\delta_s(\max) = 0.10$. However, this electronically driven static phase separation is to be distinguished from the lattice instabilities that give rise to the bond-length fluctuations that characterize the QCP behaviour of the superconductive phase.

Zero-field muon-spin relaxation (ZF-μSR) measurements on a $La_2CuO_{4.11}$ single crystal have been used to determine that the magnetically ordered phase forms as islands in the CuO_2 planes having a radius $R = 15$–30 Å with a weak coupling between islands; the volume fraction of the magnetically ordered phase increased to 40% as the temperature was lowered [126]. An applied magnetic field increases this volume fraction [127].

A competitive, non-superconductive phase was found [125] in the narrow compositional range $0.054 < \delta < 0.66$, which spans $p = 1/8$; it separates superconductive compositions appearing at smaller and larger values of δ. The hole concentration $p = 1/8$ is able to stabilize a commensurate CDW that tends to compete with the opening of a superconductive gap as is discussed below. The important point to be made here is that the extraordinary mobility of the interstitial oxygen in $La_2CuO_{4+\delta}$ allows a conventional phase segregation to be observed setting in near or below room temperature. In the absence of atomic diffusion, the driving force for phase segregation must be accommodated by electron–lattice interactions that do not allow establishing local charge neutrality in electron-rich and electron-poor phases. This latter

constraint imposes confinement of the separated phases to a small length scale and allows the phase boundaries to fluctuate. Nevertheless, a distinction must be made between this phase segregation, which is driven largely by the strong interatomic exchange interactions between localized spins in the parent phase, and the lattice instabilities associated with a double-well (Cu–O) potential that are responsible for QCP behaviour in the superconductive compositions.

Abbamonte *et al* [128] have recently magnified 82 times the charge-carrier contribution to the amplitude of the anomalous x-ray scattering of the oxygen K edge of an optimally doped $La_2CuO_{4+\delta}$ film. They used the technique, which has a spatial resolution of 1.1 nm, to search for evidence of hole ordering within the CuO_2 sheets at 50 K $> T_c$. They were unable to detect any in-plane carrier modulation in their material that would signal an ordering of the holes into Cu–O–Cu axes (metallic stripes) in a travelling CDW.

5.3. Other p-type superconductors

The system $La_{2-x}Sr_xCuO_4$, $0 \leqslant x \leqslant 0.3$, is the simplest p-type system; it has no charge-reservoir layer between the rock-salt LaO sheets and therefore the fraction of holes in the CuO_2 sheets is given unambiguously by $p = x$ provided the oxygen stoichiometry is maintained. Also, $La_{2-x}Sr_xCuO_4$ has the same parent compound, figure 2, as $La_2CuO_{4+\delta}$. Moreover, it spans the entire compositional range of interest from the parent compound at $x = 0$ to the overdoped, metallic regime at $x \geqslant 0.27$. In addition, stoichiometric single crystals can be grown by the floating zone method in an infrared image furnace. It has, therefore, been extensively and intensively studied in a search for the origin of the high-T_c phenomenon in the copper oxides. The $Bi_2Sr_2Ca_nCu_{n+1}O_{6+2n}$ family cleaves easily, exposing a chemically inert surface, so these superconductors have been studied with surface-sensitive techniques such as photoelectron spectroscopy. The information about the properties of the CuO_2 sheets in this family is transferable to the CuO_2 sheets of other systems. $YBa_2Cu_3O_{7-\delta}$ with $\delta \approx 0.09$ is optimally doped, gives a $T_c \approx 90$ K and has a relatively strong c-axis coupling between CuO_2 sheets because the chains of the conductive $\Phi = CuO_x$ charge-reservoir layer also become superconductive below T_c. Therefore, $YBa_2Cu_3O_{7-\delta}$ has been most extensively studied for technical applications and for determining the behaviour of the vortices of the strongly type II superconductor as a function of temperature and applied field, topics not covered in this article.

A tentative phase diagram for the system $La_{2-x}Sr_xCuO_4$ is shown in figure 31. A complete solid solution for $0 \leqslant x \leqslant 0.3$ exists above about 325 K. The Néel temperature $T_N \approx 320$ K of the parent phase is seen to drop sharply with increasing x, long-range antiferromagnetic order being replaced by antiferromagnetic spin clusters by $x \approx 0.02$ [129]. The Cu–O–Cu interactions within a CuO_2 sheet are much stronger than the Cu–O–O–Cu interactions between sheets, so considerable short-range magnetic order within a sheet is present below a temperature $T_{max} > T_N$, where T_{max} is the temperature at which the magnetic susceptibility shows a broad maximum. In two-dimensional (2D) systems, long-range magnetic order below T_N commonly occurs at a significantly lower temperature than T_{max}. The decrease in T_{max} with increasing x in figure 31 is less precipitous than the decrease in T_N, falling to T_c near $x = 0.23$ [130]. Any 2D short-range magnetic order of localized spins in the CuO_2 sheets has collapsed in compositions with $x > 0.23$.

Substitution of a large Sr^{2+} ion for La^{3+} and its oxidation of the CuO_2 sheets makes the 2D tolerance factor t_{2D} increase with x. Consequently, the orthorhombic (O) to high-temperature tetragonal (HTT) structural transition at T_t, figures 2(a), (b), decreases with increasing x from $T_t \approx 430$ K in the parent phase to cross the superconductive critical temperature T_c at $x \approx 0.21$ [131, 132]. Hydrostatic pressure stabilizes the tetragonal phase, demonstrating by a $dt_{2D}/dP > 0$ that the (Cu–O) bond length is abnormally compressible and therefore

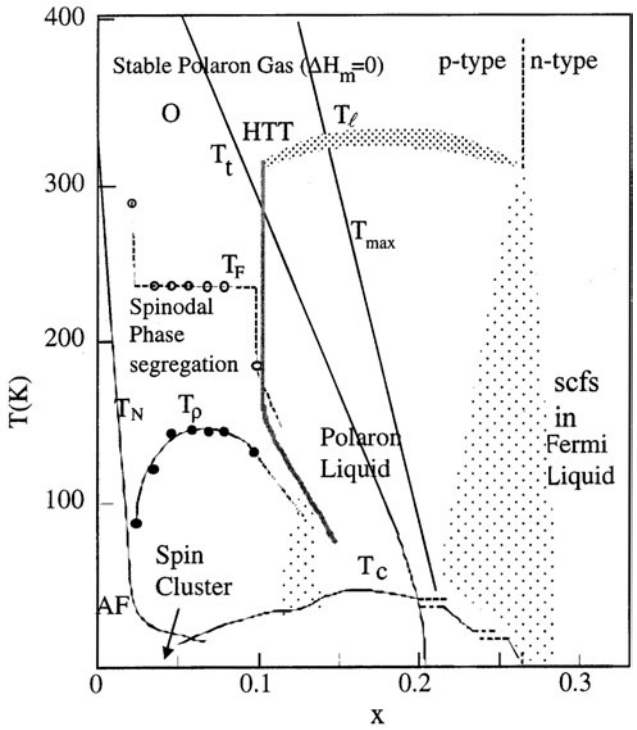

Figure 31. Phase diagram for the system $La_{2-x}Sr_xCuO_4$, adapted from [110].

the presence of a double-well potential for the equilibrium (Cu–O) bond length in the CuO_2 sheets [132].

The variation of T_c with the fraction p of mobile holes per Cu atom has been found to be similar for all the underdoped p-type superconductors. Uemura *et al* [133] used muon-spin rotation to establish the relation

$$T_c \sim p/m* \qquad \text{for } p < 0.15 \tag{23}$$

where m^* is the mean effective mass of the charge carriers. From empirical evidence for several systems, Presland *et al* [134] have proposed that a general parabolic law

$$T_c/T_{c,\max} = 1 - 82.6(p - 0.16)^2 \tag{24}$$

applies to all the p-type superconductors. In the system $La_{2-x}Sr_xCuO_4$, where $p = x$, T_c saturates in the range $0.15 \leqslant p \leqslant 0.18$ and the general trends of equations (23) and (24) are altered by some suppression of T_c in the neighbourhood of $p = 1/8$ [135]. In addition, a careful study of the overdoped region [132] has provided evidence, figure 32, that the transition from the optimally doped superconductive phase to the overdoped phase may encounter one or more competitive phases.

The value of $T_{c,\max}$, and therefore of T_c for a given value of p, depends on (1) the Cu–O–Cu bond angle, (2) the Cu–O bond length and (3) the variance of the A-site cation. In the system $La_{2-x}Sr_xCuO_4$, there is no charge reservoir, so $p = x$ remains fixed under pressure. The A-site-cation variance is also fixed. Samples with $x < x_c$ under hydrostatic pressure had a $dT_c/dP \approx 0.1$ K kbar^{-1} in the orthorhombic phase that dropped abruptly to $dT_c/dP \approx 0$ on crossing the critical value of $x = x_c$ for the orthorhombic to tetragonal phase change at

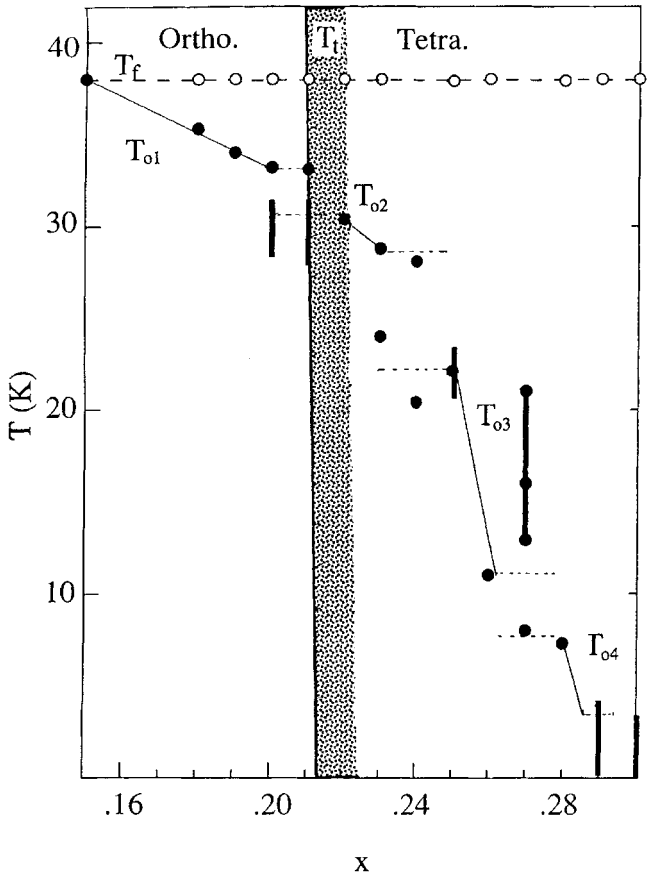

Figure 32. Compositional dependence of T_f and the superconductive onset temperature T_o indicative of a possible sequence of competitive phases, taken from data given in [132].

$P > 10$ kbar, figure 33 [132]. In the tetragonal structure, the Cu–O–Cu bond angle is 180° and pressure changes only the (Cu–O) bond length. In the orthorhombic structure, pressure reduces both the Cu–O bond length and the bending angle ϕ. Therefore, figure 33 teaches that $T_{c,\max}$ is insensitive to a decrease of a (Cu–O) bond length already under a compressive stress, but it increases sensitively with a straightening of the Cu–O–Cu bond angle.

In order to demonstrate that this conclusion also applies to a nearly optimally doped sample, $x = 0.15$, advantage was taken of the 2D compressive stress on the (001) plane of a thin film deposited epitaxially on a substrate of smaller lattice parameter [136]. Sato and Naito [137] had demonstrated that $La_{2-x}Sr_xCuO_4$ epitaxial films with c-axis oriented perpendicular to the substrate have T_c reduced by the 2D tensile stress on the CuO_2 sheets deposited on $SrTiO_3$ and increased by the 2D compressive stress on the CuO_2 sheets deposited on $LaSrAlO_4$. A single-crystal $La_{1.85}Sr_{0.15}CuO_4$ film on $LaSrAlO_4$ remained orthorhombic at the superconductive onset temperature T_o, but it had a $T_c = 43$ K compared to a $T_c \approx 36$ K in an unstressed ceramic or single-crystal sample. The T_c of the film increased with pressure for $P \leqslant 4$ kbar, saturating at 43.7 K for $P > 4$ kbar.

On the other hand, the $HgBa_2Ca_{n-1}Cu_nO_{2n+2+\delta}$ compounds have 180° Cu–O–Cu bonds that are under tension, and hydrostatic pressure increases T_c dramatically until T_c reaches a

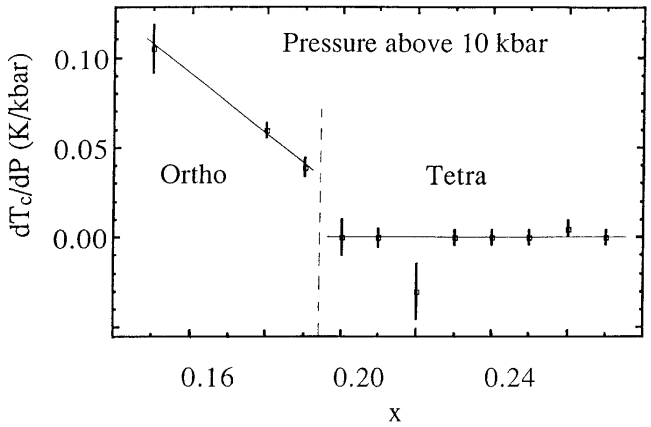

Figure 33. Variation with x of the pressure dependence of T_c for $P > 10$ kbar in the system $La_{2-x}Sr_xCuO_4$, after [132].

broad maximum above 8 GPa [138–140]. In the $n = 3$ compound, a $T_{c,\max} \approx 164$ K was reached at 31 GPa. Under pressure, transfer of charge from the CuO_2 sheets appears to be minimal. Although some charge transfer between the two outer CuO_2 sheets and the inner CuO_2 plane may contribute to dT_c/dP in the $n = 3$ compound, no such charge transfer is possible in the single-layer ($n = 1$) and double-layer ($n = 2$) compounds. These results appear to teach that where the (Cu–O) bonds of a CuO_2 sheet are stretched, reduction of the (Cu–O) bond length toward its equilibrium value enhances T_c, which contrasts with the small influence on T_c of reduction of the length of a Cu–O bond under a compressive stress.

The transport properties of the system $La_{2-x}Sr_xCuO_4$ divide the phase diagram of figure 31 at compositions near $x = 0.10$ and 0.22 [35, 132, 141]. In the compositional range $0 < x \leqslant 0.10$, the resistivity varies nearly as $\rho - \rho_i \sim T$ in the range $T_\rho < T < T_l$. Above T_l, the ρ versus T curve bends toward the temperature axis, i.e. $d\rho/dT$ decreases with increasing T, and below T_ρ the resistivity increases with decreasing temperature, figure 34; the resistance drops precipitously to zero below the superconductive critical temperature $T_c < T_\rho$ in the range $0.05 \leqslant x \leqslant 0.10$. In the range $0.10 < x < 0.22$, a $(\rho - \rho_i) \sim T$ is found for all temperatures $T > T_c$ below the decomposition temperature of the solid. In the compositional range $x > 0.22$, the critical temperature T_c drops with increasing x, falling to zero by $x \approx 0.27$, and above T_c the $\rho(T)$ curves exhibit a power-law behaviour. All the superconductive compositions show a small step in the $\rho(T)$ curve at a temperature $T_f \approx T_c(\max)$. The independence of T_f on doping is remarkable and seems to imply that the composition with $T_c(\max)$ represents a particular ordering of the (Cu–O) bond-length fluctuations for the superconductive state and that regions without this order induce phase fluctuations that suppress T_c.

The temperature dependence of the square of the thermoelectric power, $\alpha^2(T)$, shows a remarkable change not only on passing from $x \leqslant 0.10$ to $x \geqslant 0.15$, but also on passing from $T < T_l$ to $T > T_l \approx 320$ K, figures 34 to 36. At temperatures $T > T_l$, there is a smooth evolution with x of the $\rho(T)$ and $\alpha(T)$ curves. In the compositional range $0 \leqslant x \leqslant 0.10$, a temperature-independent thermoelectric power extends from high temperature down to $T_F < T_l$; $\alpha^2(T)$ drops with decreasing temperature $T < T_F$ and falls linearly in the range $T_c < T < T_\rho$ where $\rho(T)$ deviates from a linear dependence on T. In contrast, a nearly constant $\alpha(T)$ above T_l in the range $0.10 \leqslant x \leqslant 0.25$ undergoes a remarkable enhancement below T_l that reaches a maximum near 140 K, which is too high a temperature for a phonon-

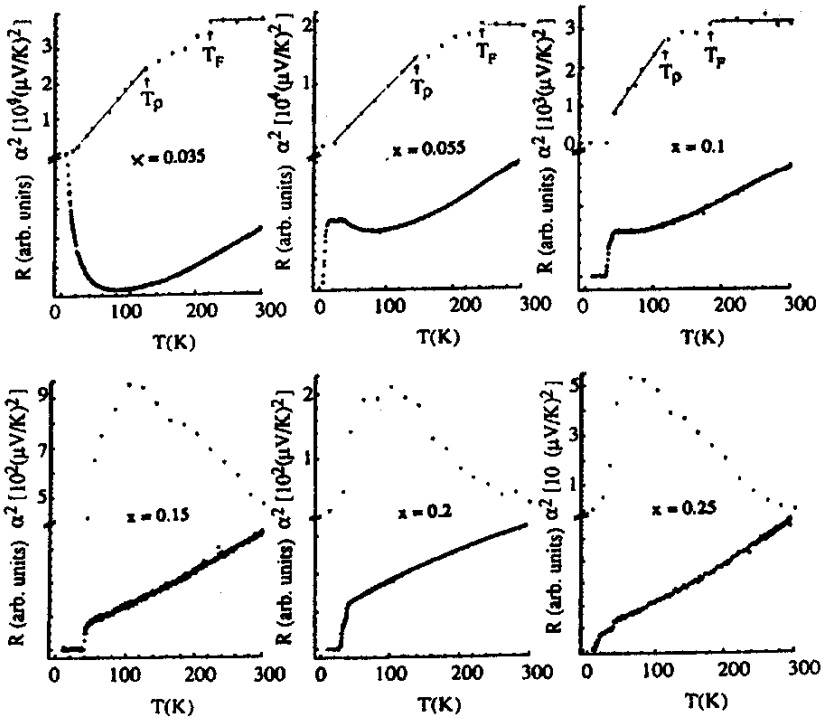

Figure 34. Temperature dependence of the square of the thermoelectric power, α^2, and the resistance R for several values of x in the system $La_{2-x}Sr_xCuO_4$, after [35].

drag enhancement. This enhancement has been shown [142–144] to be a characteristic of the QCP phase, appearing in the normal state of all the copper oxide superconductors in the compositional range of the QCP phase, and only in connection with this phase, which retains a fraction of the volume in the overdoped compositions where T_c falls to zero.

Interpretation of the electronic behaviour of the underdoped range $0 < x < 0.15$ begins with the observation that a temperature-independent thermoelectric power $\alpha(T)$ signals polaronic conduction with a resistivity

$$\rho = AT \exp(\Delta H_m/kT) \tag{25}$$

for a fixed charge-carrier fraction p per Cu atom having a motional enthalpy ΔH_m in the diffusive mobility

$$\mu = (eD_o/kT) \exp(-\Delta H_m/kT). \tag{26}$$

Where the conduction is polaronic, the thermoelectric power is dominated by the statistical component

$$\alpha = (k/e) \ln[\beta(1-c)/c] \tag{27}$$

where $\beta = 2$ is the spin-degeneracy factor and the fractional hole occupancy of sites available to a single-hole polaron is $c = pN/N^* = pn$ for N Cu atoms and n Cu centres inside the polaron [145]. Figure 35 shows that the room-temperature data fit equation (27) in the range $0 < x \leqslant 0.1$ if $N/N^* = 5.3$. We may conclude that in this compositional range at temperatures $T > T_F$, the holes are not small polarons, but occupy single-hole correlation bags, extending over five to six Cu centres. Within the bags the electrons occupy molecular

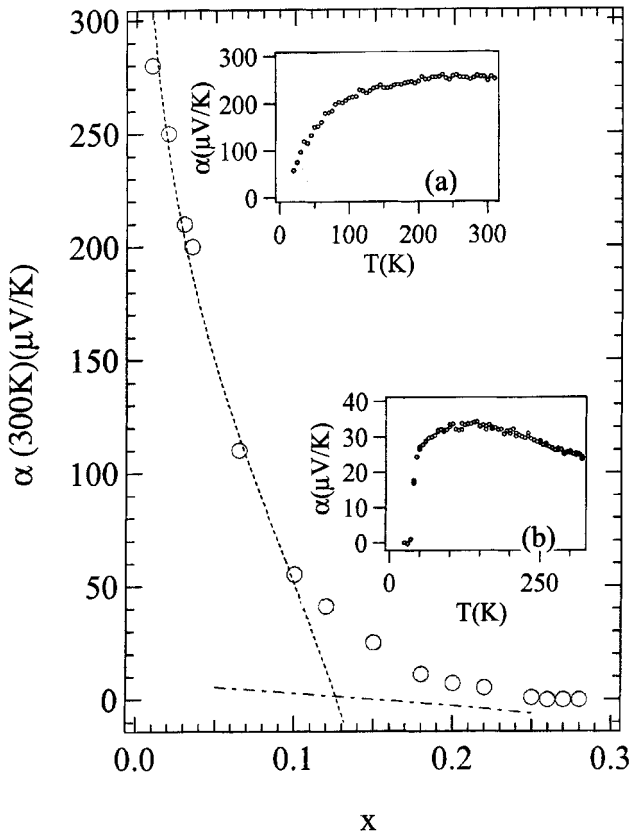

Figure 35. Room-temperature thermoelectric power α (300 K) for $La_{2-x}Sr_xCuO_4$. Dashed curve = fit to logarithmic plot with $N/N^* = 5.3$. Dot and dash line = result of band calculation. Insets (a) and (b) are $\alpha(T)$ for $x = 0.02$ and 0.15, respectively, after [141].

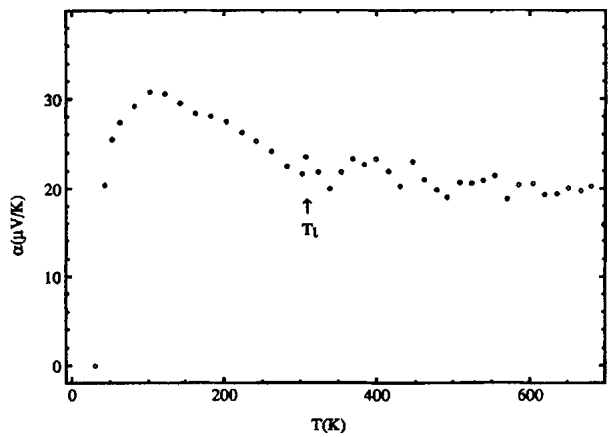

Figure 36. Temperature dependence of the thermoelectric power $\alpha(T)$ for $La_{1.85}Sr_{0.15}CuO_4$ showing a transition at $T_l \approx 320$ K, after [35].

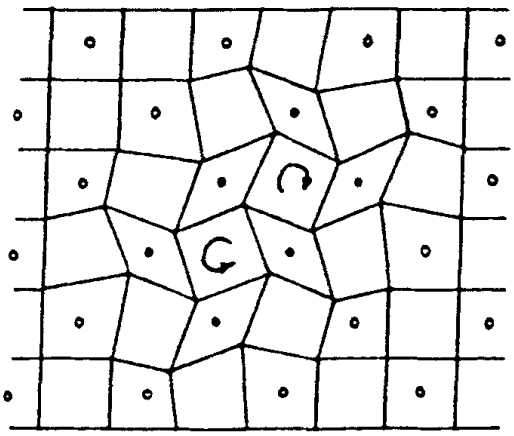

Figure 37. Model of a one-hole correlation bag stabilized over six Cu centres by cooperative pseudo-Jahn–Teller deformations, after [114].

orbitals, so a five-copper bag would have no spin. Why the correlation bags do not collapse to a small-polaron Zhang–Rice singlet remains an open question. However, a low-spin Cu(III) ion in a site with tetragonal symmetry may undergo a pseudo-Jahn–Teller distortion of the square oxygen coordination in a CuO_2 sheet to rhombohedral (Cu–O) bonding [146]. Therefore, one possibility, in addition to a lowering of the kinetic energy of the cluster electrons, is a gain in elastic energy associated with cooperative pseudo-Jahn–Teller distortions of several Cu centres from square to rhomboidal Cu–O bonding within the polarons as illustrated in figure 37. A model calculation [114, 147] for such a bag gave a stable polaron size of six to seven copper centres and an amoeba-like motion of the polaron that reduced the motional enthalpy ΔH_m to a small value ($\Delta H_m < kT_\rho$). The calculation reproduced the shape of the normal-state resistance $R(T)$ of figure 34 as well as rationalizing the size of the one-hole polaron. The upturn in $R(T)$ on cooling below T_ρ is caused by the small ΔH_m of the multicentre polarons. Significantly, a 61 T pulsed magnetic field suppressed superconductivity in an $x = 0.16$ sample to reveal an $R(T)$ curve like that of figure 34 for the non-superconductive $x = 0.035$ sample [148]. Suppression of the superconductivity of an optimally doped sample by a high magnetic field $H > H_{c2}$ reveals that the charge carriers of the normal state have a small motional enthalpy $\Delta H_m < kT_c$ in a large H field. At higher temperatures $kT \gg \Delta H_m$, the bag mobility approaches the limit $\mu = (eD_o/kT)$ to give bad-metal behaviour with $(\rho - \rho_i) \sim T$. In the underdoped region, the change in slope of the $\rho(T)$ curve reflects the opening of a pseudogap below $T^* \approx T_\rho$; the charge transport in the CuO_2 planes is largely unaffected by the opening of the pseudogap [149] whereas the transport of charge along the c-axis is strongly suppressed [150, 151].

The precipitous drop in the Néel temperature T_N reflects a spinodal phase segregation occurring below $T_F = T_s$ between the parent phase and the QCP phase stabilized at $x > 0.1$. In the system $La_2CuO_{4+\delta}$, this phase segregation sets in at a somewhat higher temperature where the mobile interstitial oxygen atoms allow segregation of oxygen-rich and oxygen-poor phases that preserve local charge neutrality. In $La_{2-x}Sr_xCuO_4$, there are no mobile ions, and the spinodal phase segregation can only be accomplished by cooperative oxygen-atom displacements that segregate hole-rich and hole-poor regions. The one-hole correlation bags already represent a segregated hole-rich phase of smaller mean ⟨Cu–O⟩ bond length; but their size is such that by $x = 0.1$ they are forced to overlap and condense into multihole bags. The

QCP phase is characterized by locally cooperative bond-length fluctuations that would define multihole bags and localized-electron regions, but they can only achieve short-range order on cooling below T_l with both spin and spinless-bag fluctuations. However, the order increases with decreasing temperature with long range being established either with formation of a CDW or a superconductive state. The Coulomb forces between the negatively charged parent phase and the positively charged QCP phase in the interval $0 < x \leqslant 0.1$ segregate the parent phase to a length scale that decreases sharply with increasing x until, for $x > 0.02$, the antiferromagnetic phase is confined to non-percolating clusters [152]. Cho *et al* [153] have argued convincingly for the existence of quasistatic fluctuations of mesoscopic antiferromagnetic domains in the range $0.02 \leqslant x \leqslant 0.08$. Julien *et al* [154] have studied an $x = 0.06$ sample with ^{63}Cu and ^{139}La NMR/NQR to show that, on cooling, the CuO_2 sheets separate progressively into two phases, one of them having enhanced antiferromagnetic correlations in clusters and the other giving rise to superconductivity below $T_c = 8$ K. Neutron scattering studies [155, 156] have identified a spin-glass phase in the range $0.02 \leqslant x \leqslant 0.055$ that has a spin-freezing temperature near 28 K and a spin modulation propagating diagonal to the Cu–O–Cu rows of a CuO_2 sheet. Phase segregation between the parent phase and this incommensurate antiferromagnetic phase occurs in the range $0 \leqslant x \leqslant 0.02$ [157] and the propagation vector of the spin-density wave changes to parallel to the Cu–O–Cu rows [158]; the appearance of superconductivity correlates with the existence of a percolating QCP phase with spin modulations parallel to the Cu–O–Cu rows.

In the QCP phase, there is a transition with increasing x in the temperature interval $T_c < T < T_l$ from fluctuating multihole bags in a localized-electron matrix in the underdoped compositions to strong-correlation fluctuations in an FL in the overdoped samples. Bozin *et al* [159] have used pair-density-function (PDF) analysis of pulsed neutron data, which is a fast experimental probe, to demonstrate the coexistence of two different equilibrium (Cu–O) bond lengths in the QCP phase, one corresponding to that of the antiferromagnetic parent phase and the other to that of the overdoped phase with $(Cu–O)_{itin}$. This experiment provides direct evidence that cooperative oxygen-atom displacements create fluctuating clusters in which the mean (Cu–O) bond length is either the $(Cu–O)_{loc}$ for localized electrons or $(Cu–O)_{itin}$ for correlation bags or an FL matrix.

On cooling, the localized-electron and itinerant-electron regions order progressively, but ordering into a commensurate CDW may compete with ordering of the superconductive state. Near the composition $x = p = 1/8$, the competitive commensurate-CDW phase consists of itinerant-electron stripes in every fourth Cu–O–Cu row, figure 38; this CDW opens up a gap at the Fermi surface to suppress superconductivity. It is stabilized relative to the superconductive phase by a structural change from orthorhombic to low-temperature tetragonal (LTT) symmetry. In the LTT phase, the oxygen atoms coordinating a Cu change their cooperative-rotation axis from the [110] of the orthorhombic phase to [100] and [010] in alternate CuO_2 sheets [160, 161], which orders and pins the holes in static stripes oriented along a rotation axis. This LTT phase is found in the system $La_{1-y-x}Nd_ySr_xCuO_4$; at $y = 0.6$ and $x = 1/8$, static itinerant electron stripes are pinned every fourth row, which has allowed identification of the phase with neutron diffraction by Tranquada *et al* [162, 163]. The metallic, positively charged stripes have a hole concentration per Cu atom of $p = 0.5$, whereas the negatively charged, localized-electron rows between the stripes have $p \approx 0$ at $x = 1/8$. A $p = 0.5$ within the multihole bags represents the most stable itinerant-electron configuration. Noda *et al* [164] have used resistivity and Hall-effect data as a function of x in $La_{1.4-x}Nd_{0.6}Sr_xCuO_4$ single-crystal films containing static stripes every fourth Cu–O–Cu row to identify a change from 1D charge transport for $x < 1/8$ to 2D transport for $x > 1/8$. This observation suggests that holes in excess of an average copper valence 2.5+ do not enter the metallic stripes but go into the localized-electron matrix between the stripes.

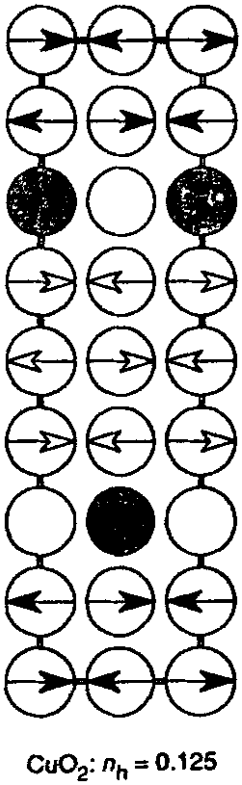

Figure 38. Itinerant-electron stripes every fourth Cu–O–Cu row in the CuO_2 sheets of $La_{0.38}Nd_{0.6}Sr_{0.12}CuO_4$, after [162].

McQueeney *et al* [165] have provided evidence from PDF analysis of pulsed neutron-diffraction data for $x = 0.15$ of the development with decreasing temperature of a dynamic ordering of holes in alternate rows of a CuO_2 sheet. A doubling of the periodicity along a Cu–O–Cu bond direction distinguishes this dynamic ordering phenomena from the static-stripe charge ordering at $x = 1/8$, which quadruples the periodicity. Moreover, Egami *et al* [166] identified hole-rich clusters in the hole-rich Cu–O–Cu rows. These clusters can be considered to consist of four Cu centres and five oxygen atoms within a row as illustrated in figure 39 [167]. This ordered configuration contains spin-paired two-electron/two-hole bags and corresponds to the hole concentration $p = 1/6$ where the maximum value of T_c is observed. It is reasonable to conclude that this vibronic striped phase represents the ordering of the bond-length fluctuations in the superconductive state with a condensation of paired spins in two-electron/two-hole correlation bags of small coherence length. Note that this configuration optimizes the Coulomb forces between the positively charged bags and the negatively charged matrix, the magnetic-exchange interactions between localized spins on the Cu(II) atoms, a 50–50 Cu(III)–Cu(II) in the two-hole bags, and Bose two-electron/two-hole bags containing paired spins while retaining a vibronic-electron character with a Fermi surface.

Considerable experimental work has been devoted to clarifying the role of spin fluctuations in the CuO_2 sheets and their relation to the high-temperature superconductivity found in the copper oxides. Unpolarized and polarized inelastic neutron scattering probes the dynamic magnetic susceptibility $\chi''(q, \omega)$ as a function of the energy transfer $\hbar\omega$ and the momentum

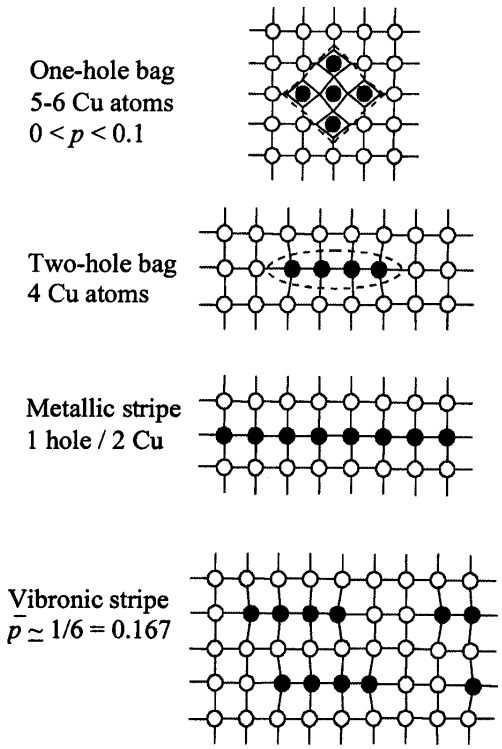

Figure 39. Correlation bags and stripes for Cu atoms of a CuO_2 sheet; ○ = Cu^{2+}, ● = $Cu^{2.2+}$ or $Cu^{2.5+}$, after [167].

transfer $\boldsymbol{q} = \boldsymbol{k}_i - \boldsymbol{k}_f$, where $\boldsymbol{k}_i$ and $\boldsymbol{k}_f$ are the incident and final neutron wavevectors. In the parent compound, antiferromagnetic Bragg peaks are found at $q_o = (\pi, \pi)$, i.e. at $\pm 1/2$, $\pm 1/2$ in units of $2\pi/a$, where a is the lattice constant. On doping p-type, two types of spin fluctuation are distinguished: incommensurate fluctuations at a quartet of wavevectors, displaced a distance δ in reciprocal space from the $q_o = (\pi, \pi)$ position [168–170], and a higher-energy, sharp (resonance) peak centred at (π, π). The resonance was not found in the $La_{2-x}Sr_xCuO_4$ system, but it has been observed in single-layer $Tl_{2-y}Ba_2CuO_{6+x}$ [171]; in the $YBa_2Cu_3O_{6+x}$ system, it appears above T_c in the underdoped compositions with an onset temperature T^* that coincides with the opening of a gap in the spin-excitation spectrum, but it is only found below $T^* = T_c$ for optimal and overdoped materials [172]. The resonance energy increases as kT_c in the underdoped samples, but it remains at $\hbar\omega_r \approx 41$ meV independently of T_c near optimal doping. A dependence on an applied magnetic field shows that the resonance is not a conventional spin-wave excitation and that it is associated with the phase coherence of superconductive electron pairs. However, the experiments do not distinguish whether the spin–spin exchange interactions are a driving force for formation of superconductive electron pairs or only reflect the phase coherence of preformed pairs.

The low-frequency incommensurate spin fluctuations, on the other hand, are present in both the $La_{2-x}Sr_xCuO_4$ and $YBa_2Cu_3O_{6+x}$ systems, and they are found in both the normal and superconducting states with a suppression of their intensity below T_c. The incommensurability parameter δ increases linearly with the hole fraction p and is proportional to T_c in the underdoped region $p < 1/8$, but it saturates in the optimal and overdoped compositional range. In $La_{2-x}Sr_xCuO_4$, δ increases with $\hbar\omega$ until it merges with the resonance peak. In

$YBa_2Cu_3O_{6+x}$, the spin gap Δ_{SG} was found to be proportional to T_c for $p < 0.1$, reaching $\Delta_{SG}/kT_c = 3.8$ at optimal doping [172].

Neutron scattering at $\boldsymbol{q}_o \pm \boldsymbol{\delta}$ can arise from a spin wave that is locally commensurate, but whose phase jumps by π at a periodic array of hole-rich stripes such as is illustrated by the static stripe configuration found by Tranquada *et al* [162, 163] at $p = 1/8$, figure 38. The equality of incommensurability and doping, $\delta = p$, follows naturally from this model. Yamada *et al* [173] reported a $\delta = p$ in underdoped $La_{2-x}Sr_xCuO_4$, which has led to the conclusion that the inelastic incommensurate neutron scattering is due to a fluctuating version of the stripes that are static in the Nd-doped samples. The stripes represent a heterogeneity of the electron system that is now generally accepted. The heterogeneity is a local and nonlinear phenomenon that is not describable in terms of FL theory. The basic physics underlying stripe formation is generally thought to be the expulsion of holes from regions of well formed local moments so as to optimize the spin–spin exchange interactions. What has yet to be more generally appreciated is that the regions not containing well formed local moments contain delocalized electrons as well as holes and that these hole-rich regions contain delocalized electrons because of cooperative oxygen-atom displacements that reduce the mean ⟨Cu–O⟩ bond length. The lattice instabilities responsible for the cooperative bond-length fluctuations occur as a result of the crossover from localized to itinerant electronic behaviour that gives rise to a double-well equilibrium (Cu–O) bond length in accordance with the virial theorem. The spin–spin interactions between localized electrons are only a part of the driving force for electronic heterogeneity. Lowering of the kinetic energy of the electrons in the hole-rich regions is a complementary, and perhaps even dominant, part of the driving force for dynamic phase separation on a microscopic scale.

McAllister and Attfield [174] have shown that the maximum value of T_c in $Ln_{1.85}A_{0.15}CuO_4$, Ln = lanthanide and A = alkaline earth, varies sensitively with the variance of the size of the cations in the rock-salt layers. This variance in the $La_{2-x}Sr_xCuO_4$ system may be responsible for lowering T_c to 36 K. Another single-layer system that can have its hole concentration varied from the underdoped to the overdoped range, but with retention of BaO rock-salt sheets neighbouring the CuO_2 sheets, is $HgBa_2CuO_{4+\delta}$. It has a maximum critical temperature of 97 K as against 36 K for $La_{2-x}Sr_xCuO_4$ and was considered by Yamamoto *et al* [175] to be more representative of the copper oxide superconductors than the $La_{2-x}Sr_xCuO_4$ system. Their thermoelectric-power data for $HgBa_2CuO_{4+\delta}$, figure 40, also show in this system the onset of superconductivity at $p \approx 0.05$ with a maximum value of T_c near $p \approx 0.16$; the superconductive samples all show the characteristic low-temperature enhancement $\alpha(T)$ with a maximum near 130 K. However, the temperature-independent thermoelectric power found between T_F and room temperature for $0 < p \leqslant 0.10$ in $La_{2-x}Sr_xCuO_4$ is restricted to the non-superconductive range $0 < p < 0.05$ in the $HgBa_2CuO_{4+\delta}$ system. Itoh *et al* [176] observed the opening of a spin gap Δ_{SG} at a temperature T^* (NMR); T^* decreases with hole doping in the underdoped compositions and extrapolates to T_c at $p \approx 0.19$. Yamamoto *et al* [175] obtained a $T^*(\alpha)$ and $T^*(\rho)$ as the respective temperatures at which $\alpha(T)$ and $\rho(T)$ deviate on cooling from a linear dependence on T; their critical temperatures are shown in figure 41 where a coincidence of the three determinations of T^* can be seen. The doping dependence of the spin-gap opening below T^* is similar to that reported for other high-temperature copper oxide superconductors; the appearance of a spin gap in the underdoped regime is a general characteristic of the copper oxide superconductors.

The transition from the QCP phase to the overdoped FL phase in the normal state has not been studied so intensively. Puchkov *et al* [177] have pointed out that the optical conductivity $\sigma(\omega)$ has two distinctly different regimes as a function of doping; in the underdoped samples, $\sigma(\omega)$ can be well described by an increasing density of mobile charge carriers as T_c increases

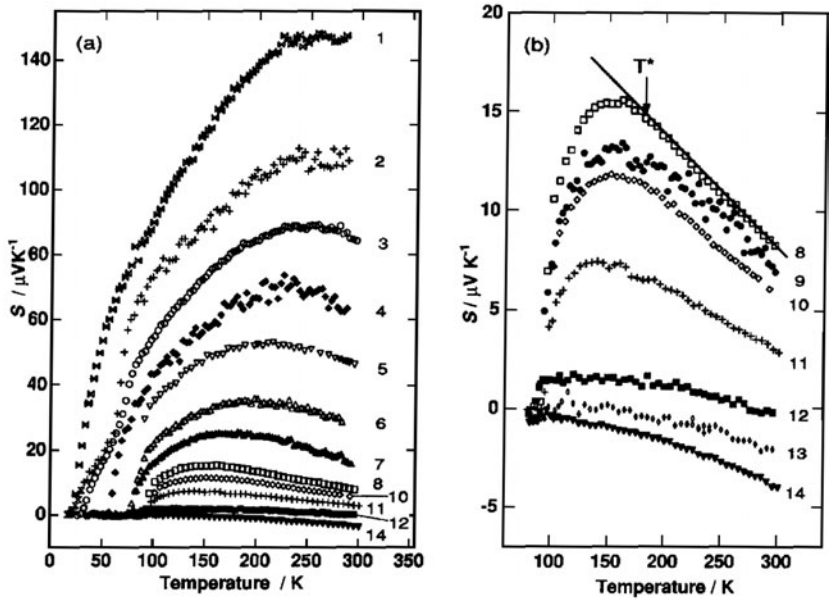

Figure 40. Temperature dependence of thermoelectric power for $HgBa_2CuO_{4+\delta}$ (a) over a wide doping range and (b) near the optimum doping. The numbers 1–14 correspond to $p = 0.040$, 0.046, 0.050, 0.057, 0.069, 0.090, 0.103, 0.110, 0.119, 0.127, 0.157, 0.180, 0.190 and 0.208, after [175].

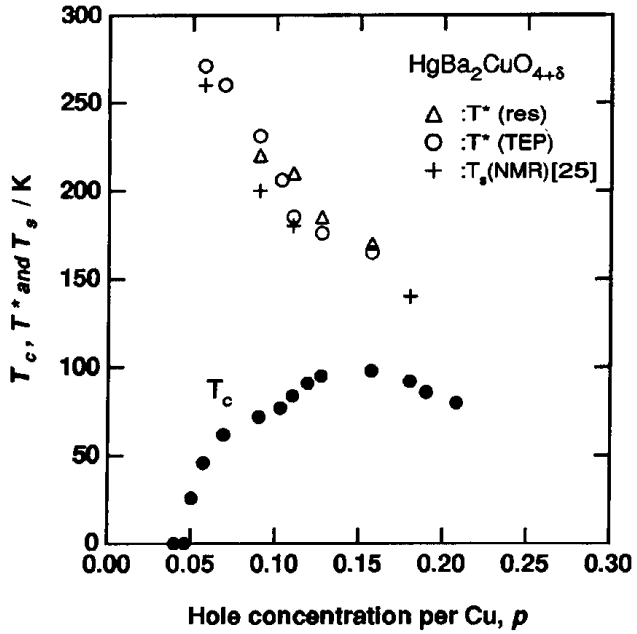

Figure 41. The superconducting critical temperature T_c and the characteristic temperature T^* as a function of hole concentration for $HgBa_2CuO_{4+\delta}$, after [175].

whereas in the overdoped regime there is no increase in the conductivity spectral weight as T_c decreases with increasing doping. The authors conclude that the doping-induced changes in

σ_1, the real part of $\sigma(\omega)$, in the overdoped regime are more consistent with a reduction in the scattering rate of the mobile carriers. Although a limited number of samples studied leaves unclear whether the transition from a vibronic diffusive motion in the QCP phase to itinerant-electron behaviour in the FL phase is smooth or first order at temperatures $T < T_l$, a decreasing volume fraction of the QCP phase in an FL matrix is consistent with the conclusion of Puchkov *et al*. Moreover, Wen *et al* [178], in a comparison of the diamagnetic susceptibilities of an underdoped and an overdoped sample each with the same critical temperature T_c, found a single transition in the underdoped sample and two superconductive transitions in the overdoped sample. They argued that this observation is evidence of a phase segregation between the superconductive (QCP) phase and an FL phase. See also discussion of Phillips [120a, b].

If the superconductive ordering of bond-length fluctuations is that illustrated in figure 39 for $p = 1/6$ and the additional holes in the overdoped regime are introduced first into the hole-rich stripes, some hole-rich stripes might be converted to metallic stripes containing a ratio Cu(III)/Cu(II) $= 1/2$ as occurs in the static stripes found in the LTT phase at $p = 1/8$ whereas others would retain a ratio Cu(III)/Cu(II) $= 1/3$. At a hole doping $p = 5/24$, the two types of hole-rich stripe would alternate with one another to form a competitive CDW phase. The plateau of T_c versus x at $x \approx 5/24$ in figure 32 and the suppression of superconductivity at $x \approx 5/24$ on substitution of less than 1% Zn for Cu are exactly analogous to what happens at $x = 1/8$ [179–181]. Whether the transition from orthorhombic to tetragonal symmetry at $x \approx 0.21$ is responsible for stabilization of a competitive CDW ordering of the bond-length fluctuations is not known, but it is clear that the Zn impurities are pinning otherwise mobile phase fluctuations. On the overdoped side, the phase fluctuations are between an FL phase and the QCP phase whereas on the underdoped side they are between the antiferromagnetic parent phase and the QCP phase, which supports the conclusion [182] that suppression of T_c from $T_{c\max}$ is a result of phase fluctuations of the superconductive order parameters, but with the caveat that these phase fluctuations may be sustained to lower temperatures by fluctuations between the QCP phase and its two neighbouring phases.

Angle-resolved photoemission spectroscopy (ARPES) has been used to study the evolution of the Fermi surface with temperature in $Bi_2Sr_2CaCu_2O_{8+\delta}$ [183–191], $Bi_2Sr_2CuO_{6+\delta}$ [192, 193] and $YBa_2Cu_3O_{7-x}$ [194]; its evolution with doping in $La_{2-x}Sr_xCuO_4$ has been obtained at $T = 11$ K by Ino *et al* [195–197]. The characteristic property of the QCP phase is a progressive transfer of spectral weight below 180 K from the (π, π) direction in reciprocal space to the $(\pi, 0)$ direction, figure 42 [191, 198], with the opening of a pseudogap in the $(\pi, 0)$ direction. The enhancement of $\alpha(T)$ below T_l reflects this spectral-weight transfer.

The vibronic QCP phase is characterized by strong electron–lattice interactions. Where the bond-length fluctuations are only locally cooperative, they suppress phonons having a dispersive energy. However, long-range ordering of the fluctuations into a travelling charge-density/spin-density wave (CDW/SDW) establishes phonons propagating along the Cu–O–Cu bond axes. The strong electron–lattice interactions may either stabilize a static CDW/SDW as occurs at $p = 1/8$ or they may induce a hybridization of the electrons and phonons that creates barely itinerant, vibronic quasiparticles of heavy mass and barely itinerant spins. Since hybridization would be with the phonons of vector $\boldsymbol{q}$ propagating along the Cu–O–Cu bond axes, the itinerant vibrons would have a momentum vector $\boldsymbol{k}' \sim \cos\theta + \mathrm{i}\sin\theta$, where θ is the angle between the electronic $\boldsymbol{k}$ vector and the phonon vector $\boldsymbol{q}$ [199]. Stabilization of a narrow band of itinerant-vibron states would induce transfer of electrons from the (π, π) to the $(\pi, 0)$ direction. The itinerant-vibron energies would have the symmetry

$$E_{\boldsymbol{k}'} \sim (\cos^2\theta - \sin^2\theta) + \mathrm{i}\sin 2\theta \sim (x^2 - y^2) + \mathrm{i}xy \tag{28}$$

with a real component $(x^2 - y^2)$ and a hidden component $\mathrm{i}xy$ that becomes manifest in

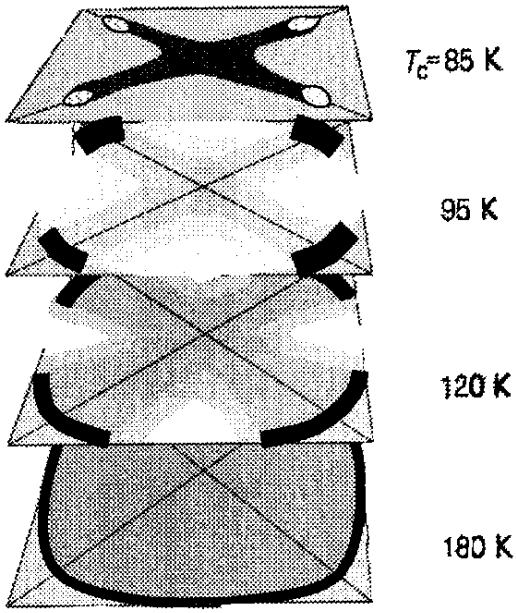

Figure 42. ARPES of underdoped $Bi_2Sr_2CaCu_2O_{8+\delta}$ showing the progressive transfer of spectral weight with decreasing temperature from the (π, π) to the $(\pi, 0)$ direction and the opening of a pseudogap at $(\pi, 0)$, after [198] from data of [191].

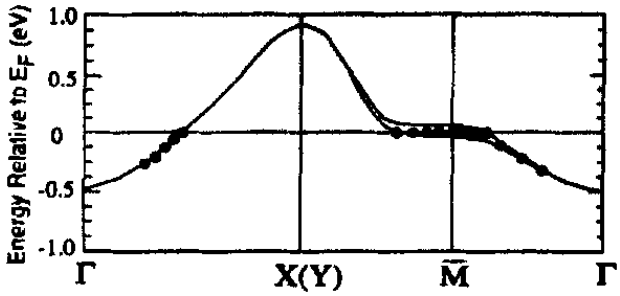

Figure 43. Experimental E versus $\boldsymbol{k}$ relationship along various high-symmetry directions (points) of the CuO_2 sheets of $Bi_2Sr_2CaCu_2O_{8+\delta}$. The lines illustrate a simple scenario compatible with the data, after [203].

a magnetic field. Experimental verification of the $x^2 - y^2$ symmetry came initially from NMR measurements [200] and superconductor–normal-state–superconductor (SNS) tunnel junctions [201, 202] in $YBa_2Cu_3O_{7-\delta}$. Dessau *et al* [203] have measured a flat electronic $E(k)$ dispersion in the $(\pi, 0)$ direction, compatible with barely itinerant vibronic states, figure 43. Deutscher and Dagan [204] and Sharoni *et al* [205] have argued from tunnelling experiments that the superconductive gap in overdoped samples has a symmetry $(x^2-y^2)+\mathrm{i}xy$ in the presence of an applied magnetic field. Laughlin [116] and Ramakrishnan [206] have independently proposed the existence of an $\mathrm{i}xy$ component to explain a kink behaviour observed in a thermal-transport measurement [207]. Zhu and Balatsky [208] have invoked coupling of a magnetic field with orbital magnetism to argue for a hidden $\mathrm{i}xy$ component of the pseudogap that becomes manifest with the application of a magnetic field.

Pines *et al* [209, 210] have derived an $(x^2 - y^2)$ symmetry for the normal state and the superconductive gap by introducing into the dynamic susceptibility a phenomenological term that peaks at spin-wavevector $\boldsymbol{Q}$:

$$\chi_{MMP}(q, \omega) = \alpha\xi^2/[1 + (\boldsymbol{Q} - \boldsymbol{q})^2\xi^2 - \mathrm{i}(\omega/\omega_{SF})] \tag{29}$$

where ξ is the antiferromagnetic correlation length, $\chi_Q = \alpha\xi^2$, the characteristic energy is $\varpi \sim \xi^{-z}$, and $\omega_{SF} = \text{constant}/\xi^z$ has a crossover from $z = 2$ to 1 at the temperature T_{Cr} at which $\chi_o(T)$ begins to decrease as T is decreased. The subscript MMP refers to Millis *et al* [210]. This term was added to the FL term to give a total susceptibility

$$\chi(q, \omega) = \chi_{MMP}(q, \omega) + \chi_{FL}(q, \omega). \tag{30}$$

However, their successful quantitative description of the spin dynamics in the QCP phase does not distinguish whether the spin–spin interactions drive or follow the ordering of the bond-length fluctuations responsible for the transfer of spectral weight from the (π, π) to the $(\pi, 0)$ direction. Both the spin–spin and electron–lattice interactions act cooperatively to open up the pseudogap.

Figure 44 shows the evolution with x of the Fermi surface of $La_{2-x}Sr_xCuO_4$ at $T = 11$ K as obtained by Ino *et al* [197] with ARPES. In the underdoped samples $x = 0.05$ and 0.10, dispersive features are only observed around $(\pi, 0)$; the dotted lines are drawn so as to make the area enclosed by the Fermi surface correspond to $(1 - x)$ electron states in the half Brillouin zone in accordance with the Luttinger sum rule. As x increases in the overdoped region, the Fermi surface near $(\pi, 0)$ moves smoothly through $(\pi, 0)$ so that the topological centre of the Fermi surface changes from p-type to n-type. On the underdoped side, the coexistence of the parent AFI and QCP phases results in a trapping of electrons in the lower Hubbard band of the AFI phase.

The electrons with $\boldsymbol{k}$ vectors oriented along the nodal lines of the $x^2 - y^2$ state symmetry do not hybridize with the phonons propagating along Cu–O–Cu bond axes as a result of long-range ordering of the (Cu–O) bond-length fluctuations. Therefore, the nodal electrons are described as a marginal FL [211]. Valla *et al* [212] have reported that the lifetimes of the nodal quasiparticles are only weakly affected by the onset of superconductivity.

There are four characteristic energies to be distinguished in the underdoped samples: a spin gap Δ_{SG}, a pseudogap Δ_{PG}, a superconductive gap Δ and a binding energy $E_{(\pi,0)}$ of the flat band at $(\pi, 0)$. A proportionality

$$\Delta_{PG} \approx 2.5E_{(\pi,0)} \approx 13\Delta \tag{31}$$

implies that Δ_{PG} reflects the binding energy of electron pairs within two-electron/two-hole bags. This binding energy decreases as the volume of the localized-electron matrix decreases and therefore with increasing hole fraction. The fact that these energy gaps decrease as T_c increases can be understood by distinguishing between the energy of the pseudogap Δ_{PG}, which measures the strength of the binding of electrons into pairs, and that of the stiffness ρ_s, which measures the ability of the superconducting state to carry supercurrent. Emery and Kivelson [213] have pointed out that a conventional superconductor has two important energy scales: the Bardeen–Cooper–Schrieffer (BCS) gap Δ and the phase stiffness ρ_s, where $\rho_s = \hbar^2 n_s(0)a/4m^*$ is proportional to the superfluid density $n_s(T)$. The phase stiffness is derived from the kinetic energy of the superfluid, which contains a superfluid velocity $v_s = \hbar\nabla\theta/2m^*$ having a phase angle θ of period 2π, and a short-distance cut-off of size a that is responsible for a transition to a low-temperature phase-ordered state below a temperature $T_\theta^{\max}$. The empirical relationship, equation (23), of Uemura *et al* [133] states that T_c is proportional to the zero-temperature superfluid density, i.e. to the phase stiffness $\rho_s(T = 0)$ for a wide range of underdoped materials. A $\Delta_{PG} \ll \rho_s$ is found in conventional superconductors, and destruction

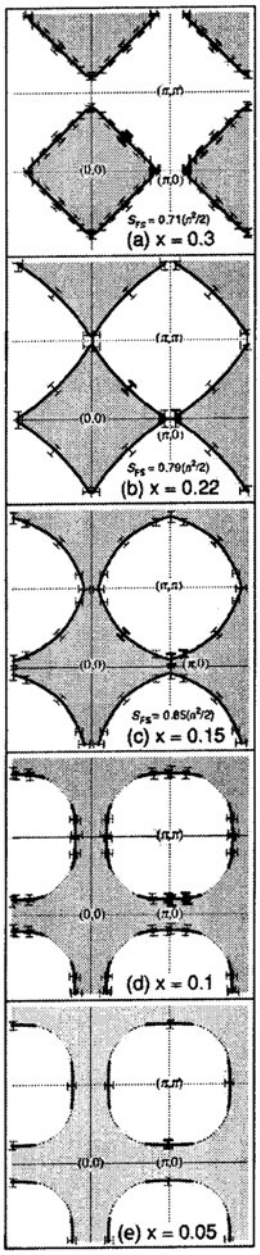

Figure 44. Fermi surfaces of $La_{2-x}Sr_xCuO_4$ obtained from ARPES experiments at $T = 11$ K [197]. Thick and thin error bars denote, respectively, the observed Fermi-surface crossings and those folded by symmetry. For dotted lines in $x = 0.05$ and 0.10 samples, see text.

of superconductivity begins with the break-up of electron pairs. In the cuprates, a $\Delta_{PG} > \rho_s$ is found in the underdoped samples, and T_c occurs where thermal agitation destroys the ability of the superconductor to carry a supercurrent while the pairs continue to exist. Therefore $T_c \sim \rho_s(T = 0\ \text{K})$ in the underdoped regime; $\rho_s(T = 0\ \text{K})$ may be reduced by thermal

excitation of nodal quasiparticles, which do not participate in the supercurrent [214–216], and $\rho_s(T = 0\ \mathrm{K}) < \Delta$ is found in the overdoped region.

Eschrig and Norman [217] have rationalized an anomalous momentum distribution of the ARPES spectra for the superconductive state of $Bi_2Sr_2CaCu_2O_{8+\delta}$ with a model that combines the flat electronic dispersion near $(\pi, 0)$ with a coupling of the fermionic degrees of freedom to a bosonic mode peaked in momentum near $Q = (\pi, \pi)$. In the model of figure 39 for $p = 1/6$, the two-electron/two-hole bags are bosonic entities and become barely itinerant in the $(\pi, 0)$ direction by hybridizing with phonons propagating along the Cu–O–Cu rows. Alexandrov [218, 218a] has been the principal advocate of the stability of bipolarons and has asserted his belief that superconductivity in the layered cuprates derives from the Bose–Einstein condensation (BEC) of bipolarons. Whereas his model calls for small bipolarons and BEC, the bosonic character appears to stem from two-electron/two-hole bags; hybridization of the Bose bags with a long-range ordering of the cooperative (Cu–O) bond-length fluctuations that create the bags gives the charge carriers an itinerant character and stabilizes a phase stiffness that allows the CuO_2 sheets to carry a supercurrent. Therefore, the BCS framework appears to be more appropriate than BEC, but with a non-retarded pairing potential.

Krasnov *et al* [219] have used intrinsic tunnelling spectroscopy to show that the pseudogap and the superconducting gap respond differently to a high magnetic field H. The superconducting gap Δ closes as $H \rightarrow H_{c2}(T)$ whereas the c-axis gap does not change below 100 K with either H or T. A high magnetic field would not influence either the formation of two-electron/two-hole bags or the ordering of the (Cu–O) bond-length fluctuations that allows hybridization of electrons and phonons, but it would destroy the superconductivity introduced by the phase stiffness.

Lupi *et al* [220] have extended an optical study of underdoped $Bi_2Sr_2CaCu_2O_{8+\delta}$ to the very-far-infrared region of frequencies in order to resolve two components of the optical conductivity $\sigma(\omega)$, a normal Drude term and a strong band peaked in the FIR having a tail exhibiting an ω^{-1} dependence rather than the ω^{-2} dependence of a conventional metal. The authors conclude that only the coexistence of two types of charge carrier can account for the optical absorption and that the anomalous optical pseudogap is an effect created by a temperature-dependent absorption of some weakly bound charges. The data support a phase-separation model in which itinerant and localized electrons coexist.

Raman scattering spectroscopy can also determine the $\boldsymbol{k}$ dependence of a gap size. The B_{1g} and B_{2g} spectra detect mainly the electronic states of the Fermi surface of a CuO_2 sheet near $(\pi, 0)$ and (π, π), respectively. The B_{1g} spectrum shows almost no temperature dependence in the underdoped regime whereas the B_{2g} spectrum shows suppression of spectral weight below 700 cm^{-1} at low temperatures as a result of an opening of the pseudogap [221, 222]. This observation motivated Liminov *et al* [223] to investigate the A_{1g} spectrum, which probes the entire Fermi surface, with electronic and phononic Raman scattering in detwinned crystals of underdoped and optimally doped $YBa_2Cu_3O_{7-\delta}$. They found no evidence for the opening of a pseudogap at optimum doping ($T_c = 93$ K), but a marked gap opening below $T^* \approx 180$ K in the electronic A_{1g} spectrum for the underdoped crystal ($T_c = 63$ K). The phononic spectrum gave a $T^* \approx 150$ K. Lack of any significant anomaly in the B_{1g} spectrum related to either Δ_{SG} or Δ implies a large suppression of the density of states around $(\pi, 0)$ has already set in at room temperature. It follows that the A_{1g} response originates from electronic states in the (π, π) direction, which is the same direction as that detected by the B_{2g} spectrum. From the ARPES data, this response signals the transfer of spectral weight from the (π, π) direction to the $(\pi, 0)$ direction below T^*. In addition, the Raman data showed the opening below T_c of a superconducting gap $2\Delta_{A1_g} \approx 120\ \mathrm{cm}^{-1}$ along the residual Fermi surface in the (π, π) direction; a $2\Delta_{B1_g} \approx 340\ \mathrm{cm}^{-1}$ was estimated for the $(\pi, 0)$ direction.

Unlike the pseudogap Δ_{PG} determined by ARPES and Raman scattering, the spin gap Δ_{SG} determined by neutron scattering [172] and the gap Δ_{IR} in the infrared response [224] increase with T_c. The development of antiferromagnetic spin correlations would depend on ordering of the bond-length fluctuations and would, therefore, have an onset temperature similar to the pseudogap T^*. However, the magnitude of Δ_{PG} depends on the energy of stabilization of the bosonic two-electron/two-hole bags whereas the spin gap Δ_{SG} reflects the degree of long-range order of the spin fluctuations of the localized-electron phase, which would be a maximum at $p \approx 1/6$ where T_c has its maximum value. Similarly, the infrared gap would reflect the ordering of the (Cu–O) bond-length fluctuations, and this order is also a maximum at $p \approx 1/6$.

Several papers have suggested that the pseudogap is due to superconductive-pair fluctuations. Although Δ_{PG} appears to be related to the formation of bosonic correlation bags, creation of these bags must be distinguished from formation of Cooper pairs. Following Pippard [225], Vidal *et al* [226] have argued from the uncertainty principle that the coherence length $\xi(T)$ of Cooper pairs must satisfy the constraint

$$\xi(T) \geqslant \xi(0) \tag{32}$$

which leads to a temperature T^c above which Cooper pairs cannot exist: $\xi(\varepsilon^c) \approx \xi(0)$, where $\varepsilon \equiv \ln(T/T_c)$ is a reduced temperature and $\varepsilon^c = \ln(T^c/T_c)$. Within the Gaussian–Ginsburg–Landau framework, the total energy

$$\xi^{-2}(\varepsilon) + k^2 \leqslant \xi(0) \tag{33}$$

in units of $\hbar^2/2m^*$ gives a cut-off at $\varepsilon = \varepsilon^c$. Applying this cut-off, Vidal *et al* [226] have found an excellent fit with their experimental determination of the dependence on ε of the fluctuation-induced magnetization and electrical conductivity for a variety of low-temperature and high-temperature superconductors that cover a range of $\xi(0)$ values varying by two orders of magnitude. Their results show that the normal-state pseudogap is not related to superconductive Cooper-pair fluctuations.

According to BCS theory, formation of Cooper pairs on cooling through T_c localizes itinerant electrons within the pair coherence length, which increases slightly the mean electronic kinetic energy. However, if T_c is determined by the superfluid stiffness rather than a pairing energy, as appears to be the case in the underdoped copper oxides, then the kinetic energy would decrease on cooling through T_c; the onset of the superfluid stiffness would be marked by an improved ordering of the Cu–O bond-length fluctuations, which would increase the volume fraction of itinerant vibrons and lower the mean kinetic energy. Motivated by an alternative argument by Hirsch [227, 228] for a decrease in the electronic kinetic energy on cooling through T_c, Molegraaf *et al* [229] made an optical study of underdoped $Bi_2Sr_2CaCu_2O_{8+\delta}$ that confirms this prediction. Using spectroscopic ellipsometry, they observed an in-plane spectral-weight transfer on cooling through T_c from above 10 000 cm^{-1} to the intraband optical range; and Santander-Syro *et al* [230] showed that transfer occurs to the infrared spectrum. From these measurements, a kinetic-energy lowering of about 1 meV/Cu atom was estimated.

Kabanov and Mihailovic [231, 232] have considered finite-$\boldsymbol{k}'$ electron–phonon coupling appropriate for a superconductor with a short coherence length. From group-theoretical analysis, they show that $k \neq 0$ phonons can couple to degenerate electronic states in the CuO_2 sheets, and a pseudo-Jahn–Teller distortion is found to be operative for oxygen vibration modes of E_u and E_g symmetry. Experimentally observed anomalies in inelastic neutron scattering, electron-spin resonance and near-edge x-ray absorption fine structure suggest that the important electron–phonon interaction is along the Cu–O–Cu rows. Their analysis supports the deduction of electron hybridization with phonons propagating along the Cu–O–Cu bond axes. Although

it does not provide a unique description of either the bosonic bags or the Cooper pairs, their analysis provides an early attempt to introduce cooperative bond-length fluctuations into an analytic framework.

Kusmartsev [233] has extended the bipolaron concept of Alexandrov to consider vibronic modes within an 'electronic molecule', which he considers to be a small bipolaron. However, the concept can be generalized to include a two-electron/two-hole correlation bag. This approach may allow description of the fluctuating shapes of the correlation bags in the normal state of the QCP phase.

5.4. Some properties of the n-type superconductors

The parent phases of the n-type superconductors contain only Cu^{2+} ions and are antiferromagnetic insulators like the parent La_2CuO_4 compound of the T/O structure. The $Ln_{2-x}Ce_xCuO_4$ systems having the T′ structure of figure 8(a) also contain Ln^{3+}-ion spins that order at low temperatures. In the superconductive compositions, antiferromagnetic ordering of the Ln^{3+}-ion spins has no apparent influence on the superconductive properties whatever the interactions between the spins on the Ln^{3+} and Cu^{2+} ions [234]. On initial doping ($x < x_c$), the charge carriers are small polarons; they do not occupy a multicentre correlation bag. Consequently the long-range antiferromagnetic ordering temperature does not drop anomalously steeply with increasing charge-carrier concentration as occurs in $La_{2-x}Sr_xCuO_4$. As illustrated in figure 29, the two-phase compositional range separating the antiferromagnetic, polaronic phase and the superconductive vibronic phase about $x \approx x_c$ is shifted to higher x as the ionic radius of the Ln^{3+} ion decreases [115]. As the size of the Ln^{3+} ion becomes smaller, the stretched Cu–O bond within the CuO_2 sheets approaches its equilibrium value and the Cu^{3+}/Cu^{2+} redox energy is raised, which reduces the O 2p covalent admixture and narrows the $(x^2 - y^2)\sigma^*$ band; a narrower bandwidth stabilizes the polaronic phase relative to the QCP phase. In the $Gd_{1-x}Ce_xCuO_4$ system, x_c is shifted beyond the superconductive compositional range, and no superconductive compositions have been found. This shift is evident in the magnetic phase diagram of $Sm_{1.85-x}Gd_xCe_{0.15}O_4$ shown in figure 45 taken from Nagata *et al* [235]. The diagram shows a suppression of superconductivity and stabilization of the antiferromagnetic phase for $x > 1.1$ with 0.15 charge carriers/Cu atom. The stability of the polaronic phase largely or completely suppresses the underdoped regime that is found in the p-type superconductors; therefore, the n-type superconductors do not exhibit a pseudogap.

As in the p-type superconductors, there is evidence that a two-phase region separates the QCP phase and the FL phase in the overdoped region. Caprara *et al* [236] have observed features in the optical conductivity $\sigma(\omega)$ that cannot be accounted for within a single-fluid model. It is noteworthy that stretching of the Cu–O bonds stabilizes the FL phase relative to the QCP phase, so the optimum doping is not achieved in $LaNd_{1-x}Ce_xCuO_4$.

ARPES data [237–239] have confirmed the conclusion from other experiments [240–243] that the superconductive gap Δ in the n-type superconductors also has $x^2 - y^2$ symmetry. The magnitude of Δ was found to be only about half that of the p-type superconductors having a T_c a little more than twice as large.

Measurements by Li *et al* [244] of the resistivity of $Nd_{2-x}Ce_xCuO_4$ ($x = 0.14$, 0.16, 0.18 and 0.20) single crystals showed a $\rho - \rho_i \sim T^2$ dependence well above T_c typical of overdoped p-type superconductors. The application of a magnetic field $H \geqslant 7$ T suppressed superconductivity in the optimally doped $x = 0.16$ sample and revealed a smooth transition at low temperatures ($T < T_c(H = 0)$) to semiconductive behaviour with a small motional enthalpy ΔH_m for the charge-carrier mobility that decreases with increasing x. A similar vibronic behaviour of the normal-state resistivity in fields $H > H_{c2}$ has been noted in several p-type superconductors [148, 245–250].

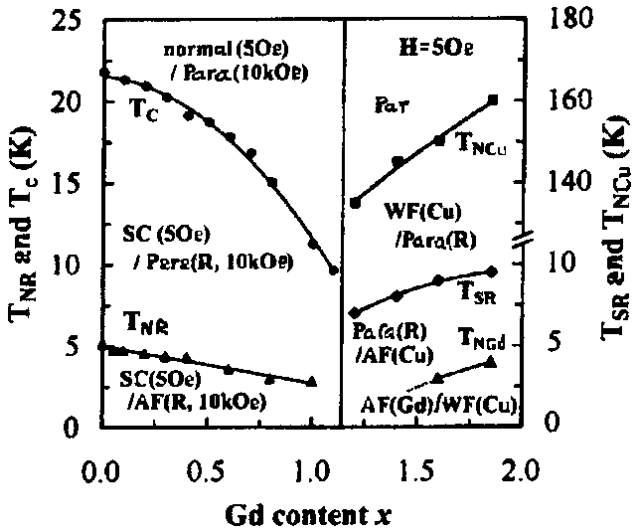

Figure 45. Magnetic phase diagram for the $Sm_{1.85-x}Gd_xCe_{0.15}CuO_4$ system at temperatures below 180 K. Transition temperatures were determined under applied magnetic fields of 5 and 10 kOe. T_c, T_{NR}, T_{NCu}, T_{NGd} and T_{SR} are the superconductive critical temperature, the Néel temperatures of the Sm, Cu and Gd sublattices, respectively, and a Cu-spin reorientation temperature. SC, WF, AF and Para represent superconductive, weak canted-spin ferromagnetic, antiferromagnetic and paramagnetic states, after [235].

Several theoretical models have been proposed to account for this phenomenon. In an attempt to distinguish between them, Budhani *et al* [251] measured the dependence on H of the thermoelectric power $\alpha(T)$ and the Hall coefficient $R_H(T)$ in underdoped ($x = 0.13$), optimally doped ($x = 0.15$) and overdoped ($x = 0.17$) $Pr_{2-x}Ce_xCuO_4$ films deposited epitaxially on a (100) face of $LaAlO_3$. They found a minimum in the in-plane resistivity $\rho_{ab}(T)$ at a characteristic temperature T^+ that increased with decreasing x; and below T^+, the resistivity varied as $\ln(1/T)$. This behaviour is similar to that shown in figure 34 for $La_{2-x}Sr_xCuO_4$ in which T^+ falls below T_c at optimum doping. Moreover, application of a magnetic field $H > H_{c2}$ to suppress T_c revealed that T^+ falls to zero in the interval $0.15 < x < 0.17$ of $Pr_{2-x}Ce_xCuO_4$, which is similar to the data of Li *et al* [244] for $Nd_{2-x}Ce_xCuO_4$. Analysis of the low-temperature $\alpha(T, H)$ and $R_H(T, H)$ data supports a model in which the transition at T^+ is caused by 2D weak localization; it also supports a vibronic model in which $\Delta H_m \to 0$ where the FL phase in the overdoped samples first percolates through the superconductive QCP phase.

Brugger *et al* [252] have reported evidence for low-temperature heavy-fermion behaviour in metallic $Nd_{2-x}Ce_xCuO_4$ ($x > 0.15$) as a result of hybridization of the FL electrons near the Fermi energy with the localized 4f states on the Nd^{3+} ions; no interaction between Ln^{3+}-4f and the heavy, superconductive Cu 3d vibrons has been detected.

In order to avoid complications due to interaction of the Cu 3d and Ln^{3+}-4f states, Williams *et al* [253] studied $\alpha(T)$ and ^{63}Cu NMR of the infinite-layer compound $Sr_{0.9}La_{0.1}CuO_2$ prepared under high pressure; it had a $T_c = 43$ K. The thermoelectric power $\alpha(T)$, figure 46, is negative and shows an anomalous enhancement with a maximum magnitude at about 120 K, which is analogous to the behaviour of $\alpha(T)$ in optimally doped and overdoped $La_{2-x}Sr_xCuO_4$ ($x \geqslant 0.15$) shown in figure 34. This enhancement correlates, in the p-type superconductors, with the transfer of spectral weight from the (π, π) to the $(\pi, 0)$ direction observed with ARPES.

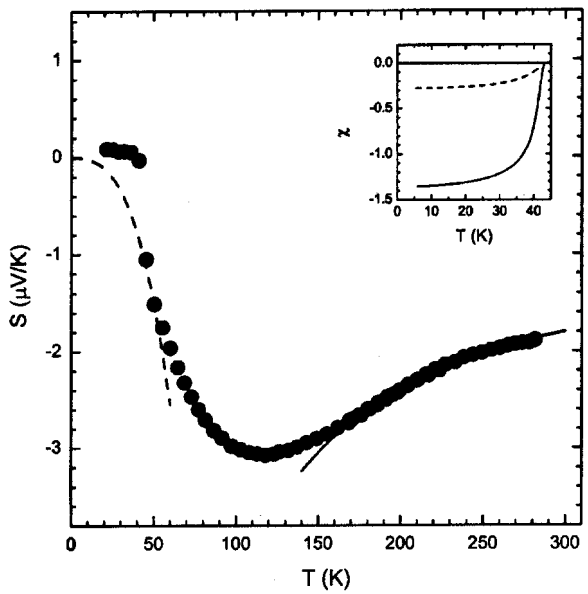

Figure 46. Thermoelectric power against temperature for n-type $Sr_{0.9}La_{0.1}CuO_2$. Inset: plot of the zero-field-cooled (solid curve) and field-cooled (dashed curve) dc susceptibility in $H = 2$ mT, after [253].

The magnitude of the pseudogap Δ_{PG} is associated with the formation of two-hole/two-electron correlation bags, not with the transfer of spectral weight. The transfer of spectral weight is to be associated with a hybridization of the vibronic charge carriers with the phonons introduced by ordering of the (Cu–O) bond-length fluctuations.

The ^{63}Cu NMR data in a field $H_\perp$ to the CuO_2 sheets of $Sr_{0.9}La_{0.1}CuO_2$ gave a Knight shift $^{63}K_{s,\perp}(T)$ that is temperature independent for $T > 50$ K; on cooling below 50 K, the $^{63}K_{s,\perp}(T)$ drops precipitously due to the opening of the spin gap Δ_{SG}, figure 47. This observation implies a flat Fermi surface within about $2\,kT$ of the Fermi energy and no opening of a pseudogap. The authors conclude that a density of states $N(\varepsilon_F)$ at the Fermi energy about one-quarter of that in $La_{1.85}Sr_{0.15}CuO_4$ together with a flat Fermi surface rules out models of the high-T_c superconductivity that are based on simple band-structure effects such as a van Hove singularity in the 3D band structure.

Interestingly, the $^{63}K_{s,\perp}(T)$ curve below T_c cannot be fitted to either a purely s-wave or purely d-wave order parameter; a best fit to the data requires, in addition to a d-wave order parameter, a residual $N_{\rm res}(\varepsilon_F) = 0.25N_o$, where N_o is the normal-state $N(\varepsilon_F)$, figure 47 inset. This observation implies that electrons with $\boldsymbol{k}$ vectors in the (π, π) direction do not become superconductive in $Sr_{0.9}La_{0.1}CuO_2$.

The Korringa relation for the spin–lattice relaxation rate T_1^{-1}, namely $^{63}T_1T\,^{63}K_s =$ constant, is not observed either in this case or in the hole-doped superconductive cuprates. The temperature dependence of $(^{63}T_1T)^{-1}$ in the normal state is remarkably similar to that observed for $La_{2-x}Sr_xCuO_4$ ($x \geqslant 0.15$) where neutron-scattering studies have shown the persistence of spin fluctuations. Therefore, it appears that $(^{63}T_1T)^{-1}$ is dominated by coupling to the antiferromagnetic spin fluctuation spectrum, which gives an increase in $(^{63}T_1T)^{-1}$ with decreasing temperature [254]. The n- and p-type copper oxide superconductors have similar dynamic spin susceptibilities, and the formation of Cooper pairs in the n-type superconductors

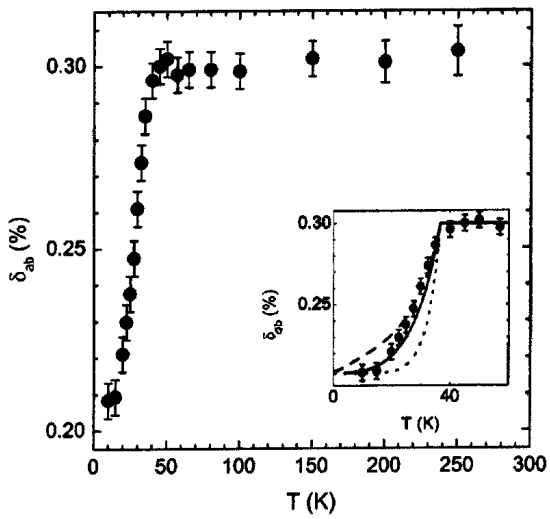

Figure 47. The ^{63}Cu NMR shift δ_{ab} for an $H = 9$ T perpendicular to the c axis of $Sr_{0.9}La_{0.1}CuO_2$. Subtraction of the temperature-independent orbital shift, the diamagnetic shift and the second-order nuclear quadrupole shift gives $^{63}K_{s,\perp}(T)$. Inset: data below T_c compared with an s-wave Δ_{SG} (dotted curve), a d-wave Δ_{SG} (dashed curve) and a d-wave Δ_{SG} with a residual density of states $N_{\rm res}(\varepsilon_F)/N_o = 1/4$ (solid curve) where N_o is $N(\varepsilon_F)$ in the normal state and $2\Delta_{SG}/kT_c = 7$, after [253].

is clearly analogous to that in the p-type superconductors; the superconductive state condensing in each case forms a QCP normal state. The separation of localized-electron regions with strong superexchange spin–spin interactions from itinerant-electron regions of lower electronic kinetic energy and no localized spins is a common feature. In each case cooperative bond-length fluctuations order at lower temperatures; the order induces hybridization of electrons and phonons to give itinerant vibronic states of large effective mass m^*.

Although bosonic two-electron/two-hole correlation bags can be identified in the underdoped and optimally doped compositions in the p-type superconductors and may be preserved in the overdoped region by a segregation of an FL phase and a superconductive QCP phase, the relationship between the bosonic clusters and formation of Cooper pairs has not yet been clarified. In the p-type superconductors, a two-electron/two-hole bag is formally a $2Cu^{3+} + 2Cu^{2+}$ cluster containing molecular σ^* electrons and having a smaller equilibrium Cu–O bond length than the Cu^{2+}-ion matrix. In the n-type superconductors, an analogous bag would be a $2Cu^{2+} + 2Cu^{+}$ cluster containing molecular σ^* electrons and having a larger equilibrium Cu–O bond length than the Cu^{2+}-ion matrix, but a smaller mean bond length than a cluster with localized Cu^{+} and Cu^{2+} ions. There is no evidence that such bosonic clusters form in the normal state of the n-type QCP phase; there may be simply the formation of heavy itinerant vibrons that form Cooper pairs having a coherence length comparable to that of the volume of a correlation bag. An inelastic neutron scattering study of the evolution with x of the phonon density of states for $Nd_{2-x}Ce_xCuO_4$ ($0 \leqslant x \leqslant 0.15$) showed softening of the Cu–O stretching and out-of-plane oxygen vibration modes in the polaronic compositions, not the superconductive compositions; the electron–lattice coupling in the n-type superconductors is clearly weaker than that in the p-type superconductors [255].

6. Conclusions

What is unique about the copper oxide superconductors? The answer lies in the confluence of several critical properties, any one or two of which may be found in oxides that are not superconductive. The following list of critical properties emerges from the data that have been summarized; the list may not be complete.

(1) Copper can be stabilized in three different formal valence states: Cu(I), Cu(II) and Cu(III). The Cu(I) and Cu(III) ions are diamagnetic; the Cu(II) carries a spin $S = 1/2$ where the $3d^9$ configuration remains localized. The orbital angular momentum of the $3d^9$ configuration is quenched.

(2) Removal of an electron from the Cu(I):$3d^{10}$ manifold favours formation of square-coplanar oxygen coordination at a Cu(II) with the hole in an antibonding $x^2 - y^2$ orbital. The Cu(II) ion may have, in addition, one or two more loosely bound apical oxygen(s), which means that the Cu(II) ion may occupy a square-coplanar site, a square-pyramidal site or a tetragonal ($c/a > 1$) octahedral site. The strong square-coplanar bonding at a Cu(II) ion lends itself to the formation of layered structures containing $Cu(II)O_2$ planes or sheets of corner-shared square-coplanar units making $(180° - \phi)$ Cu–O–Cu bonds.

(3) In a $Cu(II)O_2$ plane or sheet, the Cu(II)/Cu(I) redox couple lies an energy ΔE_p above the Cu(III)/Cu(II) redox couple, which is pinned at the top of the O 2p bands. This charge-transfer gap ΔE_p varies with the Cu–O bond length. A $\Delta E_p \approx 2$ eV is found where the Cu–O bond is under a compressive stress; it is smaller where the Cu–O bond is under tension. Transformation from localized to itinerant electronic behaviour of the $x^2 - y^2$ electrons induces a collapse of ΔE_p.

(4) In a point-charge model, the Cu(III)/Cu(II) redox energy lies below the O^{2-}:$2p^6$ energy, which means there is a dominant O 2p character in the antibonding $x^2 - y^2$ states pinned at the top of the O 2p bands; the Cu(III)/Cu(II) redox energy corresponds to these pinned $x^2 - y^2$ antibonding states and the gap between the Cu(II)/Cu(I) and Cu(III)/Cu(II) redox couples is referred to as a charge-transfer gap ΔE_p rather than an on-site Coulomb energy U. Moreover, removal of an electron from a Cu(II) ion to form Cu(III) is from the pinned $x^2 - y^2$ orbital in violation of Hund's highest multiplicity rule; the $(3z^2 - r^2)$ orbital lies an energy $(U - \Delta E_p)$ below the top of the O 2p bands. This low-spin character of the Cu(III) ions is critical; it means that only a single $x^2 - y^2$ band is partially occupied and there is no localized spin associated with any other orbitals. The $x^2 - y^2$ orbitals are half filled in the parent $Cu(II)O_2$ sheets.

(5) In layered oxides, mismatch between equilibrium metal–oxygen bond lengths in adjacent layers places the $Cu(II)O_2$ planes under a stress; a compressive stress is relieved by oxidation of the $Cu(II)O_2$ sheets, which enables p-type doping, whereas a tensile stress is relieved by reduction, which enables n-type doping.

(6) Although the $(180° - \phi)$ Cu–O–Cu interactions within a $Cu(II)O_2$ sheet are strong as a result of the Cu:3d–O:2p hybridization of the $x^2 - y^2$ orbitals, these parent sheets retain a localized spin on the Cu(II) atoms with strong antiferromagnetic superexchange interactions. However, the introduction of a hole fraction per Cu atom of $p > 0.27$ or an electron fraction per Cu atom of $n > 0.21$ results in the formation of a narrow band of itinerant $x^2 - y^2$ electrons forming an FL. A transition from localized to itinerant electronic behaviour is first order. High-temperature superconductivity is encountered where this first-order transition occurs in a mixed-valent system at a composition that allows superconductivity to compete with stabilization of a CDW. In the layered copper oxides with a 2D $x^2 - y^2$ band, this critical composition corresponds to $p \approx 1/6$ or $n \approx 1/6$.

(7) Where separation of localized-electron and itinerant-electron phases would occur at too low a temperature for atomic diffusion, it may be accomplished in an array of corner-shared transition-metal sites by cooperative oxygen-atom displacements. Where the two phases would have comparable valence fractions, these oxygen displacements may be only locally cooperative and fluctuating to give a polaronic liquid of vibronic charge carriers having a small motional enthalpy ΔH_m; however, long-range ordering of the fluctuations in such a QCP phase may occur at lower temperatures. Normally, this ordering results in stabilization of a static CDW, which opens a gap at the Fermi surface to suppress formation of Cooper pairs. Alternatively, the ordering may stabilize phonons that hybridize with the charge carriers to form itinerant vibrons of large effective mass. These can form superconductive Cooper pairs bound by a non-retarded elastic energy rather than the retarded potential of a conventional superconductor. Formation of bosonic bags that hybridize with the phononic cooperative oxygen vibrations that define them requires a critical charge-carrier concentration falling in the transition from localized to itinerant electronic behaviour.

(8) In a 2D square sublattice of transition-metal atoms, as occurs in the CuO_2 sheets, it is noteworthy that the critical charge-carrier concentrations $p \approx 1/6$ or $n \approx 1/6$ allow stabilization of two-carrier correlation bags in every other Cu–O–Cu row, as is illustrated in figure 39. This is the most stable configuration for bosonic two-carrier bags, and the dimensions of a bag correspond to the coherence length of a superconductive pair.

References

[1] Bednorz J G and Müller K A 1986 *Z. Phys.* B **64** 189
[2] Lee W C, Klemm R A and Johnston D C 1989 *Phys. Rev. Lett.* **62** 1012
[3] Takagi H, Batlogg B, Kao H L, Kwo J, Cava R J, Krajewski J J and Peck W F Jr 1992 *Phys. Rev. Lett.* **69** 2975
[4] Shannon R D and Prewitt C T 1969 *Acta Crystallogr.* B **25** 725
Shannon R D and Prewitt C T 1970 *Acta Crystallogr.* B **26** 1046
[5] Goodenough J B, Kafalas J A and Longo J M 1972 *Preparative Methods in Solid State Chemistry* ed P Hagenmuller (New York: Academic) ch 1
[6] Ruddlesden S N and Popper P 1957 *Acta Crystallogr.* **10** 538
Ruddlesden S N and Popper P 1958 *Acta Crystallogr.* **11** 54
[7] Cava R J, Batlogg B, Chen C H, Rietman E A, Zahurak S M and Werder D 1987 *Phys. Rev.* B **36** 5719
[8] Paranthaman M, Manthiram A and Goodenough J B 1992 *J. Solid State Chem.* **98** 343
[9] Nanjundaswamy K S, Manthiram A and Goodenough J B 1994 *J. Solid State Chem.* **111** 83
[10] Manthiram A and Goodenough J B 1988 *Appl. Phys. Lett.* **53** 420
[11] Torardi C C, Parise J B, Subramanian M A, Gopalakrishnan J and Sleight A W 1989 *Physica* C **157** 115
[12] Torardi C C, Jung D, Kang D B, Ren J and Wangbo M-H 1989 *Mater. Res. Soc. Symp. Proc.* **156** 295
[13] Ren J, Jung D, Wangbo M-H, Tarascon J-M, Le Page Y, McKinnon W R and Torardi C C 1989 *Physica* C **159** 151
[14] Marsh P, Flemming R M, Mandich M L, DeSantolo A M, Kwo J, Hong M and Martinez-Miranda L J 1988 *Nature* **334** 141
Karpinski J, Kaldis E, Jilek E, Rusiecki S and Bucher B 1988 *Nature* **336** 660
[15] Kaldis E, Fischer P, Hewat A W, Hewat E A, Karpinski J and Rusiecki S 1989 *Physica* C **159** 668
Karpinski J, Rusiecki S, Bucher B, Kaldis E and Jilek E 1989 *Physica* C **161** 618
[16] Zhou J-S, Goodenough J B, Dabrowski B and Rogacki K 1996 *Phys. Rev. Lett.* **77** 4253
[17] Bordet P, Chaillout C, Chenavas J, Hodeau J L, Marezio M, Karpinski J and Kaldis E 1988 *Nature* **334** 596
[18] Karpinski J, Kaldis E, Rusiecki S, Jilak E, Fischer P, Bordet P, Chaillout C, Chenavas J, Hodeau J L and Marezio M 1989 *J. Less-Common Met.* **150** 129
[19] Cava R J, Batlogg B, Krajewski J J, Rubb L W, Schneemeyer L F, Siegrist T, VanDover R B, Marsh P and Peck W F Jr 1988 *Nature* **336** 211
Cava R J, Marezio M, Krajewski J J, Peck W F Jr, Santoro A and Beech F 1989 *Physica* C **157** 272

[20] Subramanian M A, Gopalakrishnan J, Torardi C C, Gai P L, Boyes E D, Askew T R, Flippen R B, Farneth W E and Sleight A W 1989 *Physica* C **157** 124
[21] Giri R, Singh H K, Tiwari R S and Srivastava O N 2001 *Bull. Mater. Sci.* **24** 523
[22] Putilin S N, Antipov E V, Chmaissem O and Marezio M 1993 *Nature* **362** 226
[23] Bauernfeind L, Widder W and Braun H F 1995 *Physica* C **254** 151
[24] Bernhard C, Tallon J L, Brücher E and Kremer R K 2000 *Phys. Rev.* B **61** R14960
[25] Felner I, Asaf U, Levi Y and Millo O 2000 *Physica* C **334** 141
[26] Klamut P W, Dabrowski B, Kolesnik S, Maxwell M and Mais J 2001 *Phys. Rev.* B **63** 224512
[27] Boris A V, Mandal P, Bernhard C, Kovaleva N N, Pucher K, Hemberger J and Loidl A 2001 *Phys. Rev.* B **63** 184505
[28] Pozek M, Dulcic A, Paar D, Hamzic A, Basletic M, Tafra E, Williams G V M and Krämer S 2002 *Phys. Rev.* B **65** 174514
[29] Kumagai K, Takada S and Furukawa Y 2001 *Phys. Rev.* B **63** 180509(R)
[30] Tokunaga Y, Kotegawa H, Ishida K, Kitaoka Y, Takagiwa H and Akimitsu J 2001 *Phys. Rev. Lett.* **86** 5767
[31] Lynn J W, Keimer B, Ulrich C, Bernhard C and Tallon J L 2000 *Phys. Rev.* B **61** R14964
[32] Jorgensen J D, Chmaissem O, Shaked H, Short S, Klamut P W, Dabrowski B and Tallon J L 2001 *Phys. Rev.* B **63** 054440
[33] Takagiwa H, Akimitsu J, Kawano-Furukawa H and Yoshizawa H 2001 *J. Phys. Soc. Japan* **70** 333
[34] Williams G V M and Krämer S 2000 *Phys. Rev.* B **62** 4132
[35] Goodenough J B, Zhou J-S and Chan J 1993 *Phys. Rev.* B **47** 5275
[36] Goodenough J B 1994 *Materials and Crystallographic Aspects of High-T_c Superconductivity (NATO ASI Series vol 263)* ed E Kaldis (Dordrecht: Kluwer) p 175
[37] Müller-Buschbaum H and Wallschlager W Z 1975 *Z. Anorg. (Allg.) Chem.* **414** 76
[38] Manthiram A and Goodenough J B 1991 *J. Solid State Chem.* **92** 231
[39] Tokura Y, Takagi H and Uchida S 1989 *Nature* **337** 345
Takagi H, Uchida S and Tokura Y 1989 *Phys. Rev. Lett.* **62** 1197
[40] Markert J T and Maple M B 1989 *Solid State Commun.* **70** 145
Markert J T, Early E A, Bjornholm T, Ghamaty S, Lee B W, Neumeier J J, Price R D, Seaman C L and Maple M B 1989 *Physica* C **158** 178
[41] James A C W P, Zahurak S M and Murphy D W 1989 *Nature* **338** 240
[42] Grant P M, Parkin S S P, Lee V Y, Engler E M, Ramirez M L, Vazquez J E, Lim G, Jacowitz R D and Greene R L 1987 *Phys. Rev. Lett.* **58** 2482
[43] Johnston D C, Stokes J P, Goshorn D P and Lewandowski J T 1987 *Phys. Rev.* B **36** 4007
[44] Demazeau G, Tresse F, Plante T, Chevalier B, Etourneau J, Michel C, Hervieu M, Raveau B and Lejay P 1988 *Physica* C **153–155** 824
[45] Schirber J E, Morosin B, Merrill R M, Hlava P F, Venturini E I, Kwak J F, Nigrey P J, Baughman R J and Gimley D S 1988 *Physica* C **152** 121
[46] Zhou J-S, Sanjai S and Goodenough J B 1989 *Phys. Rev.* B **39** 12331
[47] Jorgensen J D, Dabrowski B, Pei S, Hinks D G, Soderholm L, Morosin B, Schirber J E, Venturini E L and Ginley D S 1988 *Phys. Rev.* B **38** 11337
[48] Zhou J S, Chen H and Goodenough J B 1994 *Phys. Rev.* B **50** 4168
[49] Chaillout C, Chenavas J, Cheong S-W, Fisk Z, Marezio M, Morosin B and Schirber J E 1990 *Physica* C **170** 87
[50] Akimitsu J, Suzuki S, Watanabe M and Sawa H 1988 *Japan. J. Appl. Phys.* **27** L1859
[51] Takayama-Muromachi E, Matsui Y, Uchida Y, Izumi F, Onoda M and Kato K 1988 *Japan. J. Appl. Phys.* **27** L2283
[52] Sawa H, Suzuki S, Watanabe M, Akimitsu J, Matsubara H, Watanabe H, Uchida S, Kokusho K, Asana H, Izumi F and Takayama-Muromachi E 1989 *Nature* **337** 447
[53] Siegrist T, Zahurak S M, Murphy D W and Roth R S 1989 *Nature* **334** 231
[54] Takano M, Takeda Y, Okada H, Miyamoto M and Kusaka T 1989 *Physica* C **159** 375
[55] Smith M G, Manthiram A, Zhou J-S, Goodenough J B and Markert J T 1991 *Nature* **351** 549
[56] Er G, Miyamoto Y, Kanamaru F and Kikkawa S 1991 *Physica* C **181** 206
[57] Arima T, Kikuchi K, Kasuya M, Koshihara S, Tokura Y, Ido T and Uchida S 1991 *Phys. Rev.* B **44** 917
[58] Attfield J P, Kharlanov A L and McAllister J A 1998 *Nature* **394** 157
[59] McAllister J A, Davies S and Attfield J P 2000 *J Solid State Chem.* **155** 138
[60] Goodenough J B 1971 *Prog. Solid State Chem.* **5** 145
[61] Anderson P W and Hasegawa H 1955 *Phys. Rev.* **100** 675
[62] Archibald W, Zhou J-S and Goodenough J B 1996 *Phys. Rev.* B **53** 14445

[63] Goodenough J B 1963 *Magnetism and the Chemical Bond* (New York: Wiley–Interscience)
[64] Geertsma W 1979 *Thesis* University of Groningen
quoted by
Zaanen J and Sawatzky G A 1987 *Can. J. Phys.* **65** 1262
[65] Zaanen J, Sawatzky G A and Allen J W 1985 *Phys. Rev. Lett.* **55** 418
[66] Arima T, Tokura Y and Torrance J B 1993 *Phys. Rev.* B **48** 17006
[67] Zhou J-S and Goodenough J B 2002 *Phys. Rev.* B **66** 052401
[68] Goodenough J B 1955 *Phys. Rev.* **100** 564
[69] Goodenough J B, Wold A, Arnott R J and Menyuk N 1961 *Phys. Rev.* **124** 373
[70] Zhou J-S, Yin H Q and Goodenough J B 2001 *Phys. Rev.* B **63** 184423
[71] Brinkman W F and Rice T M 1970 *Phys. Rev.* B **2** 4302
[72] Morikawa K, Mizokawa T, Kobayashi K, Fujimori A, Eisaki H, Uchida S, Iga F and Nishihara Y 1995 *Phys. Rev.* B **52** 13711
[73] Inoue I H, Hase I, Aiura Y, Fujimori A, Huruyama Y, Maruyama T and Nishihara Y 1995 *Phys. Rev. Lett.* **74** 2539
[74] Zhou J-S and Goodenough J B 1996 *Phys. Rev.* B **54** 13393
[75] Goodenough J B and Zhou J-S 1990 *Phys. Rev.* B **42** 4276
[76] Takano M, Nakanishi N, Takeda Y, Naka S and Takada T 1977 *Mater. Res. Bull.* **12** 923
[77] Kuwahara H and Tokura Y 1998 *Colossal Magnetoresistance, Charge Ordering and Related Properties of Manganese Oxides* ed C N R Rao and B Raveau (Singapore: World Scientific)
[78] Holstein T 1959 *Ann. Phys., NY* **8** 325
[79] Zhou J-S, Archibald W and Goodenough J B 2000 *Phys. Rev.* B **61** 3196
[80] Liu G-L, Zhou J S and Goodenough J B 2001 *Phys. Rev.* B **64** 144414
[81] Zhou J-S and Goodenough J B 2001 *Phys. Rev.* B **64** 024421
[82] Zhou J-S and Goodenough J B 1999 *Phys. Rev.* B **60** R15002
[83] Tobe K, Kimura T, Okimoto Y and Tokura Y 2001 *Phys. Rev.* B **64** 184421
[84] Bloch D 1966 *J. Phys. Chem. Solids* **27** 881
[85] Shrivastava K N and Jaccarino V 1976 *Phys. Rev.* B **13** 299
[86] Smith D W 1969 *J. Chem. Phys.* **50** 2784
[87] Zhou J-S and Goodenough J B 2002 *Phys. Rev. Lett.* **89** 087201
[88] Koehler W C and Wollan E O 1958 *J. Phys. Chem. Solids* **6** 287
[89] Goodenough J B and Raccah P M 1965 *J. Appl. Phys.* **36** 1031
[90] Lacorre P, Torrance J B, Pannetier J, Nazzal A I, Wang P and Huang T C 1991 *J. Solid State Chem.* **91** 225
[91] Torrance J B, Lacorre P, Nazzal A I, Ansaldo E J and Niedermayer Ch 1992 *Phys. Rev.* B **45** 8209
[92] García-Muñoz J L, Rodríguez-Carvajal J, Lacorre P and Torrance J B 1992 *Phys. Rev.* B **46** 4414
[93] Medarde M L 1997 *J. Phys.: Condens. Matter* **9** 1679
[94] García-Muñoz J L, Rodríguez-Carvajal J and Lacorre P 1992 *Europhys. Lett.* **20** 241
[95] Rodríguez-Carvajal J, Rosenkranz S, Medarde M, Lacorre P, Fernández-Díaz M T, Fauth F and Trounov V 1998 *Phys. Rev.* B **57** 456
[96] Alonso J A, García-Muñoz J L, Fernández-Díaz M T, Aranda M A G, Martínez-Lopez M J and Casais M T 1999 *Phys. Rev. Lett.* **82** 3871
[97] Alonso J A, Martínez-Lope M J, Casais M T, García-Muñoz J L and Fernández-Díaz M T 2000 *Phys. Rev.* B **61** 1756
[98] Alonso J A, Martínez-Lope M J, Casais M T, García-Muñoz J L, Fernández-Díaz M T, and Aranda M A G 2001 *Phys. Rev.* B **64** 094102
[99] Zaghrioui M, Bulou A, Lacorre P and Laffez P 2001 *Phys. Rev.* B **64** 081102(R)
[100] Staub U, Meijer G I, Fauth F, Allenspach R, Bednorz J G, Karpinski J, Kazakov S M, Paolasini L and d'Acapito F 2002 *Phys. Rev. Lett.* **88** 126402
[101] Zhou J-S, Goodenough J B and Dabrowski B 2003 *Phys. Rev. Lett.* B **67** 020404(R)
[102] Zhou J-S, Goodenough J B, Dabrowski B, Klamut P W and Bukowski Z 2000 *Phys. Rev.* B **61** 4401
[103] Zhou J-S, Goodenough J B, Dabrowski B, Klamut P W and Bukowski Z 2000 *Phys. Rev. Lett.* **84** 526
[104] Mott N F 1990 *Metal–Insulator Transitions* (London: Taylor and Francis)
[105] Massa N E, Alonso J A, Martínez-Lope M J and Rasines I 1997 *Phys. Rev.* B **56** 986
[106] Mroginski M A, Massa N E, Salva H, Alonso J A and Martínez-Lope M J 1999 *Phys. Rev.* B **60** 5304
[107] Medarde M, Lacorre P, Conder K, Fauth F and Furrer A 1998 *Phys. Rev. Lett.* **80** 2397
[108] Goodenough J B 1967 *Phys. Rev.* **164** 785
[109] Goodenough J B, Longo J M and Kafalas J A 1968 *Mater. Res. Bull.* **3** 471
[110] Goodenough J B and Zhou J-S 2001 *Struct. Bonding* **98** 17 and references therein

[111] Yamada Y, Suzuki J, Oikawa K, Katano S and Fernandez-Baca J A 2000 *Phys. Rev.* B **62** 11600
[112] Zhou J-S and Goodenough J B 2000 *Phys. Rev.* B **62** 3834
[113] Zhang F C and Rice T M 1988 *Phys. Rev.* B **37** 3759
[114] Bersuker G I and Goodenough J B 1997 *Physica* C **274** 267
[115] Manthiram A 1992 *J. Solid State Chem.* **100** 383
[116] Laughlin R B 1998 *Phys. Rev. Lett.* **80** 5188
[117] Sachdev S 2000 *Science* **288** 475
[118] Castellani C, Di Castro C and Grilli M 1995 *Phys. Rev. Lett.* **75** 4650
[119] Castellani C, DiCastro C and Grilli M 1997 *Z. Phys.* B **103** 137
[120] Emery V J and Kivelson S A 1995 *Phys. Rev. Lett.* **74** 3253
[120a] Phillips J C 2002 *Phys. Rev. Lett.* **88** 216401
[120b] Phillips J C 2002 *Phil. Mag.* B **82** 783
[121] Zolliker P, Cox D E, Parise J B, McCarron E M III and Farneth W E 1990 *Phys. Rev.* B **42** 6332
[122] Ryder J, Midgley P A, Exley R, Beynon R J, Yates D L, Afalfiz L and Wilson J A 1991 *Physica* C **173** 9
[123] Ahrens E T, Reyes A P, Hammel P C, Thompson J D, Canfield P C, Fisk Z and Schirber J E 1993 *Physica* C **212** 317
[124] Wattiaux A, Park J C, Grenier J C and Pouchard M 1990 *C. R. Acad. Sci., Paris* II **310** 1047
[125] Grenier J C, Lagueyte N, Wattiaux A, Doumerc J-P, Dordor P, Etourneau J, Pouchard M, Goodenough J B and Zhou J-S 1992 *Physica* C **202** 209
[126] Savici A T, Fudamoto Y, Gat I M, Ito T, Larkin M I, Uemura Y J, Luke G M, Kojima K M, Lee Y S, Kastner M A, Birgeneau R J and Yamada K 2002 *Phys. Rev.* B **66** 014524
[127] Khaykovich B, Lee Y S, Erwin R W, Lee S-H, Wakimoto S, Thomas K J, Kastner M A and Birgeneau R J 2002 *Phys. Rev.* B **66** 014528
[128] Abbamonte P, Venema L, Rusydi A, Sawatzky G A, Logvenov G and Bozovic I 2002 *Science* **297** 581
[129] Weidinger A, Niedermayer C, Golnik A, Simon R, Recknagel E, Budnick J I, Chamberland B and Baines C 1989 *Phys. Rev. Lett.* **62** 102
[130] Torrance J B, Bezinge A, Nazzal A I, Huang T C, Parkin S S P, Keane D T, LaPlaca S J, Horn P M and Held G A 1989 *Phys. Rev.* B **40** 8872
[131] Takagi H, Cava R J, Marezio M, Batlogg B, Krajewski J J, Peck W F Jr, Bordet P and Cox D E 1992 *Phys. Rev. Lett.* **68** 3777
[132] Zhou J-S, Chen H and Goodenough J B 1994 *Phys. Rev.* B **49** 9084
[133] Uemura Y J, Luke G M, Sternlieb B J, Brewer J H, Carolan J F, Hardy W N, Kadono R, Kempton J R, Kiefl R F, Kreitzman S R, Mulhern P, Riseman T M, Williams D Ll, Yang B X, Uchida S, Takagi H, Gopalakrishnan J, Sleight A W, Subramanian M A, Chien C L, Cieplak M Z, Xiao Gang, Lee V Y, Statt B W, Stronach C E, Kossler W J and Yu X H 1989 *Phys. Rev. Lett.* **62** 2317
[134] Presland M R, Tallon J L, Buckley R G, Liu R S and Flower N E 1991 *Physica* C **176** 95
[135] Nakamura Y and Uchida S 1992 *Phys. Rev.* B **46** 5841
[136] Zhou J-S, Goodenough J B, Sato H and Naito M 1999 *Phys. Rev.* B **59** 3827
[137] Sato H and Naito M 1997 *Physica* C **274** 221
[138] Chu C W, Gao L, Chen F, Huang Z J, Meng R L and Xue Y Y 1993 *Nature* **365** 323
[139] Gao L, Xue Y Y, Chen F, Xiong Q, Meng R L, Ramirez D, Chu C W, Eggert J H and Mao H K 1994 *Phys. Rev.* B **50** 4260
[140] Kosuge M, Tokiwa-Yamamoto A, Yamauchi H and Koshizuka N 1994 *Physica* C **225** 218
[141] Zhou J-S and Goodenough J B 1996 *Phys. Rev.* B **54** 12488
[142] Zhou J-S and Goodenough J B 1995 *Phys. Rev.* B **51** 3104
[143] Zhou J-S and Goodenough J B 1996 *Phys. Rev. Lett.* **77** 1190 comments on [144]
[144] Tallon J L, Cooper J R, de Silva P S I P N, Williams G V M and Loram J W 1995 *Phys. Rev. Lett.* **75** 4114
[145] Goodenough J B 1970 *J. Solid State Chem.* **1** 349
[146] Bersuker I B 1996 *Electronic Structure and Properties of Transition Metal Compounds* (New York: Wiley)
[147] Zhou J-S, Bersuker G I and Goodenough J B 1995 *J. Supercond.* **8** 541
[148] Boebinger G S, Ando Y, Passner A, Kimura T, Okuya M, Shimoyama J, Kishio K, Tamasaku K, Ichikawa N and Uchida S 1996 *Phys. Rev. Lett.* **77** 5417
[149] Orenstein J, Thomas G A, Millis A J, Cooper S L, Rapkine D H, Timusk T, Schneemeyer L F and Waszczak J V 1990 *Phys. Rev.* B **42** 6342
[150] Basov D N, Timusk T, Dabrowski B and Jorgensen J P 1994 *Phys. Rev.* B **50** 3511
[151] Timusk T, Homes C C, Bonn D A, Liang R and Hardy W N 1995 *Physica* C **254** 265
[152] Cannelli G, Canali M, Cantelli R, Cordero F, Ferraro S, Ferretti M and Trequattrini F 1992 *Phys. Rev.* B **45** 931

[153] Cho J H, Borsa F, Johnston D C and Torgeson D R 1992 *Phys. Rev.* B **46** 3179
[154] Julien M-H, Borsa F, Carretta P, Horvatic M, Berthier C and Lin C T 1999 *Phys. Rev. Lett.* **83** 604
[155] Wakimoto S, Shirane G, Endoh Y, Hirota K, Ueki S, Yamada K, Birgeneau R J, Kastner M A, Lee Y S, Gehring P M and Lee S H 1999 *Phys. Rev.* B **60** R769
[156] Wakimoto S, Birgeneau R J, Kastner M A, Lee Y S, Erwin R, Gehring P M, Lee S H, Fujita M, Yamada K, Endoh Y, Hirota K and Shirane G 2000 *Phys. Rev.* B **61** 3699
[157] Matsuda M, Fujita M, Yamada K, Birgeneau R J, Endoh Y and Shirane G 2002 *Phys. Rev.* B **65** 134515
[158] Fujita M, Yamada K, Hiraka H, Gehring P M, Lee S H, Wakimoto S and Shirane G 2002 *Phys. Rev.* B **65** 064505
[159] Bozin E S, Kwei G H, Takagi H and Billinge S J L 2000 *Phys. Rev. Lett.* **84** 5856
[160] Moodenbaugh A R, Xu Y, Suenaga M, Folkerts T J and Shelton R N 1988 *Phys. Rev.* B **38** 4596
[161] Sakita S, Nakamura F, Suzuki T and Fujita T 1999 *J. Phys. Soc. Japan* **68** 2755
[162] Tranquada J M, Sternlieb B J, Axe J D, Nakamura Y and Uchida S 1995 *Nature* **375** 561
[163] Tranquada J M, Ichikawa N and Uchida S 1999 *Phys. Rev.* B **59** 14712
[164] Noda T, Eisaki H and Uchida S 1999 *Science* **286** 265
[165] McQueeney R J, Petrov Y, Egami T, Yethiraj M, Shirane G and Endoh Y 1999 *Phys. Rev. Lett.* **82** 628
[166] Egami T, Petrov Y and Louca D 2000 *J. Supercond. Incorp. Novel Magn.* **13** 709
[167] Goodenough J B 2002 *Mater. Res. Soc. Symp. Proc.* **689** E3.1
[168] Cheong S-W, Aeppli G, Mason T E, Mook H, Hayden S M, Canfield P C, Fisk Z, Clausen K N and Martinez J L 1991 *Phys. Rev. Lett.* **67** 1791
[169] Mason T E, Aeppli G and Mook H A 1992 *Phys. Rev. Lett.* **68** 1414
[170] Thurston T R, Gehring P M, Shirane G, Birgeneau R J, Kastner M A, Endoh Y, Matsuda M, Yamada K, Kojima H and Tanaka I 1992 *Phys. Rev.* B **46** 9128
[171] He H, Bourges P, Sidis Y, Ulrich C, Regnault L P, Pailhès S, Berzigiarova N S, Kolesnikov N M and Keimer B 2002 *Science* **295** 1045
[172] Pengcheng Dai, Mook H A, Hunt R D and Dogan F 2001 *Phys. Rev.* B **63** 054525
[173] Yamada K, Lee C H, Kurahashi K, Wada J, Wakimoto S, Ueki S, Kimura H, Endoh Y, Hosoya S, Shirane G, Birgeneau R J, Greven M, Kastner M A and Kim Y J 1998 *Phys. Rev.* B **57** 6165
[174] McAllister J A and Attfield J P 2002 *Phys. Rev.* B **66** 014514
[175] Yamamoto A, Hu W-Z and Tajima S 2000 *Phys. Rev.* B **63** 024504
[176] Itoh Y, Machi T, Fukuoka A, Tanabe K and Yasuoka H 1996 *J. Phys. Soc. Japan* **65** 3751
[177] Puchkov A V, Fournier P, Timusk T and Kolesnikov N N 1996 *Phys. Rev. Lett.* **77** 1853
[178] Wen H H, Chen X H, Yang W L and Zhao Z X 2000 *Phys. Rev. Lett.* **85** 2805
[179] Kawamata T, Adachi T, Noji T and Koike Y 2000 *Phys. Rev.* B **62** R11981
[180] Watanabe I, Aoyama M, Akoshima M, Kawamata T, Adachi T, Koike Y, Ohira S, Higemoto W and Nagamine K 2000 *Phys. Rev.* B **62** R11985
[181] Watanabe I, Adachi T, Takahashi K, Yairi S, Koike Y and Nagamine K 2002 *Phys. Rev.* B **65** 180516(R)
[182] Meingast C, Pasler V, Nagel P, Rykov A, Tajima S and Olsson P 2001 *Phys. Rev. Lett.* **86** 1606
[183] Shen Z-X and Dessau D S 1995 *Phys. Rep.* **253** 1
[184] Marshall D S, Dessau D S, Loeser A G, Park C-H, Matsuura A Y, Eckstein J N, Bozovic I, Fournier P, Kapitulnik A, Spicer W E and Shen Z X 1996 *Phys. Rev. Lett.* **76** 4841
[185] Ding H, Norman M R, Yokoya T, Takeuchi T, Randeria M, Campuzano J C, Takahashi T, Mochiku T and Kadowaki K 1997 *Phys. Rev. Lett.* **78** 2628
[186] Ding H, Norman M R, Campuzano J C, Randeria M, Bellman A F, Yokoya T, Takahashi T, Mochiku T and Kadowaki K 1996 *Phys. Rev.* B **54** R9678
[187] Ding H, Yokoya T, Campuzano J C, Takahashi T, Randeria M, Norman M R, Mochiku T, Kadowaki K and Giapintzakis M 1996 *Nature* **382** 51
[188] White P J, Shen Z-X, Kim C, Harris J M, Loeser A G, Fournier P and Kapitulnik A 1996 *Phys. Rev.* B **54** R15669
[189] Loeser A G, Shen Z-X, Dessau D S, Marshall D S, Park C H, Fournier P and Kapitulnik A 1996 *Science* **273** 325
[190] Harris J M, Shen Z-X, White P J, Marshall D S, Schabel M C, Eckstein J N and Bozovic I 1996 *Phys. Rev.* B **54** R15665
[191] Norman M R, Ding H, Randeria M, Campuzano J C, Yokoya T, Takeuchi T, Takahashi T, Mochiku T, Kadowaki K, Guptasarma P and Hinks D G 1998 *Nature* **392** 157
[192] Harris J M, White P J, Shen Z-X, Ikeda H, Yoshizaki R, Eisaki H, Uchida S, Si W D, Xiong J W, Zhao Z-X and Dessau D S 1997 *Phys. Rev. Lett.* **79** 143
[193] King D M, Shen Z-X, Dessau D S, Marshall D S, Park C H, Spicer W E, Peng J L, Li Z Y and Greene R L 1994 *Phys. Rev. Lett.* **73** 3298

[194] Schabel M C, Park C-H, Matsuura A, Shen Z X, Bonn D A, Liang R and Hardy W N 1997 *Phys. Rev.* B **55** 2796
[195] Ino A, Kim C, Mizokawa T, Shen Z-X, Fujimori A, Takaba M, Tamasaku K, Eisaki H and Uchida S 1999 *J. Phys. Soc. Japan* **68** 1496
[196] Ino A, Kim C, Nakamura M, Yoshida T, Mizokawa T, Shen Z-X, Fujimori A, Kakeshita T, Eisaki H and Uchida S 2000 *Phys. Rev.* B **62** 4137
[197] Ino A, Kim C, Nakamura M, Yoshida T, Mizokawa T, Fujimori A, Shen Z-X, Kakeshita T, Eisaki H and Uchida S 2002 *Phys. Rev.* B **65** 094504
[198] Coleman P 1998 *Nature* **392** 134
[199] Goodenough J B 2002 *Europhys. Lett.* **57** 550
[200] Slichter C P 1994 *Strongly Correlated Electron Systems* ed K S Bedell *et al* (New York: Addison-Wesley) p 427
[201] Wollman D A, Van Harlingen D J, Lee W C, Ginsberg D M and Leggett A J 1993 *Phys. Rev. Lett.* **71** 2134
[202] Van Harlingen D J 1995 *Rev. Mod. Phys.* **67** 515
[203] Dessau D S, Shen Z-X, King D M, Marshall D S, Lombardo L W, Dickinson P H, Loeser A G, DiCarlo J, Park C-H, Kapitulnik A and Spicer W E 1993 *Phys. Rev. Lett.* **71** 2781
[204] Deutscher G and Dagan Y 2000 *J. Supercond. Incorp. Novel Magn.* **13** 699
[205] Sharoni A, Millo O, Kohen A, Dagan Y, Beck R, Deutscher G and Koren G 2002 *Phys. Rev.* B **65** 134526
[206] Ramakrishnan T V 1998 *J. Phys. Chem. Solids* **59** 1750
[207] Krishana K, Ong N P, Li Q, Gu G D and Koshizuka N 1997 *Science* **277** 83
[208] Zhu J-X and Balatsky A V 2002 *Phys. Rev.* B **65** 132502
[209] Pines D 1994 *Physica* B **199/200** 300
Pines D 1994 *Physica* C **235–240** 113
[210] Millis A, Monien H and Pines D 1990 *Phys. Rev.* B **42** 167
[211] Varma C M, Littlewood P B, Schmitt-Rink S, Abrahams E and Ruckenstein A E 1989 *Phys. Rev. Lett.* **63** 1996
[212] Valla T, Fedorov A V, Johnson P D, Wells B O, Hulbert S L, Li Q, Gu G D and Koshizuka N 1999 *Science* **285** 2110
[213] Emery V J and Kivelson S A 1995 *Nature* **374** 434
[214] Lee P A and Wen X-G 1997 *Phys. Rev. Lett.* **78** 4111
[215] Annett J, Goldenfeld N and Renn S R 1991 *Phys. Rev.* B **43** 2778
[216] Hardy W N, Bonn D A, Morgan D C, Liang R and Zhang K 1993 *Phys. Rev. Lett.* **70** 3999
[217] Eschrig M and Norman M R 2000 *Phys. Rev. Lett.* **85** 3261
[218] Alexandrov A S and Edwards P P 2000 *Physica* C **331** 97 and references therein
[218a] Alexandrov A S and Kornilovitch P E 2002 *J. Phys.: Condens. Matter* **14** 5337
[219] Krasnov V M, Kovalev A E, Yurgens A and Winkler D 2001 *Phys. Rev. Lett.* **86** 2657
[220] Lupi S, Calvani P, Capizzi M and Roy P 2000 *Phys. Rev.* B **62** 12418
[221] Nemetschek R, Opel M, Hoffmann C, Müller P F, Hackl R, Berger H, Forró L, Erb A and Walker E 1997 *Phys. Rev. Lett.* **78** 4837
[222] Opel M, Götzinger M, Hoffmann C, Nemetschek R, Philipp R, Venturini F, Hackl R, Erb A and Walker E 1999 *J. Low Temp. Phys.* **117** 347
[223] Limonov M F, Tajima S and Yamanaka A 2000 *Phys. Rev.* B **62** 11859
[224] McGuire J J, Windt M, Startseva T, Timusk T, Colson D and Viallet-Guillen V 2000 *Phys. Rev.* B **62** 8711
[225] Pippard A B 1953 *Proc. R. Soc.* A **216** 547
[226] Vidal F, Carballeira C, Currás S R, Mosqueira J, Ramallo M V, Veira J A and Viña J 2002 *Europhys. Lett.* **59** 754
[227] Hirsch J E 1992 *Physica* C **199** 305
[228] Hirsch J E 1992 *Physica* C **201** 347
[229] Molegraaf H J A, Presura C, van der Marel D, Kes P H and Li M 2002 *Science* **295** 2239
[230] Santander-Syro A F, Lobo R P S M, Bontemps N, Konstantinovic Z, Li Z Z and Raffy H see http//xxx.lanl.gov./pdf/cond-mat/0111539
[231] Kabanov V V and Mihailovic D 2002 *Phys. Rev.* B **65** 212508
[232] Mihailovic D and Kabanov V V 2001 *Phys. Rev.* B **63** 054505
[233] Kusmartsev F V 2002 *Europhys. Lett.* **57** 557
[234] Lynn J W, Sumarlin I W, Skanthakumar S, Li W-H, Shelton R N, Peng J L, Fisk Z and Cheong S-W 1990 *Phys. Rev.* B **41** 2569
[235] Nagata Y, Shioga T, Taniguchi T, Uchida T, Zhang L, Lan M D and Samata H 2002 *Phys. Rev.* B **65** 104506
[236] Caprara S, Di Castro C, Fratini S and Grilli M 2002 *Phys. Rev. Lett.* **88** 147001

[237] Sato T, Kamiyama T, Takahashi T, Kurahashi K and Yamada K 2001 *Science* **291** 1517
[238] Armitage N P, Lu D H, Feng D L, Kim C, Damascelli A, Shen K M, Ronning F, Shen Z-X, Onose Y, Taguchi Y and Tokura Y 2001 *Phys. Rev. Lett.* **86** 1126
[239] Armitage N P, Ronning F, Lu D H, Kim C, Damascelli A, Shen K M, Feng D L, Eisaki H, Shen Z-X, Mang P K, Kaneko N, Greven M, Onose Y, Taguchi Y and Tokura Y 2002 *Phys. Rev. Lett.* **88** 257001
[240] Hayashi F, Ueda E, Sato M, Kurahashi K and Yamada K 1998 *J. Phys. Soc. Japan* **67** 3234
[241] Tuei C C and Kirtley J R 2000 *Phys. Rev. Lett.* **85** 185
[242] Kokales J D, Fournier P, Mercaldo L V, Talanov V V, Greene R L and Anlage S M 2000 *Phys. Rev. Lett.* **85** 3696
[243] Prozorov R, Giannetta R W, Fournier P and Greene R L 2000 *Phys. Rev. Lett.* **85** 3700
[244] Li S Y, Mo W Q, Chen X H, Xiong Y M, Wang C H, Luo X G and Sun Z 2002 *Phys. Rev.* B **65** 224515
[245] Ando Y, Boebinger G S, Passner A, Kimura T and Kishio K 1995 *Phys. Rev. Lett.* **75** 4662
[246] Ando Y, Boebinger G S, Passner A, Tamasaku K, Ichikawa N, Uchida S, Okuya M, Kimura T, Shimoyama J and Kishio K 1996 *J. Low Temp. Phys.* **105** 867
[247] Ono S, Ando Y, Murayama T, Balakirev F F, Betts J B and Boebinger G S 2000 *Phys. Rev. Lett.* **85** 638
[248] Hidaka Y, Tajima Y, Sugiyama K, Tomiyama F, Yamagishi A, Date M and Hidaka M 1991 *J. Phys. Soc. Japan* **60** 1185
[249] Harus G I, Ignatenkov A N, Ponomarev A I, Sabirzyanova L D, Shelushinina N G and Babushkina N A 1999 *JETP Lett.* **70** 97
[250] Fournier P, Mohanty P, Maiser E, Darzens S, Venkatesan T, Lobb C J, Czjzek G, Webb R A and Greene R L 1998 *Phys. Rev. Lett.* **81** 4720
[251] Budhani R C, Sullivan M C, Lobb C J and Greene R L 2002 *Phys. Rev.* B **65** 100517(R)
[252] Brugger T, Schreiner T, Roth G, Adelmann P and Czjzek G 1993 *Phys. Rev. Lett.* **71** 2481
[253] Williams G V M, Dupree R, Howes A, Krämer S, Trodahl H J, Jung C U, Park M-S and Lee S-I 2002 *Phys. Rev.* B **65** 224520
[254] Millis A J, Moinen H and Pines D 1990 *Phys. Rev.* B **42** 167
[255] Kang H J, Dai Pengcheng, Mandrus D, Jin R, Mook H A, Adroja D T, Bennington S M, Lee S-H and Lynn J W 2002 *Phys. Rev.* B **66** 064506